

EFFECT OF PARASITIC PARAMETERS AND ENVIRONMENTAL CONDITIONS ON I-V AND P-V CHARACTERISTICS OF 1D5P MODEL SOLAR PV CELL USING LTSPICE-IV[†]

 **Muhammad Aamir Shafi^{a,e,f,*}, Muneeb Khan^b, Sumayya Bibi^c, Muhammad Yasir Shafi^b,
Noreena Rabbani^d,  **Hanif Ullah^e,  **Laiq Khan^a,  **Bernabe Mari^f********

^aDepartment of Electrical Engineering, COMSATS University Islamabad, Pakistan

^bDepartment of Electrical Engineering, Institute of Southern Punjab Multan, Pakistan

^cDepartment of Electrical Engineering, Bahauddin Zakariya University Multan, Pakistan

^dDepartment of Electrical Engineering, Sarhad University of Science & Information Technology, Peshawar, Pakistan

^eDepartment of Electrical Engineering, Federal Urdu University of Arts, Science and Technology, Islamabad, Pakistan

^fInstituto de diseño y Fabricación (IDF), Universitat Politècnica de València (UPV), Spain

^{*}Corresponding Author: aamirshafi@ymail.com, tel. +923016065560, +923006951920

Received March 6, 2022; revised March 28, 2022; accepted April 5, 2022

In this research work, the electrical simulation of 1D5P model solar cell is done using LTSpice-IV simulation software. In this work effect of environmental conditions i.e temperature, solar irradiance, and parasitic parameters i.e series as well as shunt resistances was carried out. It has been discovered that as temperature increases the performance of solar cell decrease because temperature causes to increase the recombination phenomenon and hence lower the performance. However, when the temperature rises from 0°C to 50°C, the I-V and P-V curves move to the origin showing the negative effect of increasing temperature on the solar cell. Solar irradiance has major role on the performance of solar cell. As solar irradiance increases from 250 Wm⁻² to 1000 Wm⁻², the performance of solar cell increases accordingly and I-V as well as P-V curve moves away from the origin. It is concluded that for different series resistances, I-V along with P-V characteristic of 1D5P model solar cell varies, as at 0.02Ω series resistance, a maximum short circuit current and maximum power is obtained. But when series resistance increased up to 2 ohm only, the I-V and P-V curves moves to origin drastically. Shunt Resistance is the path of reverse current of the cell. As the shunt resistance increases, the path for reverse current decreased, hence all current goes to load, hence maximum power is obtained. Similarly when the value of shunt resistance decreased, the voltage-controlled section of I-V characteristics curve is moved closer to the origin hence reduced the solar cell performance. It's critical to understand how different factors affect the I-V and P-V characteristics curves of solar cells. The open circuit voltage, short circuit current and maximum power is all variable. The influence of these factors may be extremely beneficial when tracking highest power point of a solar cell applying various methods.

Keywords: Solar Cell, 1D5P, Simulation, Temperature, Irradiance, LTSpice

PACS: 02.60.Cb, 02.60.Pn, 82.47.Jk, 84.60.Jt, 42.79.Ek, 89.30.Cc

Because of the catastrophic situation with conventional fuels, renewable energy sources have grown increasingly appealing. Solar energy consumption has grown by 20 percent to 25 percent in the last 20 years [1]. PV cells are devices that use solar energy to turn it directly into electricity. However, energy generation has a significant impact on the environment and solar cell manufacture. The short circuit current increases somewhat as temperature rise, whereas open circuit voltage of PV cell drops significantly [2].

A short circuit current decreases as sun irradiation decreased [3]. The open circuit voltage, on the other hand, does not fluctuate substantially. It is substantially diminished after a certain point [4]. Voltage drop between junction and terminal increases as the series resistance of the PV cell increases, as well as current-controlled section of I-V characteristics curve moves closer to the origin [5]. Current flowing through the shunt resistance improves when the shunt resistance is reduced, and the voltage regulated part of I-V characteristics curve moves closer to an origin [6].

The characteristics curves of PV cells are affected by changes in many factors. This document includes a brief explanation of the PV cell as well as LTSpice IV modeling [7]. LTSpice IV is a strong, high-performance, and a quick sufficient program that makes it simple to build and simulate various circuit models while also providing accurate simulation results. LTSpice's capabilities include the ability to do simulations based on transient, AC, noise, and DC analyses [8]. Because of its advantages, LTSpice IV is utilized to run the simulations. This simulation tool is entirely free and is easily downloaded from the LTC website [9]. It is compatible with a wide range of operating systems, including Windows NT4.0, Me, XP, Vista, Windows 7, Windows 8, Windows 8.1, and Windows 10. LTSpice-IV program is available for Linux users also [10].

PV CELL MODELING

Mathematical expressions representing current-voltage (I-V) curves describe the electric performance of solar modules. Typically, seven mathematical models are employed, split into three categories as shown in Table 1 [11]. The

[†] **Cite as:** M.A. Shafi, M. Khan, S. Bibi, M.Y. Shafi, N. Rabbani, H. Ullah, L. Khan, and B. Mari, East Eur. J. Phys. 2, 64 (2022), <https://doi.org/10.26565/2312-4334-2022-2-07>

© M.A. Shafi, S. Bibi, M.M. Khan, H. Sikandar, F. Javed, H. Ullah, L. Khan, B. Mari, 2022

single diode variant is the most common. Because these equations are non-linear, the right procedures for extracting their parameters are required. Several writers have reviewed the approaches for extracting module parameters in the literature [12,13,14].

Despite the fact that these many approaches are strong, the majority of them, particularly iterative methods like the Levenberg-Marquardt (LM) algorithm, need beginning data. In most cases, the user enters these initial settings instinctively. Algorithm's computation will take a long time or, at the very least, a convergence problem will arise if input values are distant from true beginning values. Because incorrect starting values might influence algorithm accuracy, convergence, and computation time, it would be beneficial to have a way to get these initial values [15].

Table. 1. Classification of photovoltaic cell comparable models [16].

Group	Model	Parameters
One Diode Model	3 Parameters Model	I_{ph}, I_0, n
	4 Parameters Model	I_{ph}, I_0, n, R_s
	5 Parameters Model	$I_{ph}, I_0, n, R_s, R_{sh}$
One Diode Model	6 Parameters Model	$I_{ph}, I_{o1}, n_1, I_{o2}, n_2, R_s$
	7 Parameters Model	$I_{ph}, I_{o1}, n_1, I_{o2}, n_2, R_s, R_{sh}$
Model with recombination in intrinsic layer	1 Diode Model with Recombination	$I_{ph}, I_0, n, R_s, R_{sh}, \mu\tau$
	2 Diode Model with Recombination	$I_{ph}, I_{o1}, n_1, I_{o2}, n_2, R_s, R_{sh}, \mu\tau$

Equation of the diode current is

$$I_d = I_0(e^{\frac{qV_d}{kT}} - 1) \tag{1}$$

Equation of load current is

$$I_L = I_{ph} - I_d \tag{2}$$

$$I_L = I_{ph} - I_0(e^{\frac{qV_d}{kT}} - 1) \tag{3}$$

When terminals are short circuited ($V_d = 0$);

$$I_{sc} = I_{ph} - I_0(e^{\frac{q0}{kT}} - 1) \tag{4}$$

$$I_{sc} = I_{ph} \tag{5}$$

When terminals are open circuited ($I_{sc} = 0$);

$$V_d = V_L = V_{oc} \tag{6}$$

$$V_{oc} = \left(\frac{kT}{q}\right) \ln \left\{ \left(\frac{I_{ph}}{I_0}\right) + 1 \right\} \tag{7}$$

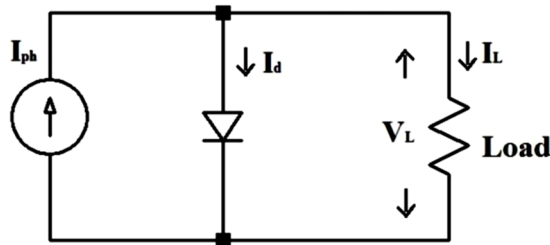


Figure 1. Ideal Equivalent Circuit of a Solar Cell [17].

A current source, a diode, and a shunt resistance R_p parallel to it make up the realistic equivalent circuit of a solar cell as given in Figure 2. Between a connection and load there lies a series resistance R_s [5].

Equation of load current is,

$$I_L = I_{ph} - I_d - I_p \tag{8}$$

$$I_L = I_{ph} - I_0(e^{\frac{qI_{ph}R_s}{kT}} - 1) - \left(I_{ph} \frac{R_s}{R_p}\right) \tag{9}$$

Open circuit voltage (V_{oc}) equation:

$$V_{oc} = \left(\frac{kT}{q}\right) \ln \left\{ \left(\frac{I_{ph}}{I_0}\right) + 1 \right\} \tag{10}$$

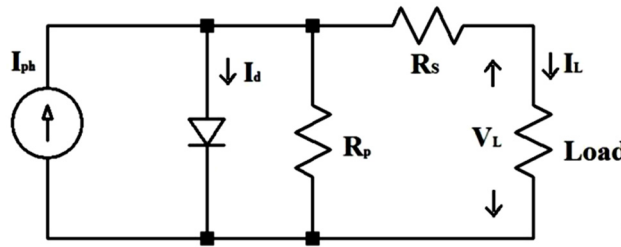


Figure 2. Practical Equivalent Circuit of a Solar Cell [18].

I-V and P-V characteristics of solar cell

The following Figure 3 describes I-V as well as P-V characteristics of solar cell.

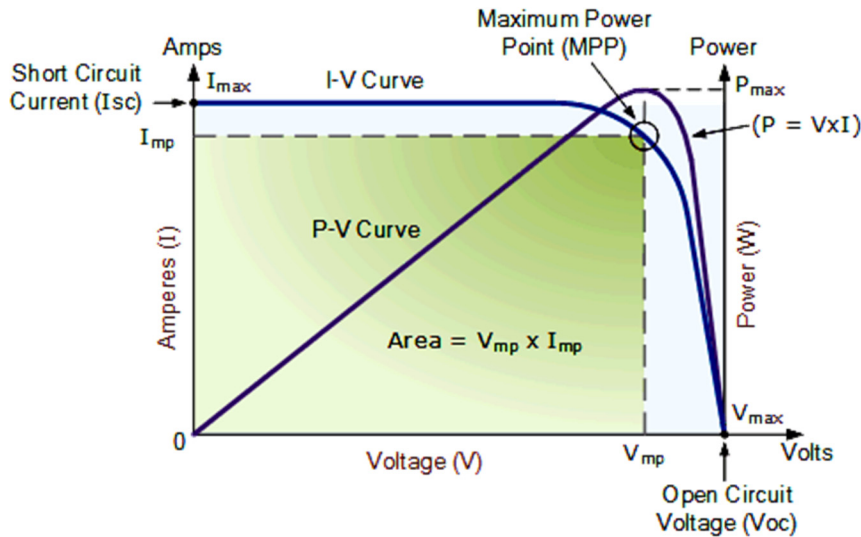


Figure 3. I-V and P-V Characteristics Curve of Solar Cell [19].

For a single operating point, maximum power is gained at output of a solar cell. When the given quantity of load is applied, the resulting power at load is P_L for load current I_L as well as load voltage V_L . However, for a given load value, the load current ($I_L = I_{mpp}$) and load voltage ($V_L = V_{mpp}$) are maximum, and the power obtained is maximum, P_{max} . Ratio of maximum power to product of V_{oc} and I_{sc} is known as the fill factor that reflects quality of solar cell [20]. Changes in parameters have an impact on I-V characteristics curve and maximum power value. As a result, it's critical to understand the impact of changing these factors [21].

Simulation of Solar Cell Model using LTSpice-IV

Schematic diagram of solar cell model 1D5P (one diode, five parameters) is shown in Figure 4. This model is used to simulate the effects of temperature, sun irradiation, series resistance, and shunt resistance of the solar cell.

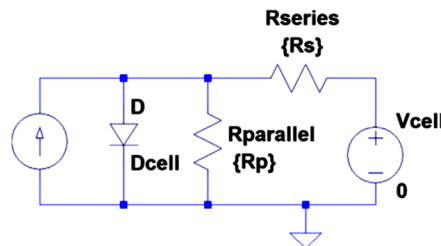


Figure 4. Single-diode solar cell 1D5P-model simulated in LTSpice IV.

As illustrated in Figure 5, the model accepts as input the cell characteristics in reference circumstances as well as environmental data (cell temperature, irradiation). The characteristics of solar cells change as a result of climatic factors (irradiation, temperature).



Figure 5. Illustrative diagrams of the inputs and outputs of the LTSpice model.

RESULTS AND DISCUSSION

Temperature Effect on 1D5P Model Solar Cell

PV system-1 (1D5P) is used to demonstrate the effect of temperature variation. The command used in LTSpice IV to run the simulation is (step temp 0 50 10). The beginning temperature is 0 degree, with 10 degrees as the step size and 50 degrees as the end temperature. The series and shunt resistances are 0.03 Ohms and 500 Ohms, respectively, in 1D5P solar cell model. The current source is assumed to be 3A since the irradiance is 1000 Wm⁻². The simulation for the temperature impact is illustrated in Figures 6 and 7. The curve on the right represents 0 degrees celsius, while the curves on the left represent 10, 20, 30, 40, and 50 degrees celsius, respectively.

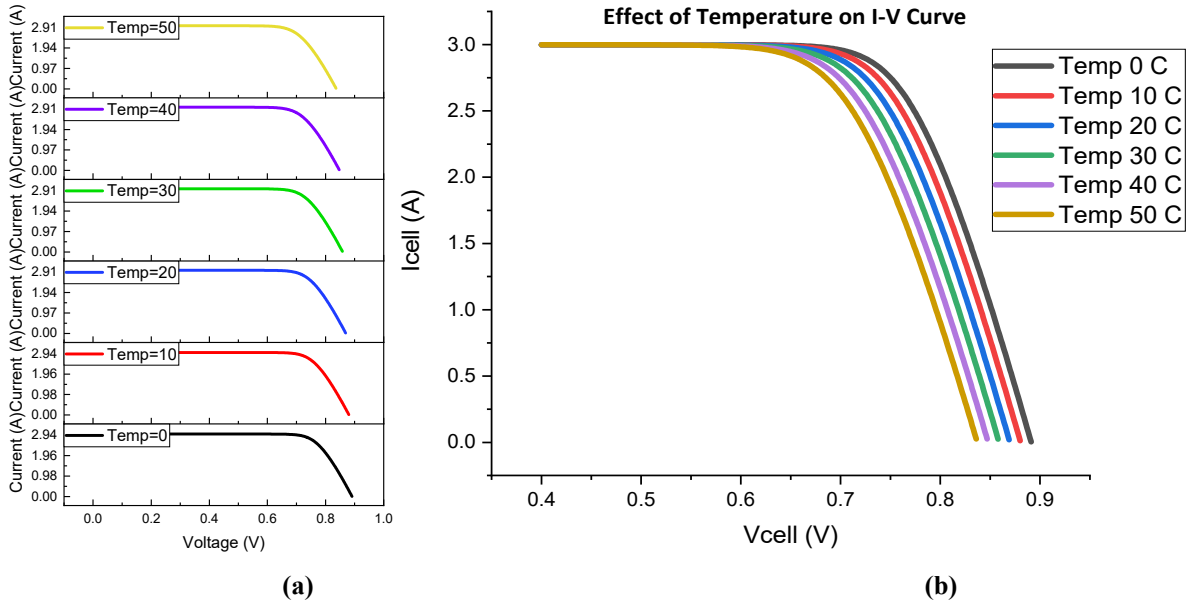


Figure 6. Temperature effect on I-V curve (a) Stack (b) Batch

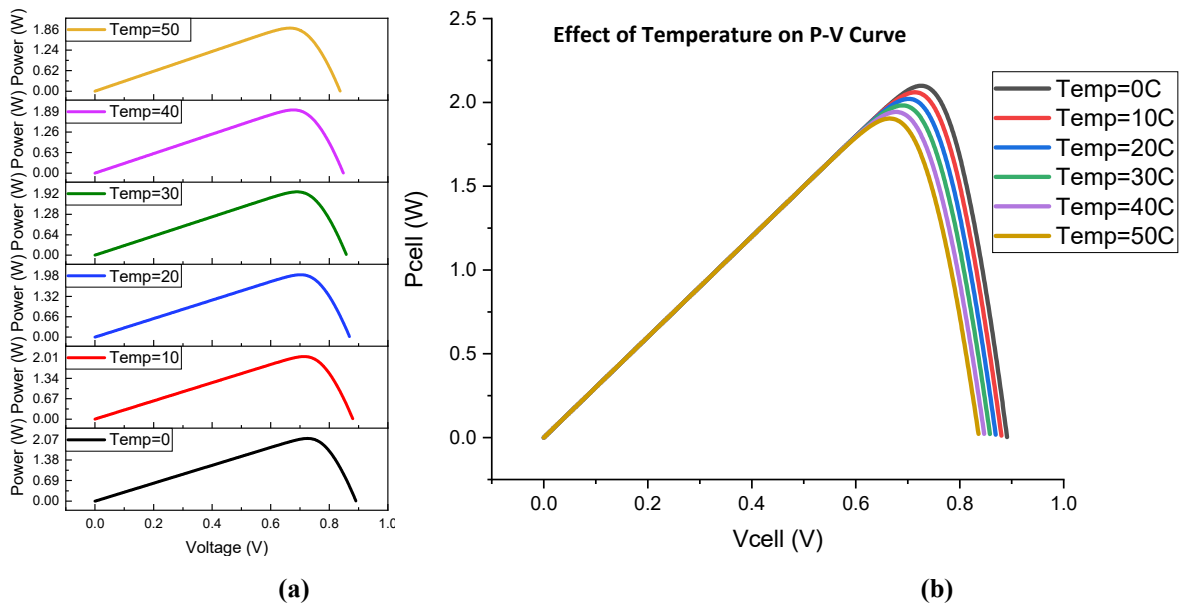


Figure 7. Temperature effect on P-V curve (a) Stacked (b) Batch

Solar cells, like all other semiconductor devices, are temperature sensitive. Increasing temperature, lowers the bandgap of a semiconductor, affecting the majority of its material characteristics. A reduction in a semiconductor's band gap as temperature rises might be interpreted as an increase in the energy of the material's electrons. As a result, less energy is required to break a connection. A decrease in bond energy decreases a bandgap in the bond model of a semiconductor bandgap. Open-circuit voltage is characteristic in a solar cell that is most impacted by temperature changes. The observed variations in parameters owing to rise in temperature are reported in table 2 based on the temperature impact simulations (Figure 6 and 7).

Table 2. Effect of temperature

Temperature (degree)	Open circuit voltage, V_{oc} (V)	Short circuit current, I_{sc} (A)	Maximum Power, P_{max} (W)
0	0.891136	2.99998	2.09897
10	0.880491	2.99997	2.05999
20	0.869756	2.99997	2.02095
30	0.858932	2.99996	1.98187
40	0.848023	2.99988	1.94276
50	0.837031	2.99984	1.90362

The open circuit voltage decreases with increasing temperature, while short circuit current decreases only little, according to simulation results. At 0-degree output power is maximum. Power progressively decreases because with temperature changes, current voltage (I-V) characteristic of an illuminated photovoltaic cell changes. According to solid state theory, the impact may be explained. Higher temperature lowers open-circuit voltage and short-circuits current, and hence same is true for the P-V curve. As a result, changes in temperature have an impact on the cell's overall performance. The cell performs well at low temperatures, but as temperature rises, efficiency of the cell decreases.

Irradiance Effect

The value of I_{ph} changes when the value of solar irradiance changes. The current in a short circuit is proportional to sun irradiation, G . A solar cell is seen to act like a 3A current source when exposed to 1000 Wm^{-2} sun irradiation. If the obtained ratio is $K_r = (3/1000)$, it is determined that the current sources for radiations of 1000 Wm^{-2} , 850 Wm^{-2} , 700 Wm^{-2} , 550 Wm^{-2} , 400 Wm^{-2} , and 250 Wm^{-2} are 3A, 2.55A, 2.1A, 1.65A, 1.2A, and 0.75A, respectively, using the equation;

$$I_{sc} = K_r * G \tag{11}$$

The series and shunt resistances are 0.03 ohms and 500 ohms, respectively, in the model. Figures 8 and 9 show simulations of I-V as well as P-V characteristics curves for various solar irradiances.

Table 3. Solar Cell Current (I_{sc}) effect by Irradiance (G)

I_{ph} (A)	$K_r = \frac{I_{sc}}{1000}$ (A)	G (Wm^{-2})	$I_{sc} = K_r * G$ (A)
3	0.003	1000	3
3	0.003	850	2.55
3	0.003	700	2.1
3	0.003	550	1.65
3	0.003	400	1.2
3	0.003	250	0.75

I_{sc} is the current of the solar cell affected by the solar irradiance. These currents are being used to observe the affect of solar irradiance on I-V and P-V curve of the solar cell. The variation in the solar irradiance majorly affects the performance of the solar cell shown below in the graphs.

As the solar insolation changes during the day, the I-V and P-V properties change as well. With rise in solar irradiance, open circuit voltage and short circuit current rises as well, causing maximum power point to shift downward. Solar cell performance is affected by irradiance, with a drop in sunshine resulting in a fall in current and, as a result, a loss in power production. The observed changes in parameters are presented in Table 4 resulting in a decrease in solar irradiation.

Open circuit voltage and short circuit current are lowered as sun irradiation reduced, according to the simulation results. The output power is highest when the irradiance is at its highest, then progressively decreases when the irradiance is reduced.

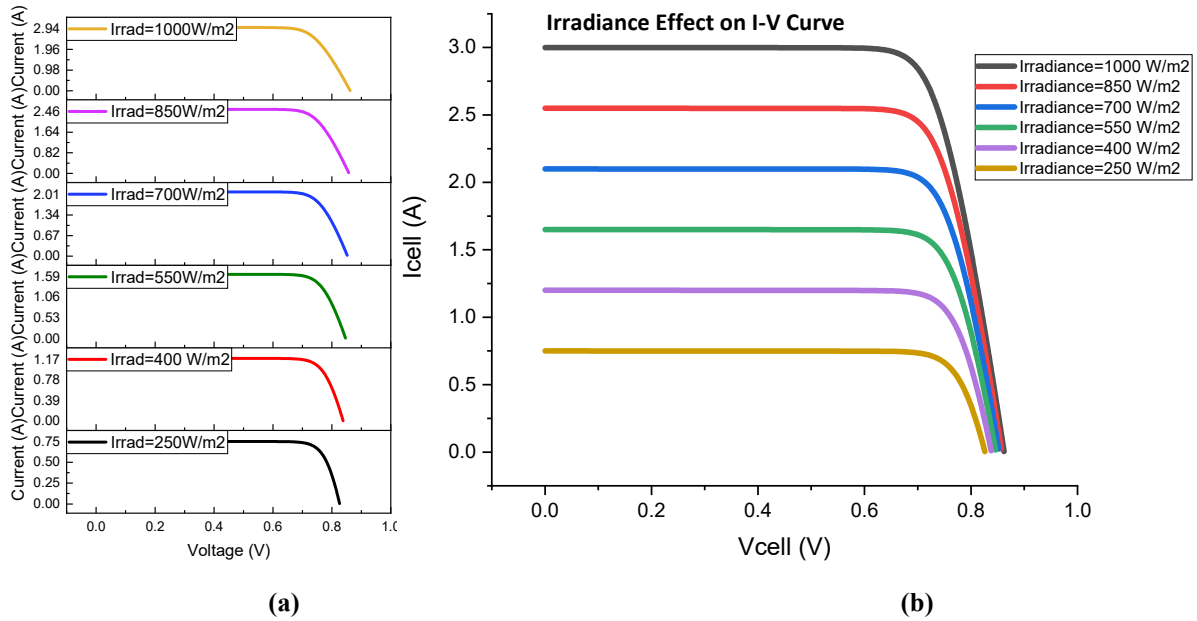


Figure 8. Irradiance effect on I-V curves (a) Stack (b) Batch

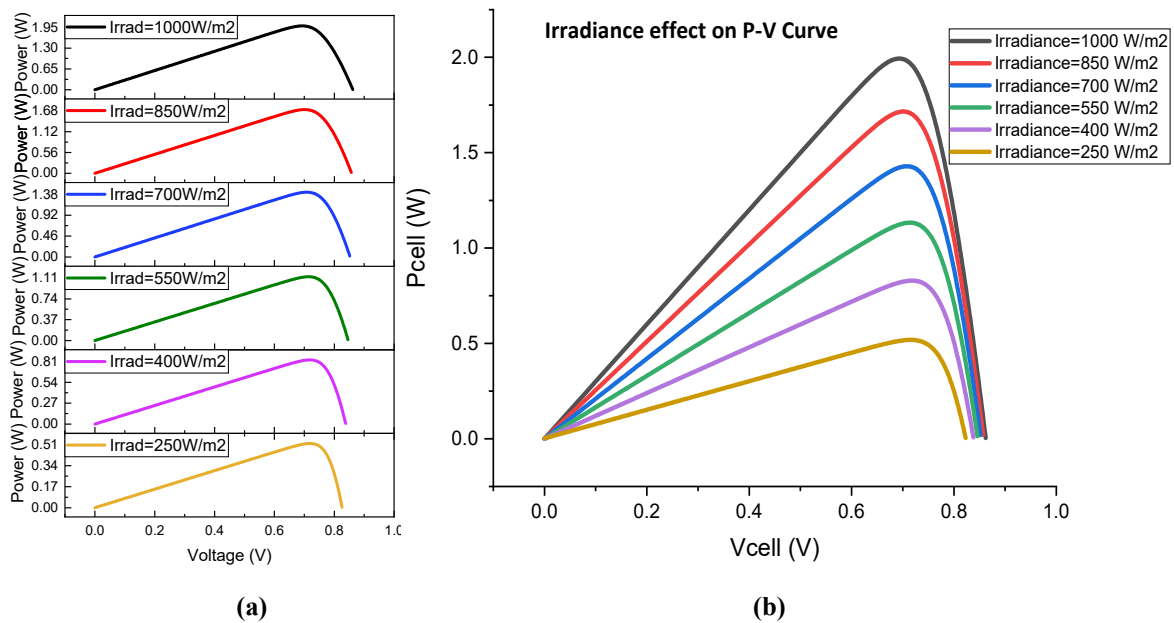


Figure 9. Irradiance effect on P-V curves (a) Stack (b) Batch

Table 4. Effect of Irradiance

Irradiance, G (Wm ⁻²)	Open circuit voltage, V _{oc} (V)	Short circuit current, I _{sc} (A)	Maximum Power, P _{max} (W)
250	0.826288	0.749955	0.518568
400	0.838466	1.19993	0.829345
550	0.846713	1.6499	1.13318
700	0.852957	2.09987	1.42888
850	0.857982	2.54985	1.71582
1000	0.862188	2.99982	1.99361

Effect of Change in Series Resistance

Figures 10 and 11 show the simulation results for various series resistance levels. The solar irradiation is set to 1000Wm⁻², temperature is set to 20°C, and shunt resistance is set to 500 ohms. 0.03 ohm, 0.3 ohm, 3 ohm, 4 ohms, and 5 ohms are the series resistance values utilized.

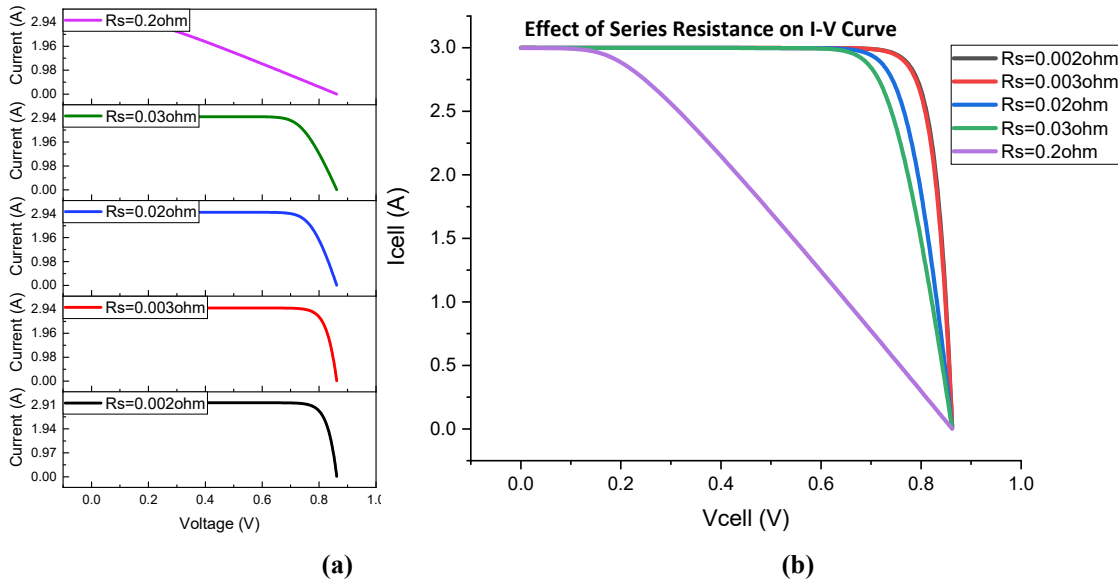


Figure 10. Effect of change of series resistance on I-V curve (a) Stack (b) Batch

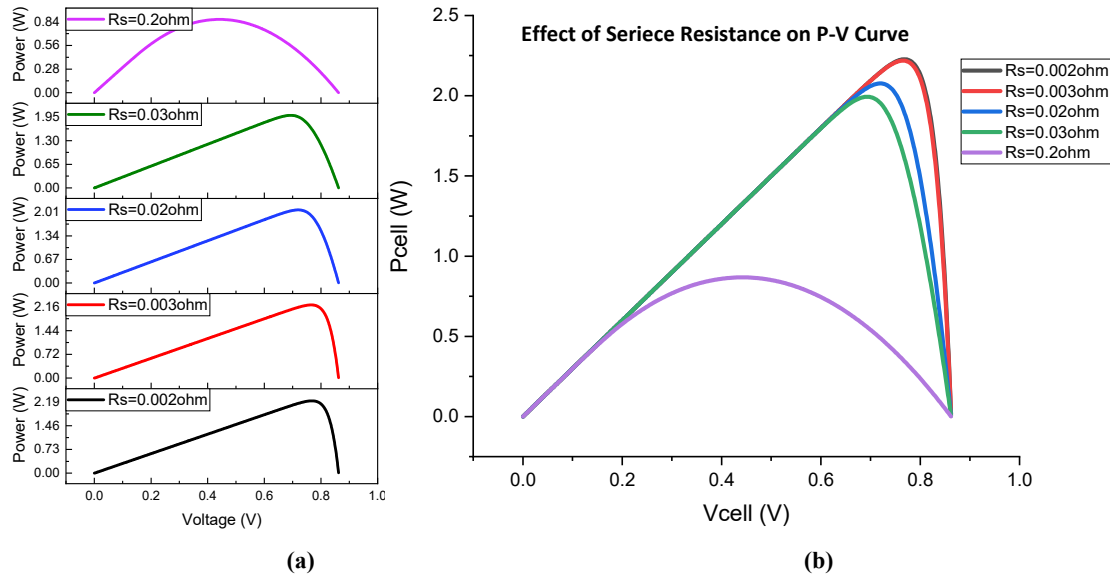


Figure 11. Effect of change of series resistance on P-V curve (a) Stack (b) Batch

At open-circuit voltage, series resistance has no effect on the solar cell since entire current flow through solar cell, and therefore via series resistance, is zero. Series resistance, on the other hand, has a significant impact on I-V curve at open-circuit voltage. Table 5 summarizes the observed variations owing to changes in series resistance.

Table 5. Effect of change of series resistance

Series resistance, R_s (Ohm)	Open circuit voltage, V_{oc} (V)	Short circuit current, I_{sc} (A)	Maximum Power, P_{max} (W)
0.002	0.862186	2.99999	2.22728
0.003	0.862187	2.99998	2.21887
0.02	0.862188	2.99988	2.0766
0.03	0.862188	2.99982	1.99361
0.2	0.862188	2.99868	0.867814

Short circuit current is lowered insignificantly when series resistance is raised, while short circuit current is reduced significantly for very high series resistance values. However, open circuit voltage stays same, whereas maximum output power is decreased. The flow of current between emitter and base of solar cell, contact resistance between metal contact and the absorber layer, and resistance of top and rear metal contacts are the three reasons of series resistance in a solar cell. Although extremely high values may also lower short-circuit current, the major effect of series resistance is to

diminish the fill factor. At open-circuit voltage, series resistance has no effect on solar cell since entire current flow through solar cell, and therefore via series resistance, is zero. Series resistance, on the other hand, has a significant impact on I-V curve at open-circuit voltage. Finding slope of I-V curve at open-circuit voltage point is a simple way to estimate series resistance of a solar cell.

Effect of Change in Shunt Resistance

Figures 12 and 13 illustrate the simulation for various shunt resistance levels. The irradiation of the sun is 1000Wm^{-2} , the temperature is 20°C , and the series resistance is $0.03\ \text{Ohm}$. $5000\ \text{Ohms}$, $1000\ \text{Ohms}$, $500\ \text{Ohms}$, $5\ \text{Ohms}$, and $0.05\ \text{Ohms}$ are the shunt resistance values.

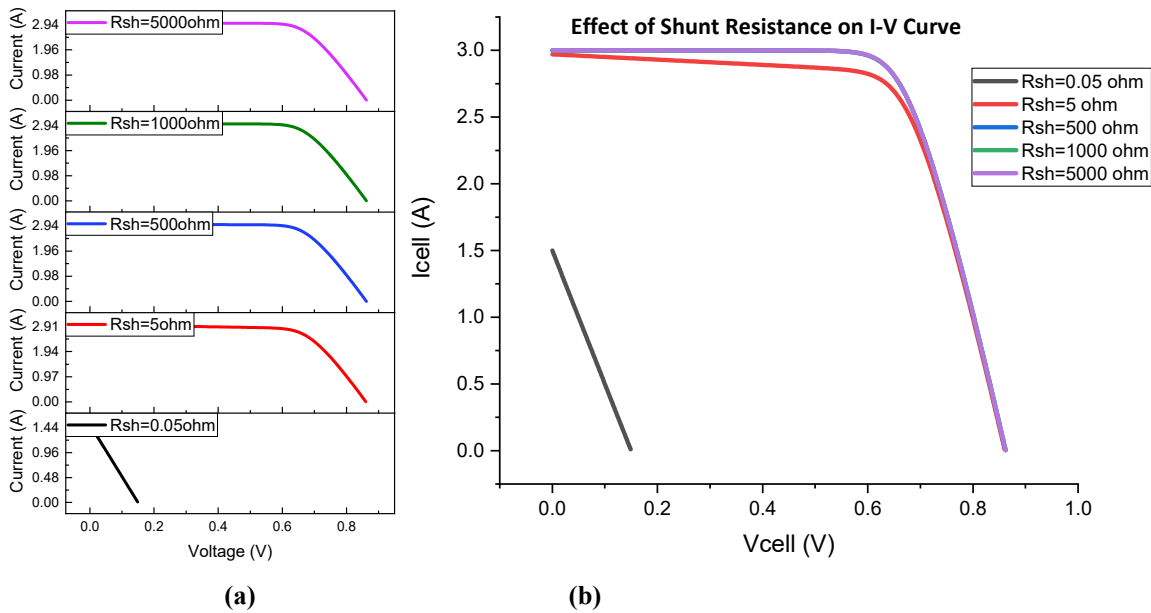


Figure 12. Effect of change of shunt resistance on I-V curve (a) Stack (b) Batch

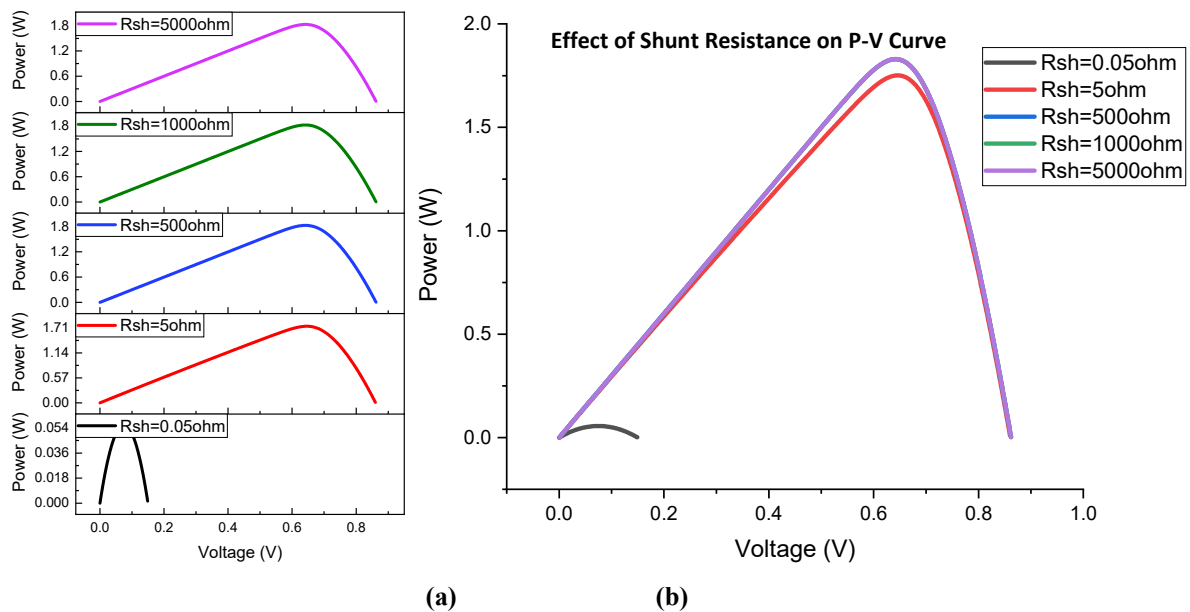


Figure 13. Effect of change of shunt resistance on P-V curve (a) Stack (b) Batch

By offering an additional current channel for light-generated current, low shunt resistance becomes the reason of power losses in solar cells. An amount of current passing through solar cell junction is reduced, and voltage from solar cell is reduced as a result of this diversion. Because there is less light-generated current at low light levels, effect of a shunt resistance is more severe. As a result, loss of this current due to shunt resistance has a greater impact on solar cell performance. Furthermore, at lower voltages, when solar cell's effective resistance is considerable, influence of a parallel resistance is significant. Table 4 summarizes the observed variations owing to changes in series resistance.

Table 6. Effect of change of shunt resistance

Shunt resistance, R_{sh} (Ohm)	Open circuit voltage, V_{oc} (V)	Short circuit current, I_{sc} (A)	Maximum Power, P_{max} (W)
0.05	0.150000	1.87500	0.0703125
5	0.860675	2.98211	1.89965
500	0.862188	2.99982	1.99361
1000	0.862196	2.99991	1.99408
5000	0.862201	2.99998	1.99446

The open circuit voltage decreases little as shunt resistance decreases, but it decreases considerably for very low shunt resistance values. The short circuit current is little impacted. The output power is decreased, and the power is very low for a very tiny shunt resistance.

Optimized Results

From the above results and discussion, we concluded that at $0^{\circ}C$ temperature, $1000w/m^2$ irradiance, 0.002 ohm series resistance and 5000 ohm shunt resistance give the fruitful results. The optimized values were simulated on 1D5P model solar cell as shown in the following circuit diagram.

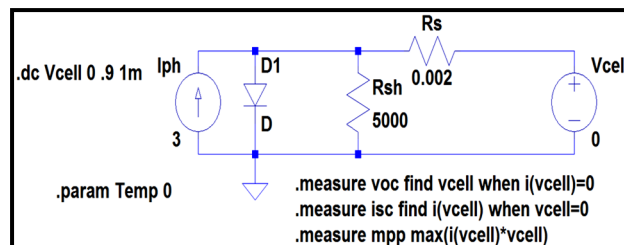


Figure 14. Real Valued Circuited simulated on optimum values

The effect of these optimum values is clearly shown in the following graphs.

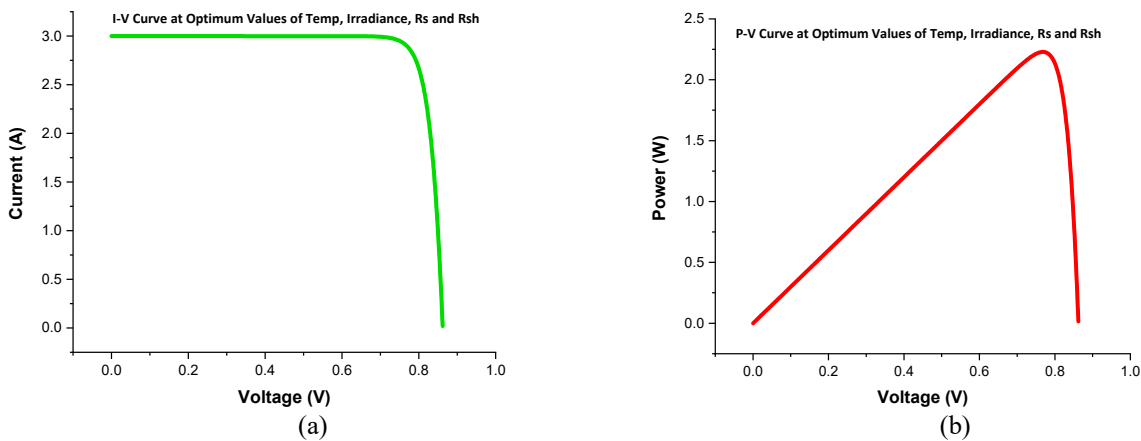


Figure 15. (a) I-V curve at optimum values (b) P-V curve at optimum values

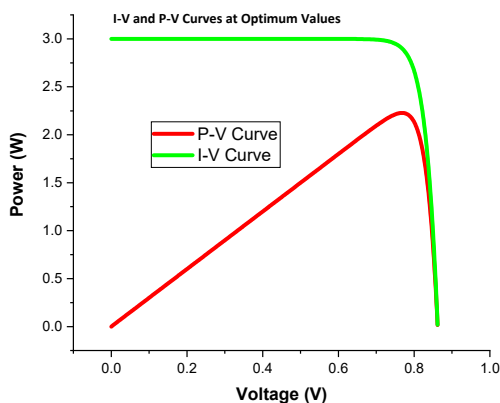


Figure 16. Improved I-V and P-V curves

From the above graphs it is clear that at the optimum values, the curves have become straighter showing the improvement in the performance of 1D5P model solar cell.

CONCLUSION

The numerical simulation was done with LTSpice. The short-circuit current and electrical characteristics of certain cell components such as the diode, shunt resistance, and series resistances are illustrated and analyzed using numerical data. These impacts are demonstrated using simulations. The major goal of the project is to measure output power under various environmental conditions such as temperature, solar irradiance. Changes in these parameters have a major impact on the PV cell's I-V and P-V characteristics curves. Temperature was varied from 0°C to 50°C. With increase in temperature the I-V and P-V curves were affected. Hence the case with solar irradiance varied from 250 to 1000 Wm⁻² was observed. The shunt and series resistances of the solar cell play an important role in the performance of the solar cell. Optimum values of the temperature, solar irradiance, shunt and series resistance values have been calculated for one diode five parameters (1D5P) solar cell.

FUTURE WORK

The presented work gave the effect of different parameters variations on I-V and P-V curves of 1D5P model solar pv cell. If a DC-DC converter is applied at the output of this model, the voltages and currents, and hence the power of the cell can be enhanced as well as the smooth curves can be obtained.

Acknowledgement

This work was supported by European Commission under project Erasmus+ (2019-1-ES01-KA107-062073), Coordinator University Polytechnic of Valencia, Spain, and Grant PID2019-107137RB-C22 funded by MCIN/AEI/10.13039/501100011033 and by “ERDF A way of making Europe.

ORCID IDs

 Muhammad Aamir Shafi, <https://orcid.org/0000-0001-9813-7029>;  Hanif Ullah, <https://orcid.org/0000-0002-0529-973X>
 Laiq Khan, <https://orcid.org/0000-0003-3659-3824>;  Bernabe Mari, <https://orcid.org/0000-0003-0001-419X>

REFERENCES

- [1] W.M. Chen, H. Kim, and H. Yamaguchi, Renewable energy in eastern Asia: Renewable energy policy review and comparative SWOT analysis for promoting renewable energy in Japan, South Korea, and Taiwan, *Energy Policy*, **74**, 319 (2014), <https://doi.org/10.1016/j.enpol.2014.08.019>
- [2] L. El Chaar, and N. El Zein, Review of photovoltaic technologies, *Renewable and sustainable energy reviews*, **15**(5), 2165 (2011), <https://doi.org/10.1016/j.rser.2011.01.004>
- [3] R.N. Shaw, P. Walde, and A. Ghosh, Effects of solar irradiance on load sharing of integrated photovoltaic system with IEEE standard bus network, *Int. J. Eng. Adv. Technol.*, **9**(1), 424 (2019), <http://www.doi.org/10.35940/ijeat.A9410.109119>
- [4] D. Meneses-Rodríguez, P.P. Horley, J. Gonzalez-Hernandez, Y.V. Vorobiev, and P.N. Gorley, Photovoltaic solar cells performance at elevated temperatures, *Solar energy*, **78**(2), 243 (2005), <https://doi.org/10.1016/j.solener.2004.05.016>
- [5] M.A. Rahman, S. Hasan, and M.J. Ferdous, *An Investigation into efficiency improvement of thin film solar cell* (Doctoral dissertation, Department of Electrical, Electronics and Communication Engineering (EECE), (MIST, 2011).
- [6] T. Ahmad, S. Sobhan, and M.F. Nayan, Comparative analysis between single diode and double diode model of PV cell: concentrate different parameters effect on its efficiency, *Journal of Power and Energy Engineering*, **4**(3), 31 (2016), <http://dx.doi.org/10.4236/jpee.2016.43004>
- [7] S. Gallardo-Saavedra, and B. Karlsson, Simulation, validation and analysis of shading effects on a PV system, *Solar Energy*, **170**, 828 (2018), <https://doi.org/10.1016/j.solener.2018.06.035>
- [8] S.P. Philipps, W. Guter, E. Welsler, J. Schöne, M. Steiner, F. Dimroth, and A.W. Bett, in: *Next Generation of Photovoltaics*, edited by C.A. López, M.A. Vega, L.A. López, (Springer, Berlin, Heidelberg, 2012). pp. 1-21, https://doi.org/10.1007/978-3-642-23369-2_1
- [9] M. Karlsson, *Comparison and evaluation of hardware modeling and simulation tools*, M.Sc. Thesis, Jönköping Institute of Technology, 2011.
- [10] N. Sultana, M.A. Ahad, and K. Hassan, *Simulation and Analysis of the Effect of Change of Different Parameters on the Characteristics of PV Cell Using LTSpiceIV*, *International Journal of Science and Research*, **4**(2), 63 (2015), <https://www.ijsr.net/archive/v4i2/SUB15942.pdf>
- [11] D. Diouf, Y.M. Soro, A. Darga, and A.S. Maiga, Module parameter extraction and simulation with LTSpice software model in sub-Saharan outdoor conditions, *African Journal of Environmental Science and Technology*, **12**(12), 523 (2018), <https://doi.org/10.5897/AJEST2018.2566>
- [12] R. Abbassi, A. Abbassi, M. Jemli, and S. Chebbi, Identification of unknown parameters of solar cell models: A comprehensive overview of available approaches, *Renewable and Sustainable Energy Reviews*, **90**, 453 (2018), <https://doi.org/10.1016/j.rser.2018.03.011>
- [13] P.A. Kumari, and P. Geethanjali, Parameter estimation for photovoltaic system under normal and partial shading conditions: A survey, *Renewable and Sustainable Energy Reviews*, **84**, 1 (2018), <https://doi.org/10.1016/j.rser.2017.10.051>
- [14] V. Tamrakar, S.C. Gupta, and Y. Sawle, Study of characteristics of single and double diode electrical equivalent circuit models of solar PV module. In: *International Conference on Energy Systems and Applications*, (IEEE, 2015), pp. 312-317.
- [15] H.P. Gavin, <https://people.duke.edu/~hpgavin/ce281/lm.pdf>
- [16] F. Dkhichi, B. Ouarkfi, A. Fakkar, and N. Belbounaguia, Parameter identification of solar cell model using Levenberg–Marquardt algorithm combined with simulated annealing, *Solar Energy*, **110**, 781 (2014), <http://dx.doi.org/10.1016%2Fj.solener.2014.09.033>

- [17] E.M.G. Rodrigues, R. Melicio, V.M.F. Mendes, and J.P. Catalao, Simulation of a solar cell considering single-diode equivalent circuit model, in: *International conference on renewable energies and power quality*, (Spain, 2011), pp. 13-15.
- [18] V. Tamrakar, S.C. Gupta, and Y. Sawle, Study of characteristics of single and double diode electrical equivalent circuit models of solar PV module, in: *International Conference on Energy Systems and Applications* (IEEE, 2015), pp. 312-317.
- [19] Alternative Energy Tutorials, <https://www.alternative-energy-tutorials.com/photovoltaics/solar-cell-i-v-characteristic.html>.
- [20] B.V. Chikate, Y. Sadawarte, and B.D.C.O.E. Sewagram, The factors affecting the performance of solar cell, *International journal of computer applications*, 1(1), 0975 (2015), <http://research.ijcaonline.org/icquest2015/number1/icquest2776.pdf>
- [21] B.K. Dey, I. Khan, N. Mandal, and A. Bhattacharjee, (2016, October). Mathematical modelling and characteristic analysis of Solar PV Cell, in: *7th Annual Information Technology, Electronics and Mobile Communication Conference (IEMCON)*, (IEEE, 2016), pp. 1-5.

ВПЛИВ ПАРАЗИТНИХ ПАРАМЕТРІВ ТА УМОВ СЕРЕДОВИЩА НА I-V ТА P-V ХАРАКТЕРИСТИКИ МОДЕЛІ 1D5P СОНЯЧНОГО ЕЛЕМЕНТА З ВИКОРИСТАННЯМ LTSPICE-IV

Мухаммад Аамір Шафі^{a,e,f}, Муніб Хан^b, Сумайя Бібі^c, Мухаммад Ясір Шафі^b, Норіна Раббані^d, Ханіф Улла^e, Лайк Хан^a, Бернабе Марі^f

^aФакультет електротехніки, Університет COMSATS Ісламабад, Пакистан

^bФакультет електротехніки, Інститут Південного Пенджаба Мултана, Пакистан

^cФакультет електротехніки, Університет Бахауддіна Закарії, Мултан, Пакистан

^dФакультет електротехніки, Університет науки та інформаційних технологій Сархад, Пешавар, Пакистан

^eЕлектронний факультет електротехніки, Федеральний університет мистецтв, науки і техніки Урду, Ісламабад, Пакистан

^fІнститут дизайну та виробництва (IDF), Політехнічний університет Валенсії (UPV), Іспанія

У цій дослідницькій роботі виконано електричне моделювання сонячної батареї моделі 1D5P за допомогою програмного забезпечення моделювання LTSpice-IV. У цій роботі здійснювався вплив умов навколишнього середовища, тобто температури, сонячного опромінення, а також паразитних параметрів, послідовних шунтів. Було виявлено, що в міру підвищення температури продуктивність сонячних батарей знижується, оскільки температура призводить до посилення явища рекомбінації і, отже, до зниження продуктивності. Однак, коли температура підвищується від 0°C до 50°C, криві I-V і P-V переміщуються до початку координат, показуючи негативний вплив підвищення температури на сонячний елемент. Сонячне опромінення відіграє важливу роль у продуктивності сонячних елементів. Зі збільшенням сонячного опромінення з 250 Вт·м⁻² до 1000 Вт·м⁻² продуктивність сонячного елемента відповідно збільшується, і крива I-V, а також P-V віддаляється від початку координат. Зроблено висновок, що для різних послідовних опорів I V разом із P-V характеристикою сонячного елемента моделі 1D5P змінюється, оскільки при послідовному опорі 0,02 Ом отримується максимальний струм короткого замикання та максимальна потужність. Але коли послідовний опір збільшився лише на 2 Ом, криві I-V і P-V різко рухаються до початку координат. Опір шунта – це шлях до зміни струму елементу. Зі збільшенням опору шунта шлях зворотного струму зменшується, отже, весь струм йде на навантаження, отже, досягається максимальна потужність. Аналогічно, коли значення опору шунта зменшується, керована напругою ділянка кривої вольт-амперних характеристик переміщується ближче до початку координат, що знижує продуктивність сонячних елементів. Важливо зрозуміти, як різні фактори впливають на криві I-V і P-V характеристик сонячних елементів. Напруга холостого ходу, струм короткого замикання та максимальна потужність змінюються. Вплив цих факторів може бути надзвичайно корисним при відстеженні найвищої точки потужності сонячної батареї різними методами.

Ключові слова: сонячна батарея, 1D5P, моделювання, температура, освітленість, LTSpice

BORON ISOTOPIC RATIO ($\delta^{11}\text{B}$) MEASUREMENTS IN BORON CARBIDE (B_4C): BENCHMARKING BETWEEN SF-ICP-MS AND PIGE TECHNIQUES[†]

 Dmytro Kutnii*,  Stanislav Vanzha,  Dmytro Burdeynyi,  Volodymyr Levenets, O. Omelnik, A. Shchur

National Science Center “Kharkiv Institute of Physics and Technology” of NAS of Ukraine

*Corresponding Author: d_kutnii@kipt.kharkov.ua

Received February 16, 2022; accepted March 30, 2022

The results of comparing the analytical capabilities of Sector Field Inductively Coupled Plasma Mass Spectrometry (SF-ICP-MS) and Particle Induced Gamma-ray Emission (PIGE) methods for determining the $^{11}\text{B}/^{10}\text{B}$ isotope ratio in boron carbide samples (B_4C) are presented. The following nuclear reactions excited by protons on the stable boron isotopes are considered: $^{10}\text{B}(\text{p},\alpha\gamma)^7\text{Be}$, $^{10}\text{B}(\text{p},\text{p}\gamma)^7\text{Be}$ and $^{11}\text{B}(\text{p},\gamma)^{12}\text{C}$. The optimum proton energy range was determined to be within 550 to 600 keV, while the energies of the induced gamma-radiation that can be used for quantitative estimation of the boron isotopes were 429 keV and 4439 keV for the isotopes ^{10}B and ^{11}B , respectively. Considering the uncertainties of measurements, the data for the $^{11}\text{B}/^{10}\text{B}$ isotope ratios, measured by the SF-ICP-MS and PIGE methods, are found to correlate with each other; yet they are characterized by a systematic bias. The uncertainty of measurements by the PIGE method was somewhat higher in comparison with SF-ICP-MS, and ranged from $\pm 4.1\%$ to $\pm 4.3\%$, and from $\pm 1.1\%$ to $\pm 3.5\%$, respectively.

Keywords: ICP-MS, PIGE, boron carbide, isotopic ratio, nuclear application, benchmarking

PACS: 29.30. Ep, 29.30. Kv

Boron has two naturally occurring isotopes ^{10}B (19.9 %) and ^{11}B (80.1 %). Due to a relatively large mass difference (10 %) between the two isotopes and high volatility, the boron isotopic ratio ranges from -70 to $+60\%$ in natural materials (rocks, natural waters and sediments), and is used as a tracer for studying continental weathering, plate subduction processes, pH variability in the oceans and anthropogenic pollution [1]. Boron isotopic ratios are conventionally expressed in delta notation ($\delta^{11}\text{B}$), which denotes the deviation of measured $^{11}\text{B}/^{10}\text{B}$ ratios from the standard (in parts per thousand), using the equation below [2]:

$$\delta^{11}\text{B}(\%) = \left[\frac{(^{11}\text{B}/^{10}\text{B})_{\text{meas.}}}{(^{11}\text{B}/^{10}\text{B})_{\text{NIST951}}} - 1 \right] \cdot 10^3,$$

where $(^{11}\text{B}/^{10}\text{B})_{\text{NIST951}} = 4.04362 \pm 0.00137$ is the abundance ratio from the accepted international reference material NIST SRM 951 (boric acid).

The accurate knowledge of the boron isotope ratio is of particular importance for neutron-absorbing materials in nuclear reactors. In a boiling water reactor (BWR) and a fast breeder reactor (FBR), boron carbide (B_4C) serves as a neutron-absorbing material for the control rods. Furthermore, in a pressurized water reactor (PWR), a solution of boric acid (H_3BO_3) is added to the primary cooling water to adjust the reactivity of the reactor core [3]. The boron isotopic ratio is one of the most important parameters that qualifies the applicability of B_4C in the nuclear reactor, considering due to the fact that the isotope ^{10}B has a significantly higher thermal neutron absorption cross-section compared to ^{11}B , namely 3840 barn vs. about 0.005 barn [4].

The isotope composition control is also of importance for predicting the material behavior under irradiation conditions, when even a minor variation in the isotopic abundance ratio may cause a substantial change in material properties.

The traditional method for determining the isotopic composition of boron ($\delta^{11}\text{B}$) most accurately (RSD of $\pm 0.3\%$) is the thermal ionization mass-spectrometry (TIMS). Other mass-spectrometric methods with ionization in inductively coupled plasma (ICP-MS) are also widely used for measuring various isotopic ratios. In the boron analysis case, the MC-ICP-MS multicollector systems can provide measurement uncertainty $\pm 0.2\%$. For double focusing sector field mass-spectrometers SF-ICP-MS, the typical value of uncertainty is $\pm 2\%$, and for quadrupole-based mass-spectrometers Q-ICP-MS it makes $\delta^{11}\text{B} \pm 15\%$ [5-8].

Furthermore, for isotopic analysis, nuclear physics methods are also used, which involve the Rutherford ion backscattering spectrometry, and also, the nuclear reactions excited by charged particles and neutrons on different isotopes of one and the same chemical element [9-11].

[†] Cite as: D. Kutnii, S. Vanzha, D. Burdeynyi, V. Levenets, O. Omelnik, and A. Shchur, East Eur. J. Phys. 2, 75 (2022), <https://doi.org/10.26565/2312-4334-2022-2-08>

This paper presents the results of benchmarking between the SF-ICP-MS and PIGE methods at determining the $^{11}\text{B}/^{10}\text{B}$ isotope ratio in boron carbide samples (B_4C). The traditional mass-spectrometric methods for determining isotopic composition provide high precision, but, on the other hand, often require labor-intensive sample preparation, such as chemical purification of the analyte, and expensive auxiliary equipment. In this context, the PIGE is considered as an alternative nondestructive express-method for measuring the ^{10}B and ^{11}B isotopic abundance in the field of nuclear applications.

MATERIALS AND METHODS

The samples used in the measurements were B_4C powders with different particle sizes varying from 50 to 70 μm . For purposes of the studies, pellets-targets were prepared from boron of natural isotopic composition and ^{10}B enriched. The pellets of diameter 9 mm were made by pressing the B_4C powder under pressure of 25 kg/cm^2 for 3 minutes.

Amorphous boron powder enriched to 96.2 % at. in the ^{10}B isotope (produced by the National High Technology Centre of Georgia) was used as a reference material to assure the accuracy of boron isotope measurements and to correct the isotopic ratios in the samples for mass bias. No additional drying or homogenization was carried out on the reference material.

The boron isotope measurements were performed using a double-focusing magnetic sector inductively coupled plasma mass spectrometer equipped with a single electron multiplier SF-ICP-MS ELEMENT 2 (Thermo Fisher Scientific GmbH, Germany); its technical characteristics are given in Table 1. All measurements were carried out in the low mass resolution mode ($m/\Delta m = 300$).

Table 1. Technical characteristics of SF-ICP-MS ELEMENT 2

Mass range	from 2 to 264 a.m.u.
Sensitivity	$\sim 10^6$ cps for 1 ppb ^{115}In
Detection limit	1 ppq for non-interfering elements
Dark noise	< 0.2 cps
Dynamic range	$> 10^9$
Mass resolution	low (300), middle (4000), high (10000) at 10 % peak height
Signal stability	better than 1 % for 10 min.

Thermo Tuning Solution A, containing the elements ^7Li , ^9Be , ^{59}Co , ^{115}In , ^{138}Ba , ^{140}Ce , ^{206}Pb and ^{238}U at 10 $\mu\text{g L}^{-1}$, was used for tuning.

The samples were introduced into the SF-ICP-MS through a Nd:YAG deep UV (213 nm) laser ablation system NWR-213 (New Wave Research, Inc., USA). The generated plume was transported from the laser ablation cell to the SF-ICP-MS plasma by means of a laminar flow of Ar gas. Further details on the optimized instrumental settings as well as on the applied data acquisition parameters are reported elsewhere [12].

The nuclear physical analytical complex SOKOL (NSC Kharkiv Institute of Physics and Technology, Ukraine) was used to determine the boron isotopic ratio by the PIGE method [13].

The targets were placed into the multi-position cassette located in the irradiation chamber, which was evacuated to a pressure lower than 10^{-6}MPa , and were alternately exposed with a proton beam under identical conditions. The current integrator was used to measure the proton beam current, while the chamber itself, being out of contact with the ion guide, the vacuum and adjusting systems served as a Faraday cup.

The accelerator energy calibration was performed against the resonances of 991.2 keV protons and 1779 keV gamma-quanta from the $^{27}\text{Al}(p,\gamma)^{28}\text{Si}$ reaction.

The protons were incident on the target along the normal to its surface. The beam projection on the target represented a circle 3 mm in diameter.

The gamma-quanta were registered by a Ge(Li) detector located outside the chamber, at a distance of 1.5 cm from the target and at a 0° angle to the proton beam direction. The energy resolution (FWHM) of the detector at the 661 keV line was 1.5 keV.

The characteristic X-ray excited in the samples was registered by a Si-pin detector with the crystal measuring 3 mm \times 500 μm . The detector, having the 165 keV energy resolution at 6.4 keV line, was located outside the chamber, at a distance of 4.5 cm from the target and at a 135° angle to the proton beam direction. The characteristic X-ray was extracted from the chamber and was guided to the detector through the window made from a 25 μm thick Be-foil. A polyethylene absorber 150 μm thick was used to suppress low-energy radiation. To eliminate the edge effects during the X-ray registration by the detector, a 5 mm thick aluminum collimator, having a hole with diameter of 1.5 mm, was arranged between the detector and the target.

The optimum measuring conditions have been established and a series of measurements of gamma-ray spectra from both natural and ^{10}B -enriched samples was performed. In the experiments, the proton energy was 600 keV, the beam current – 500 nA, the proton charge on the target varied from 200 to 500 μC . Five replicate measurements were performed for each of the samples.

The prepared sample pellets were placed into the laser ablation chamber. The raw data obtained by the SF-ICP-MS analysis were first corrected for the gas blank. The boron isotopic ratios were calculated subsequently as the ratios of the background-corrected signals after ablation. All the results reported here are based on five replicate measurements of each sample. All indicated uncertainties are the combined standard uncertainties and include a coverage factor of 2.

The mass bias correction was calculated using a boron powder enriched in the ^{10}B isotope to 96.2 % at. The signal intensity ratio of each sample was corrected by multiplying the mass bias coefficient thus obtained from the signal intensity ratio of boron powder enriched in the isotope ^{10}B .

For many years now the nuclear physics methods have been used for the analysis of elemental and isotopic composition of substances, as well as for studies of spatial distribution of matrix and impurity elements, including the depth distribution gradients, i.e., the concentration profiles [14].

Table 2 lists the data for proton-excited nuclear reactions on stable boron isotopes, which can be used to determine the isotopic composition.

Table 2. Data for proton-excited nuclear reactions on stable boron isotopes

Reaction	Gamma energy, keV	Resonance energy, keV	Resonance width, keV	Resonance cross-section, barn	Reference
$^{10}\text{B}(p,\alpha\gamma)^7\text{Be}$	429	None	-	-	[15]
$^{10}\text{B}(p,\gamma)^7\text{Be}$	718	None	-	-	[15]
$^{11}\text{B}(p,\gamma)^{12}\text{C}$	4439, 11680, 16110	163	7	0.157	[16]

As is evident from Table 2, for determination of the ^{10}B isotope, gamma-quanta of energies 429 keV and 718 keV can be used. In the process, as the experimental data demonstrate, the 429 keV radiation appears much more intense. For the ^{11}B isotope analysis, it is advantageous to use 4439 keV gamma-quanta, because the registration efficiency of 11680 keV and 16110 keV quanta is appreciably lower. In the proton energy range up to 600 keV, the contribution of 4439 keV gamma-quanta to the peak is mainly due to the resonance at a proton energy of 163 keV, and hence, the radiation intensity in this energy range remains essentially the same. Yet, at proton energies above 600 keV, the emission of 429 keV gamma-quanta from the $^{10}\text{B}(p,\alpha\gamma)^7\text{Be}$ reaction substantially increases, and this complicates the operation of the spectrometer. Then, for determination of the boron isotopic composition, it is expedient to measure the gamma-ray spectra at proton energies ranging from 550 to 600 keV.

RESULTS AND DISCUSSIONS

Figures 1a, 1b show the gamma-ray spectra, measured under the above-described conditions, with the use of samples from boron of natural composition and boron enriched in the ^{10}B isotope.

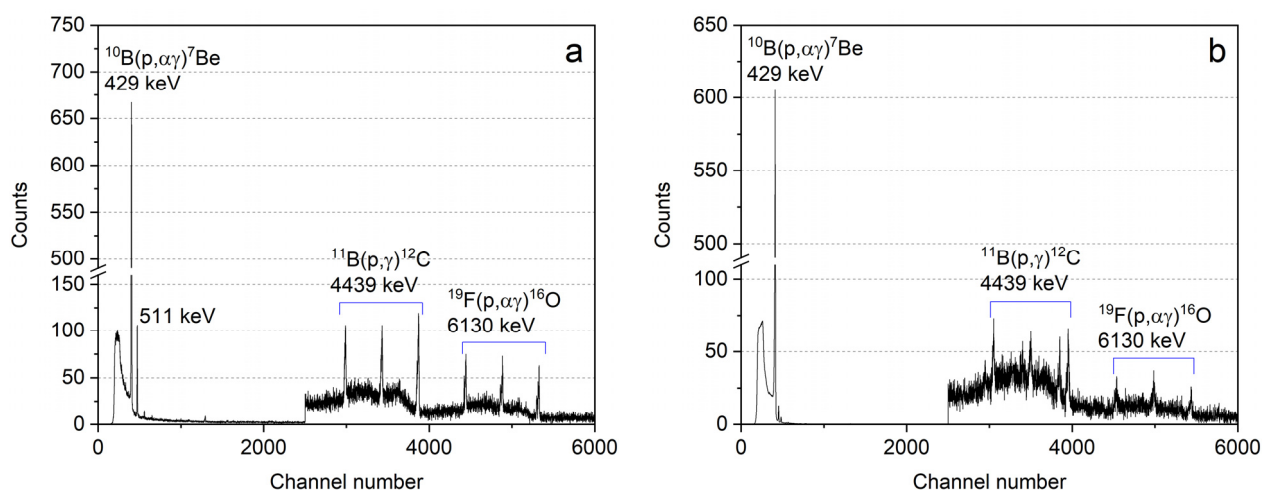


Figure 1. Spectra of gamma radiation induced by proton irradiation of boron samples: a – sample of natural isotopic composition; b – sample enriched with ^{10}B

As is obvious from the spectra, in the proton energy range under consideration, the gamma-radiation intensity resulting from the reaction on the ^{10}B nuclei is considerably higher than that from the reaction on the ^{11}B nuclei. With increase in the proton energy, the intensity of the 429 keV gamma radiation from the $^{10}\text{B}(p,\alpha\gamma)^7\text{Be}$ reaction strongly increases, thereby complicating the operation of the spectrometer, in particular, for registration of a substantially less intense 4439 keV gamma-rays from the $^{11}\text{B}(p,\gamma)^{12}\text{C}$ reaction.

Figure 2 shows the SF-ICP-MS and PIGE measurement data on the $^{11}\text{B}/^{10}\text{B}$ isotopic ratios for four B_4C samples in comparison with the reference ($^{11}\text{B}/^{10}\text{B}$)_{NIST951} values.

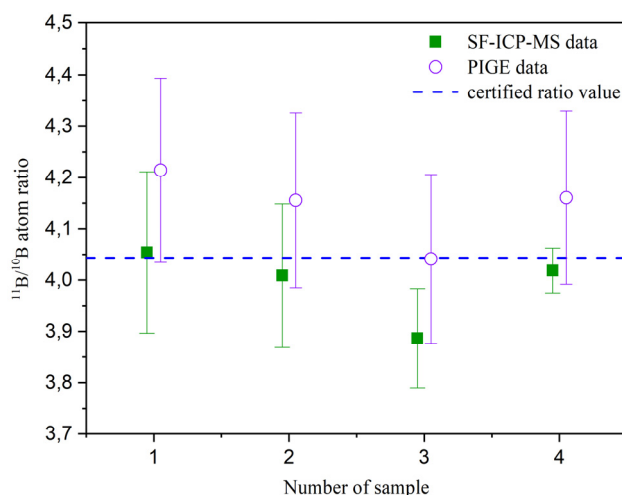


Figure 2. $^{11}\text{B}/^{10}\text{B}$ isotopic ratios in four samples of boron carbide measured by SF-ICP-MS and PIGE methods vs accepted international reference value 4.04362 ± 0.00137

With allowance made for the uncertainties of measurements, the data are seen to correlate between themselves, but at the same time, they are characterized by a systematic bias. The use of the SF-ICP-MS technique allows one to assume that the isotopic composition of one of the B_4C samples under analysis is probably not natural, whereas the PIGE data show no difference in the said samples. On the whole, the uncertainty of the PIGE data appears somewhat higher compared to the SF-ICP-MS measurement results, ranging from $\pm 4.1\%$ to $\pm 4.3\%$ versus $\pm 1.1\%$ to $\pm 3.5\%$, respectively.

Figures 3 and 4 show the estimates of statistical correlation and agreement of the SF-ICP-MS and PIGE measurement data, as determined by the regression analysis and the Bland-Altman comparison, respectively.

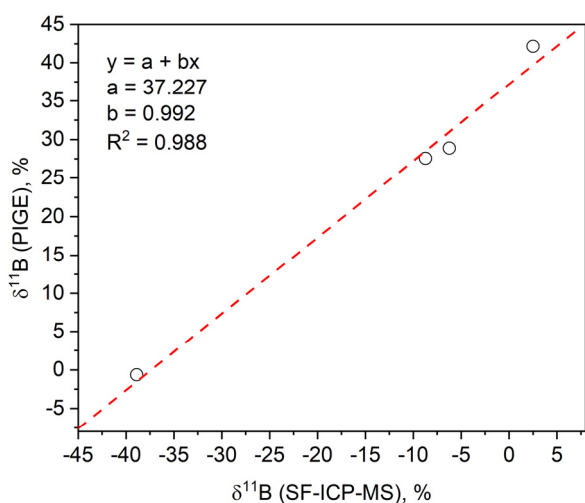


Figure 3. Relation between $\delta^{11}\text{B}$ determined by both SF-ICP-MS and PIGE for all B_4C samples and their linear approximation

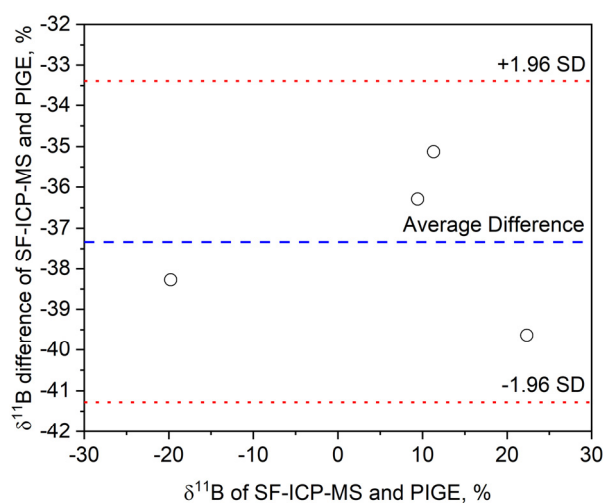


Figure 4. Bland-Altman comparison of the SF-ICP-MS and PIGE $\delta^{11}\text{B}$ determinations of B_4C samples

As can be seen from the scatter diagram in Fig. 3, there is strong correlation between the two methods. The calculated linear regression equation is given by: $y = 37.227 + 0.992 \cdot x$ with the coefficient of determination (R-Square) being close to 1. But, it is important to note that the correlation is not the same as the agreement. In some cases, the regression analysis may lead to improper conclusions. This just relates to the problems of comparing two measuring techniques, when the choice of independent variable is ambiguous.

In order to more readily see the difference between the two measurement techniques, it is useful to plot the means of each pair of measurements versus the difference between the measurements. Such a plot is known as the Bland-Altman Plot, which is shown in Fig. 4. The average difference in $\delta^{11}\text{B}$ values measured by SF-ICP-MS and PIGE is -37.3 and there is no tendency for the difference to vary with variation of isotopic ratios. The limits of agreement within 95% of the differences expected were calculated according to the Bland-Altman approach as to be -41.3 and -33.4 . The

agreement of the SF-ICP-MS and PIGE methods is confirmed by the fact that the values in Fig. 4 are clustered around the mean of the differences, and certainly within two standard deviations of the mean.

CONCLUSIONS

Benchmarking assessment of the boron isotopic ratio values measured in boron carbide by both the SF-ICP-MS and PIGE techniques has been performed. As nuclear reactions excited by protons on stable boron isotopes, consideration has been given to the $^{10}B(p,\alpha\gamma)^7Be$, $^{10}B(p,\gamma)^7Be$ and $^{11}B(p,\gamma)^{12}C$ reactions. The optimum proton energy range has been determined to be between 550 and 600 keV. The induced gamma-radiation energies, which may be used for quantitative estimation of boron isotopes, have been found to be 429 keV and 4439 keV for the isotopes ^{10}B and ^{11}B , respectively. It has been demonstrated that with allowance for measurement uncertainties, the isotopic ratio $^{11}B/^{10}B$ values measured by the SF-ICP-MS and PIGE methods correlate with each other, yet at the same time, are characterized by a systematic bias. The uncertainty in the PIGE data is somewhat greater compared to the SF-ICP-MS data, namely, it varies from $\pm 4.1\%$ to $\pm 4.3\%$ and from $\pm 1.1\%$ to $\pm 3.5\%$, respectively. The agreement of the SF-ICP-MS and PIGE methods has been confirmed by the Bland-Altman comparison.

ORCID IDs

 Kutnii Dmytro, <https://orcid.org/0000-0001-9591-4013>;  Vanzha Stanislav, <https://orcid.org/0000-0003-0949-947X>
 Burdejnyi Dmytro, <https://orcid.org/0000-0003-4431-7264>;  Volodymyr Levenets, <https://orcid.org/0000-0002-6439-0576>

REFERENCES

- [1] C. Voster, L. Greef, and P. Coetzee, S. Afr. J. Chem. **63**, 207 (2010), http://www.scielo.org.za/scielo.php?script=sci_arttext&pid=S0379-43502010000100033&lng=en&nrm=iso
- [2] K. Tirez, W. Brusteen, D. Widory, E. Petelet, A. Bregnot, D. Xue, P. Boeckx, and J. Bronders, J. Anal. At. Spectrom. **25**, 964 (2010), <https://doi.org/10.1039/C001840F>
- [3] I. Takasaki, T. Nagumo, T. Inaba, N. Yoshino, and T. Maruyama, J. Nucl. Sci. Technol. **49**(8), 867 (2012), <https://doi.org/10.1080/00223131.2012.703946>
- [4] Nuclear Data Center, Japan Atomic Energy Agency. *Boron Cross Sections*. <https://www.ndc.jaea.go.jp/cgi-bin/Tab80WWW.cgi?lib=J40&iso=B010>.
- [5] J.S. Becker, J. Anal. At. Spectrom. **17**, 1172 (2002), <https://doi.org/10.1039/B203028B>
- [6] J. Aggarwal, F. Böhm, G. Foster, S. Halas, B. Hönisch, S.-Y. Jiang, J. Kosler, et al. J. Anal. At. Spectrom. **24**, 825 (2009), <https://doi.org/10.1039/B815240C>
- [7] S. Kasemann, D. Schmidt, J. Bijma, and G. Foster, Chem. Geol. **260**(1), 138 (2009), <https://doi.org/10.1016/j.chemgeo.2008.12.015>
- [8] P. Coetzee, and F. Vanhaecke, Anal. Bioanal. Chem. **383**, 977 (2005), <https://doi.org/10.1007/s00216-005-0093-7>
- [9] S. Chhillar, R. Acharya, S. Sodaye, and P. Pujari, Anal. Chem. **86**(22), 11167 (2014), <https://dx.doi.org/10.1021/ac5024292>
- [10] Y. Sunitha, and S. Kumar, Appl. Radiat. Isot. **128**, 28 (2017), <https://doi.org/10.1016/j.apradiso.2017.06.037>
- [11] V. Levenets, O. Omelnyk, A. Shchur, and B. Shirokov, J. Radioanal. Nucl. Chem. **329**, 1183 (2021), <https://doi.org/10.1007/s10967-021-07873-y>
- [12] Z. Varga, M. Krachler, A. Nicholl, M. Ernstberger, T. Wiss, M. Wallenius, and K. Mayer, J. Anal. At. Spectrom. **33**, 1076 (2018), <https://doi.org/10.1039/C8JA00006A>
- [13] V. Bondarenko, L. Glazunov, A. Goncharov, V. Kolot, V. Kuz'menko, V. Levenets, A. Omel'nik, V. Suhostavec, and V. Shchur, Scientific Bulletin (Belgorod State University), **2**(15), 86 (2001).
- [14] V. Levenets, A. Shchur, O. Omelnyk, B. Shirokov, Functional Materials. **14**(2), 258 (2007), <http://functmaterials.org.ua/contents/14-2/fm142-08.pdf>
- [15] J. Bird, M. Scott, L. Russell, and M. Kenny, Aust. J. Phys. **31**, 209 (1978), <https://doi.org/10.1071/PH780209>
- [16] I. Golicheff, M. Loeuillet, and Ch. Engelmann, J. Radioanal. Chem. **12**, 233 (1972), <https://doi.org/10.1007/BF02520991>

ВИМІРЮВАННЯ ІЗОТОПНОГО СПІВВІДНОШЕННЯ БОРУ ($\delta^{11}B$) У КАРБІДІ БОРУ (B_4C):

ПОРІВНЯННЯ МЕТОДІВ SF-ICP-MS ТА PIGE

Д.В. Кутній, С.О. Ванжа, Д.Д. Бурдейний, В.В. Левенець, О.П. Омельник, А.О. Щур

Національний науковий центр «Харківський фізико-технічний інститут» НАН України

У роботі представлені результати порівняння аналітичних можливостей методів магнітосекторної мас-спектрометрії з індуктивно-зв'язаною плазмою (SF-ICP-MS) та спектрометрії гамма-випромінювання із ядерних реакцій, що індуковані важкими частинками (PIGE) при визначенні ізотопного відношення $^{11}B/^{10}B$ в карбіді бору (B_4C). Розглянуто такі ядерні реакції, що збуджуються протонами на стабільних ізотопах бору: $^{10}B(p,\alpha\gamma)^7Be$, $^{10}B(p,\gamma)^7Be$ і $^{11}B(p,\gamma)^{12}C$. Визначено оптимальний діапазон енергій протонів в інтервалі від 550 до 600 кеВ, для індукування гамма-випромінювання з енергіями 429 та 4439 кеВ, які можуть бути використані для кількісної оцінки ізотопів ^{10}B і ^{11}B , відповідно. Показано, що з урахуванням невизначеності вимірювань величини ізотопних відношень $^{11}B/^{10}B$, що виміряні методами SF-ICP-MS і PIGE узгоджуються між собою, проте всі результати характеризуються систематичним відхиленням. Невизначеність вимірювань PIGE методу дещо вище порівняно з SF-ICP-MS, і варіюється від $\pm 4,1\%$ до $\pm 4,3\%$, і від $\pm 1,1\%$ до $\pm 3,5\%$, відповідно.

Ключові слова: ICP-MS, PIGE, карбід бору, ізотопне відношення, ядерне застосування, порівняння результатів

STUDY OF ELECTRICAL PROPERTIES OF NANO TiO₂ COATINGS BASED ON THE CHARACTERISTIC MATRIX THEORY AND THE BRUS MODEL[†]

Sarah A. Hijab*,  Saeed N. Turki Al-Rashid[#]

Physics Department, Education College for Pure Sciences, University of Anbar, Iraq

*Corresponding Author: sar20u3007@uoanbar.edu.iq

[#]E-mail: esp.saeedn.turkisntr2006@uoanbar.edu.iq

Received March 12, 2022; revised March 29, 2022; accepted April 18, 2022

Electrical properties of Nano TiO₂ coatings as a function of the nanoparticle size have been studied. In addition, this study explores how to calculate the quantum confinement energy of TiO₂. The results confirm the effect of particle size on electrical properties especially when the size becomes close to the exciton Bohr radius. The electrical properties are not effected when the size becomes close to 40nm. The Bohr radius of Nano TiO₂ coatings has been found to be 1.4nm. While the confinement energy was 0.43 eV. The program depends on the Characteristic Matrix Theory and The Brus Model.

Keywords: TiO₂, Nano Coatings, TheBrus model, TheCharacteristic matrix, Quantum confinement

PACS: 02.10Yn, 73.21La

The study of electrical properties of semiconductors nano coatings has a considerable interest in the field of nanotechnology [1]. The present study focuses on Nano TiO₂ because of its many modern coating applications. Titanium dioxide (TiO₂) belongs to the family of transitional metal oxides [2]. Nowadays, TiO₂ has a great attention in researches and industrial fields. TiO₂ is used as a white pigment in paints, paper and plastics [3]. TiO₂ is used in the solar energy industry and in anti-reflective coatings because of its stability and high absorption capacity, as well as for its strong mechanical properties, and because it has a high refractive index and good transmittance in the visible spectrum region [4]. Titanium dioxide is a semiconductor (N-type) [5]. TiO₂ has three important natural crystalline forms: anatase, brookite, and rutile, and the energy gap of anatase or rutile forms range between 3.0-3.05 eV. Titanium dioxide has a wide energy gap, which makes it suitable for UV or X-rays detection application [6]. The rutile phase is more common and stable than the other phases, while brookite is rare in nature. Brookite is formed when titanium dioxide films are amorphous in depositions at temperatures less than 300°C, while rutile is formed at high temperatures [7]. The nano-material of TiO₂ shows good electronic and optical properties because it is effective in the ultraviolet region and the refractive index is high, and it shows the photocatalytic behavior by generating an electron-hole pair when exposed to sunlight or ultraviolet rays [8].

The aim of this work is to study the electrical properties (dielectric constant, activation energy, concentration of charge carriers) of nano TiO₂ coatings with a change in the size of its nanoparticles within the ultraviolet spectral region (10-400 nm). Also, we present the calculation of confinement energy. The Characteristic Matrix Theory and The Brus Model were used to conduct this study.

THEORY

The Brus model

The Brus Model can be considered as one of the most important models which indicates that the energy gap of quantum dots in semiconductors depends on the nanoparticle size. It has another term which is called the Effective Mass Approximation (EMA). This model takes into account the values of the effective masses of the electrons and holes, which change from one material to another. The change in the energy gap of quantum dots (ΔE_g) is given by Brus equation [9]:

$$\Delta E_g = \frac{\hbar^2 \pi^2}{2r_{ps}^2} \left[\frac{1}{m_e^*} + \frac{1}{m_h^*} \right] - \frac{1.786 e^2}{\epsilon r_{ps}} - \frac{0.124 e^4}{h^2 \epsilon^2} \left[\frac{1}{m_e^*} + \frac{1}{m_h^*} \right]^{-1}, \quad (1)$$

where r_{ps} is the particle's radius as aspherical quantum dots. m_e^* represents the effective mass of electrons, m_h^* is the effective mass of holes, ϵ is the dielectric constant.

Since $\Delta E_g = E_g^{nano}(r_{ps}) - E_g^{bulk}$, eq (1) becomes [10]:

$$E_g^{nano}(r_{ps}) = E_g^{bulk} + \frac{\hbar^2 \pi^2}{2r_{ps}^2} \left[\frac{1}{m_e^*} + \frac{1}{m_h^*} \right] - \frac{1.786 e^2}{\epsilon r_{ps}} - \frac{0.124 e^4}{h^2 \epsilon^2} \left[\frac{1}{m_e^*} + \frac{1}{m_h^*} \right]^{-1}. \quad (2)$$

E_g^{bulk} represents the bulk energy gap and $E_g^{nano}(r_{ps})$ is the effective energy gap. We notice from the second term of Eq 2 that the energy gap inversely related to r_{ps}^2 , which means that the particle size decreases when the energy gap increases.

[†] Cite as: S.A. Hijab, and S.N. Turki Al-Rashid, East Eur. J. Phys. 2, 80 (2022), <https://doi.org/10.26565/2312-4334-2022-2-09>
© S.A. Hijab, S.N.T. Al-Rashid, 2022

The third term in Eq 2 will be ignored because the strenght of Coulombic interaction will increase. we observe that the second and third terms can be neglected due to the smallness compared to the first, then Eq 2 becomes:

$$E_g^{\text{nano}}(r_{\text{ps}}) = E_g^{\text{bulk}} + \frac{\hbar^2 \pi^2}{2r_{\text{ps}}^2} \left[\frac{1}{m_e^*} + \frac{1}{m_h^*} \right] \tag{3}$$

Moreover, we could suppose that the energy gap increases as the particle size decreases by reason of the effect of quantum confinement, which has a vital effect when r_{ps} becomes equal to or less than the normal Bohr radius α_0 of the exciton [11] with

$$\alpha_0 = \frac{4\pi\epsilon_0\epsilon_r\hbar^2}{e^2} \left[\frac{1}{m_e^*} + \frac{1}{m_h^*} \right] \tag{4}$$

Where e represents the electron charge, whereas ϵ_r and ϵ_0 are the dielectric constants for the semiconductor and the vacuum, respectively.

The Characteristic Matrix of Single Thin Films

The Characteristic Matrix combines the continous tangential components for the magnetic and electric fields, which can be written as [12]:

$$\begin{bmatrix} B \\ C \end{bmatrix} = \left\{ \prod_{r=1}^q \begin{bmatrix} \cos\delta_r & i \sin\delta_r / \eta_r \\ i \eta_r \sin\delta_r & \cos\delta_r \end{bmatrix} \right\} \begin{bmatrix} 1 \\ \eta_m \end{bmatrix} \tag{5}$$

Since, the phase thickness is: $\delta_r = 2\pi n_r d_r \cos\theta_r / \lambda$ here (B,C) are the Matrixs' elements (electric and magnetic fields). η_r is the optical permittivity and η_m is the refractive index of substrate. Figure 1 represents the system of a single thin film on substrate.

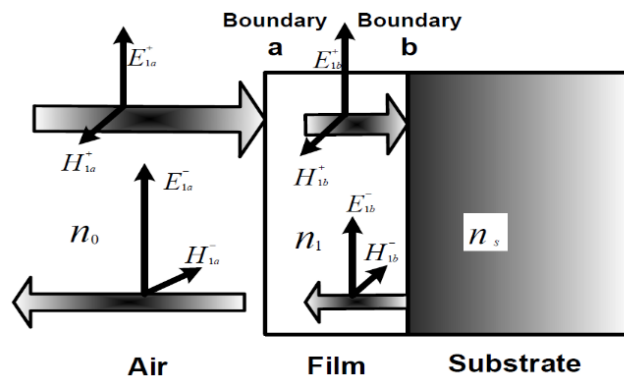


Figure 1. A plane wave incident on a thin film [13]

The equation (4) includes all the information which we need to calculate the reflectivity (R) and transmittance (T) For a single thin film deposited on the substrate's surface. And from Fresnels' equations we can find the reflectivity (R) [14]:

$$R = \left(\frac{\eta_0 - \eta_1}{\eta_0 + \eta_1} \right)^2 \tag{6}$$

η_1 and η_0 are the optical permittivity for the medium transmittance and incidence, respectively.

Quantum confinement

The quantum confinement of electrons occurs when the dimensions of the material are smaller than the distance of liberation of electrons, so it depends on the Bohr radius of the material. The quantum confinement is one of the direct effects of reducing the size of materials to nanoparticle; As the energy levels of the material become discrete, its effect appears through the change in the density of states and the energy gap of the material. Thus, the optical, electronic and electrical properties of materials become dependent on their size. Quantum dots can be defined as a physical system in which electrons are bound in three dimensions, and this electronic confinement is known as quantum confinement. Quantum confinement occurs when the dimensions of the particle structure are equal to or smaller than the de Broglie wavelength of the electron or the gap [15,16].

As an example of quantum confinement, we take a spherical semiconductor particle with a diameter ($D=2r_{\text{ps}}$), and which must be smaller than the de Broglie wavelength $\lambda = h/p$ of the electron for the particle to be a quantum dot. The typical electron kinetic energy is given by following formula [17]:

$$E = \left(\frac{2}{3}\right) k_B T = \frac{p^2}{2m_{e,h}} \quad (7)$$

And when we consider that the effective mass of the electron m_e^* is equal to its mass in free space ($9.1 \times 10^{-31} \text{kg}$) we find that $\lambda \approx 6 \text{ nm}$ at room temperature (300K), and this means that if the spherical crystal diameter is less than 6nm, The electron wave packets or holes are compressed into a smaller space than they should normally be. So, the electron will need more energy to move [18]. The above example does not take into account that the electron mass m_e^* and the hole mass m_h^* are not actually the two masses in free space that we know, but the two effective masses.

Application

In this work, we used MATLAB program version (R2021a) to study the electrical properties (Dielectric constant, Activation energy and concentration of charge carriers) of Nano-TiO₂ Coatings on (Ge) substrates as a function of the particle size. Also, we calculated the quantum confinement energy.

Concentration of charge carriers

We studied the concentration of charge carriers by using Brus model. Figure 2 shows the change in the concentration of charge carriers of TiO₂ coatings as a function of the nanoparticle size.

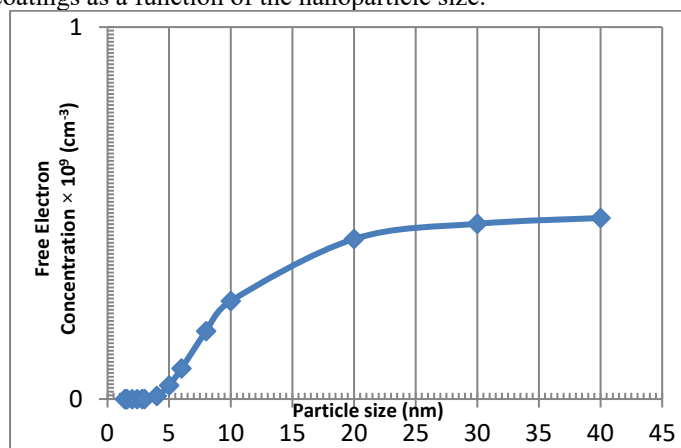


Figure 2. change in concentration of charge carriers of TiO₂ as a function of the nanoparticle size.

We noticed that when the size is very small, the concentration of charge carriers is very small. This is due to the quantum confinement of the electron, as the atoms present on the surface are few. When the nanosize increases, the concentration of charge carriers increases as expected. Indeed, when the nanosize increases, the number of molecules and atoms on the surface increases. This behavior was observed by P. Parameshwari (2012), who pointed that the increase in electrical conductivity could be associated with the decrease in the scattering at the grain boundaries when the size of the grains increases, conducting to an increase in injection and mobility of free charge carriers [19].

From Figure 2, the Bohr radius of TiO₂ was estimated to be not less than 1.4 nm. whereas, the energy gap of TiO₂, was 5.7 eV, and by using the empirical equation to calculate the refractive index of TiO₂, we found 2.2, which is less than the refractive index of the bulk material. The quantum confinement energy was calculated to be 0.43eV.

Activation energy

The activation energy was studied by using the Brus model. Figure 3 shows the change in the value of the activation energy as a function of the nanoparticle size.

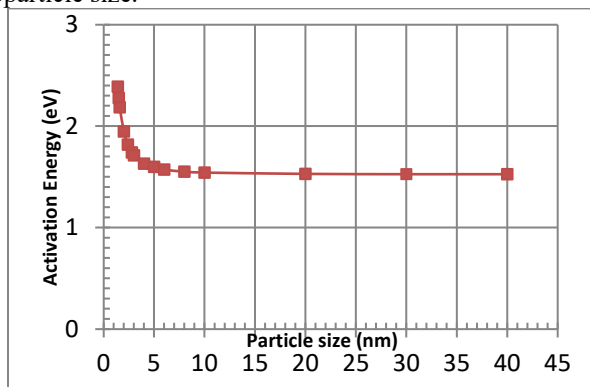


Figure 3. Change in the activation energy of TiO₂ as a function of the nanoparticle size.

From Fig. 3 we observe that at small nanoparticle sizes the values become large, but they decrease when the particle size increases close from to the exciton Bohr radius. The activation energy is at the Fermi level, which is in the middle of the energy gap. That is, the activation energy is equal to half of energy gap. This means that the change in activation energy is exactly corresponding to the change in the energy gap [20]

Generally, it was found from this study that the activation energy depends on the size of the grains and gradually decreases with the grain size. Thus, it is in agreement with previous studies [21].

Dielectric constant

At this stage, the dielectric constant was studied, using the results obtained from the Brus model to extract the dielectric constant value of TiO₂ as a function of the nanoparticle size.

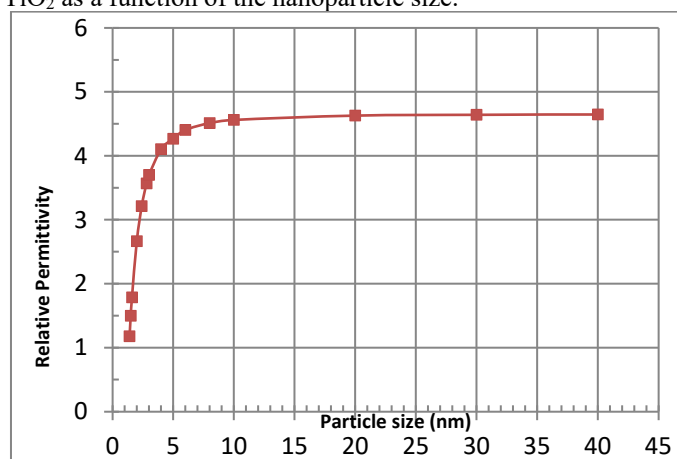


Figure 4. change in the dielectric constant of TiO₂ as a function of the change in nanoparticle size.

We observe from Fig. 4 that the dielectric constant decreases with the decrease in nanoparticle size. To clarify this in the nanoscale range, this can be understood by observing that for small particle sizes, the number of surface atoms is large, while for nanomaterials, the number of atoms per unit volume will decrease because of the quantum confinement, whereas at the nanoscale, the electron orbits causing in the increases of the Coulomb force that supports the force recovery. Thus, the natural angular frequency of electron oscillation, that results in the decreases in the dielectric constant, and this shows that the dielectric constant decreases with the size of the particle's material [22].

CONCLUSION

It has found that the dielectric constant of Nano TiO₂ coatings decreases the nanoparticle size. The values of the activation energy of Nano TiO₂ coatings are inversely related to the particle size. While the concentration of charge carriers for TiO₂ is very small when the size is too small. So no change in the electrical properties of the material can be observed, because it behaves at 40nm size as a bulk material, because the quantum confinement is almost non-existent. The quantum confinement energy was calculated to be 0.43 eV. The Bohr radius of TiO₂ was estimated to be not less than 1.4nm, and the energy gap of TiO₂ was found to be 5.7ev, and we also found the value of the refractive index of TiO₂ to be 2.2, which is less than the refractive index of the bulk material.

ORCID IDs

 Saeed N. Turki Al-Rashid, <https://orcid.org/0000-0002-7622-1526>

REFERENCES

- [1] U. Woggon, *Optical Properties of Semiconductor Quantum Dots*, (Springer-Verlag Berlin Heidelberg, Germany, 1997).
- [2] N.N. Greenwood, and A. Earnshaw, *Chemistry of the elements*, (Butterworth-Heinemann, Oxford, 1997).
- [3] A.A. Al-Khafaji, Ph.D. Thesis. *Photocatalysis of Sol-Gel Derived TiO₂ for Anti-Dust Properties*, University of Baghdad, 2013.
- [4] P. Baumeister, *Optical Coating Technology*, (SPIE Press, 2004).
- [5] A. Wisitsoraat, A. Tuantranont, E. Comini, G. Sberveglieri, and W. Wlodarski, "Characterization of n-type and p-type semiconductor gas sensors based on NiOx doped TiO₂ thin films, *Thin Solid Films*", **517**(8), 2775 (2009). <https://doi.org/10.1016/j.tsf.2008.10.090>
- [6] F. Schmidt-Stein, R. Hahn, J.F. Gnichwitz, Y.Y. Song, N.K. Shrestha, A. Hirsch, and P. Schmuki, "X-ray induced photocatalysis on TiO₂ and TiO₂ nanotubes: Degradation of organics and drug release", *Electrochem. Commun.* **11**, 2077 (2009), <http://dx.doi.org/10.1016/j.elecom.2009.08.036>
- [7] K. Karki, K.I. Gnanasekar, and B. Rambabu "Nanostructure Semiconductor Oxide Powders and Thin Films for Gas Sensors" *Appl. Sur. Sci.* **399**, 193 (2006), <https://www.electrochem.org/dl/ma/202/pdfs/0025.pdf>
- [8] C. Burda, X. Chen, R. Narayanan, and M.A. El-Sayed, "Chemistry and properties of nanocrystals of different shapes", *Chemical reviews*, **105**(4), 1025 (2005), <https://doi.org/10.1021/cr030063a>
- [9] L.E. Brus, "Electron-Electron and Electron-Hole Interactions in Small Semiconductor Crystallites: The Size Dependence of the Lowest Excited Electronic State", *Journal of Chemical Physics*, **80**(9), 4403 (1984), <https://doi.org/10.1063/1.447218>

- [10] Z.L. Wang, Y. Liu, and Z. Zhang, editors, *Handbook of nanophase and nanostructured materials, Volume II* (Kluwer Academic/Plenum Publishers, Tsinghua University Press, 2003), pp. 428.
- [11] B. Bhattacharjee, D. Ganguli, K. Iakoubovskii, A. Stesmans, and S. Chaudhuri, "Synthesis and characterization of sol-gel derived ZnS: Mn²⁺ nanocrystallites embedded in a silica matrix", *Indian Academy of Sciences*, **25**(3), 175 (2002). <https://doi.org/10.1007/BF02711150>
- [12] H.A. Macleod, *Thin-Film Optical Filters*, Fourth Edition, ISBN: 9781420073027, (CRC Press, Taylor & Francis Group, LLC, 2010), pp. 772.
- [13] N.M. Ahmed, *Design and experimental studies of Multilayer Coatings for Applications in Gallium nitride Emitting Devices*, Ph.D. Thesis, University Sa ins Malaysia, 2006)
- [14] S.M. Abed, and S.N.T. Al-Rashid, "Designing High reflectivity Omnidirectional coating of Mirrors for Near Infrared Spectrum (700-2500nm)", *Applied physics Research*, **5**(1), 102 (2013), <https://doi.org/10.5539/apr.v5n1p102>
- [15] A. Scaff, "Introduction to Nanotechnology (Science, Engineering & Applications)" Series of Strategic and Advanced Techniques, Arabic Compendium of Translation, INSB: 139789953824437, (2011).
- [16] G. Cao, and Y. Wang, *Nanostructures and Nanomaterials: Synthesis, Properties, and Applications*, ISBN: 9781783260881, (Imperial College Press, 2004), <https://doi.org/10.1142/7885>
- [17] T. Edvinsson, "Optical quantum confinement and photocatalytic properties in two-, one- and zero- dimensional nanostructures", *Royal Society Open Science*, **5**(9), 180387 (2018), <https://doi.org/10.1098/rsos.180387>
- [18] Z.L. Wang, Y. Liu, and Z. Zhang, editors, *Handbook of nanophase and nanostructured materials, Volume II*, ISBN: 9780306472497 (Kluwer Academic Plenum, 2003), pp. 406.
- [19] P. Parameshwari, B. Shashidhara, and K. Gopalakrishna, "Structural Electrical and Optical Studies on Spray Deposited Cadmium Sulphide and Copper Indium Disulphide thin films", *Arch. of Physics Research*, **3**, 441 (2012). https://www.researchgate.net/publication/281333311_Structural_electrical_and_optical_studies_on_spray_deposited_cadmium_sulphide_and_copper_indium_disulphide_thin_film
- [20] R. Zallen, *The physics of amorphous solids*, (Wiley, New York, 1983), pp. 297.
- [21] S.X. Xue, S.H. Liu, W. Zhang, J. Wang, L. Tang, B. Shen, and J.W. Zhai, "Dielectric properties and charge-discharge behaviors in niobate glass ceramics for energy-storage applications," *J. Alloys Compd.* **617**, 418 (2014) <https://doi.org/10.1016/j.jallcom.2016.06.024>
- [22] G.R. Patel, and T.C. Pandya, "Effect of size and shape on static Refractive Index, Dielectric constant and Band gap of Nano solids", *Physics and Applied Sciences*, **6**(1), 37-42 (2018), <https://doi.org/10.26438/ijsrpas/v6i1.3742>

ДОСЛІДЖЕННЯ ЕЛЕКТРИЧНИХ ВЛАСТИВОСТЕЙ ПОКРИТТІВ NANO TiO₂ НА ОСНОВІ ХАРАКТЕРИСТИЧНОЇ МАТРИЧНОЇ ТЕОРІЇ І МОДЕЛІ БРЮСА

Сара А. Хіджаб, Саїд Н.Т. аль-Рашид

Фізичний факультет Освітнього коледжу чистих наук Університету Анбара, Ірак

Досліджено електричні властивості нанопокриттів TiO₂ у залежності від розміру наночастинок. Крім того, у дослідженні вивчається, як розрахувати енергію квантового утримання TiO₂. Результати підтверджують вплив розміру частинок на електричні властивості, особливо коли розмір стає близьким до радіусу екситона Бора. Електричні властивості не змінюються, коли розмір стає близьким до 40 нм. Встановлено, що радіус Бора покриттів Nano TiO₂ становить 1,4 нм, тоді як енергія утримання становила 0,43 еВ. Програма залежить від характеристичної матричної теорії та моделі Брюса.

Ключові слова: TiO₂, нанопокриття, модель TheBrus, TheCharacteristic matrix, Quantum confinement

INVESTIGATION OF A GLOW DISCHARGE WITH A COAXIAL HOLLOW CATHODE[†]

 Stanislav V. Pogorelov^a,  Volodymyr A. Timaniuk^{a,*},  Ihor V. Krasovskyi^a,
 Nikolay G. Kokodii^b

^aNational University of Pharmacy, Kharkiv, Ukraine

^bV.N. Karazin Kharkiv National University, Kharkiv, Ukraine

*Corresponding Author: vladimir.timaniuk@gmail.com, tel.: +38 095 505 39 19

Received February 11, 2022; revised March 26, 2022; accepted April 4, 2022

The article is devoted to the study of the operating modes of a glow discharge with a coaxial hollow cathode in helium and neon gases. It is shown that the burning voltage of a discharge with a coaxial hollow cathode is lower than one with a cylindrical hollow cathode of equal diameter, and the position of the optimal pressure range depends on the width of the annular gap of the cavity. It is noted that the rod current density is 3-5 times higher than the cylinder current density. The insignificant role of the photoelectric effect in the processes of electron emission from the cathode is proved. It is shown that the intensity of the atomic spectral lines of the cathode material increases significantly when a coaxial hollow cathode is used.

Keywords: glow discharge, hollow cathode, cathode configuration, spectral sources, electron oscillations, discharge current density.

PACS: 52.80.Pi; 52.80.Tn

The vast majority of glow discharge studies in hollow cathode devices use cylindrical hollow cathodes that are open at one or both ends. However, the effect of a hollow cathode is also observed with other configuration of the cathode cavity (a double hollow cathode formed by two flat plates located at a rather small distance; or hollow cathodes with different shapes of the inner cavity [1]), as long as conditions for the oscillation of fast electrons in the cross section of the cathode cavity are provided. These designs have no advantages over the cylindrical hollow cathode and therefore have not gained widespread acceptance. An exception is the slit hollow cathode used in ion lasers, which is essentially a cylindrical hollow cathode, with withdrawal of a current through a slit in the side surface of the cylinder.

GOALS OF ARTICLE

Analyzing the features of the discharge mechanism with a cylindrical hollow cathode, the following drawback of these cathodes can be noted [2, 3, 4]. On the axis of the cathode cavity, there is a maximum concentration of slow electrons, which have an energy of less than 1 eV near the upper boundary of the optimal pressures range. Consequently, in the axial region of the cylindrical cathode cavity, conditions for intense volume recombination of electrons and ions are created, because of this recombination the degree of plasma ionization in the cathode cavity decreases. Placement of additional electrodes in the cathode cavity, for example, an anode or an insulated electrode [3] leads to the loss of fast electrons due to violation of the conditions for the oscillation of fast electrons and a sharp increase in the burning voltage of the discharge. However, placing a metal rod, connected to the cathode, on the axis of the cathode cavity leads to a decrease in the burning voltage of the discharge in comparison with a hollow cathode formed by the same cylinder without a rod. Therefore, such a hollow cathode, called coaxial, was investigated in more detail.

MATERIALS AND METHODS

One of the designs of discharge tubes with a coaxial hollow cathode is shown in Figure 1.

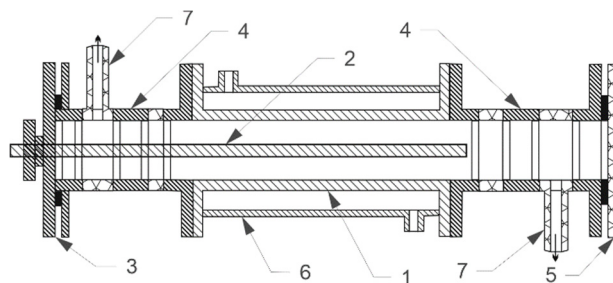


Figure 1. Construction of the discharge tube with a coaxial hollow cathode: 1 - cylinder; 2 - removable rod; 3 - side flange; 4 - anodes; 5 - glass plate; 6 - water cooling jacket; 7 - glass pipes for gas.

The cathode cavity is formed by a cylinder 1 and a removable rod of various diameters 2, fixed with a vitrified holder in the side flange 3. The anodes are two annular electrodes 4 located coaxially with the cathode cavity. The second side flange is covered with a glass plate 5 for visual observation and output of optical radiation from the cathode cavity. The outer

[†] Cite as: S.V. Pogorelov, V.A. Timaniuk, I.V. Krasovskyi, and N.G. Kokodii, East Eur. J. Phys. 2, 85 (2022), <https://doi.org/10.26565/2312-4334-2022-2-10>
© S.V. Pogorelov, V.A. Timaniuk, I.V. Krasovskyi, N.G. Kokodii, 2022

cylinder is equipped with a water cooling jacket 6, filling the tube with gas and pumping out was performed through glass pipes 7. The rod could be introduced into the cathode cavity using a bellows system that allows the rod to be shifted parallel to the axis of the cathode cavity. All measurements were carried out in the continuous flow regime of spectrally pure helium and neon gases.

RESULTS

For a cylindrical hollow cathode, the discharge burning voltage depends on the geometric dimensions of the cathode cavity and the cathode material. Figure 2 shows the dependences of the burning voltage on the helium pressure for a coaxial hollow cathode with a rod diameter of 2 mm and 5 mm at a discharge current of 10 mA. Similar measurements were also carried out for the cylindrical hollow cathode.

It can be seen that, in the region of optimal pressures, the burning voltage in the coaxial hollow cathode is lower than in the cylindrical one, and a shift of both boundaries of the region of optimal pressures is observed. With an increase in the diameter of the rod, the transverse size of the resulting annular cavity, along which the electron oscillations occur, decreases. And just like for a cylindrical hollow cathode, with a decrease in the diameter, the burning voltage decreases and the boundaries of the region of optimal pressures shift towards higher pressures.

Figure 3 shows the dependence of the burning voltage on the helium pressure for a cylindrical hollow cathode and coaxial hollow cathode formed by an aluminum cylinder with a diameter of 30 mm and a rod with a diameter of 5 mm made of molybdenum, aluminum and nickel.

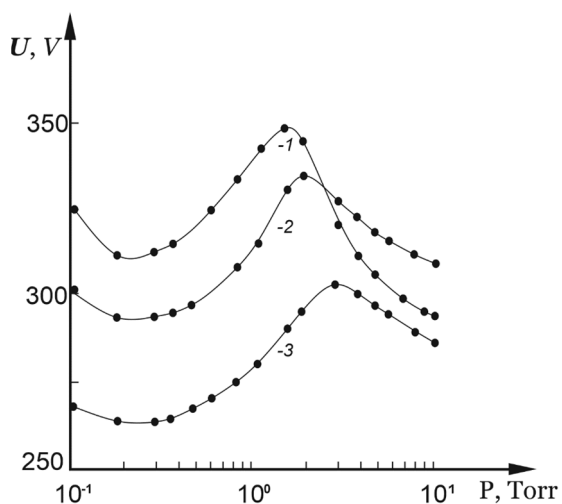


Figure 2. The dependences of the burning voltage on the helium pressure for a cylindrical hollow cathode (CylHC) with a cylinder diameter of 30 mm (1) and for a coaxial hollow cathode (CoaxHC) with a rod diameter of 2 mm (2) and 5 mm (3)

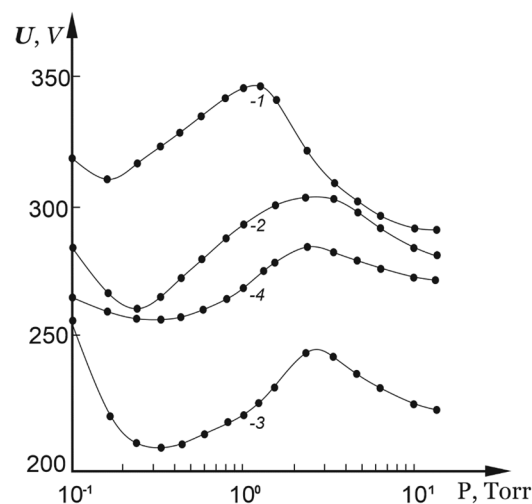


Figure 3. The dependence of the burning voltage on the helium pressure for CylHC with a cylinder diameter of 30 mm (1) and CoaxHC with a rod diameter of 5 mm of molybdenum (2), aluminum (3) and nickel (4)

Curve 1 corresponds to a hollow cathode without a rod. It can be seen that the burning voltage of the discharge depends on the material of the rod and also it depends on the material of a cylindrical hollow cathode. If both the outer cylinder and the rod are made of nickel (Figure 4), then the burning voltage at the minimum of the $U(P)$ dependence is 116 V, which is less than the normal cathode potential drop for a nickel-helium pair (144V) [5].

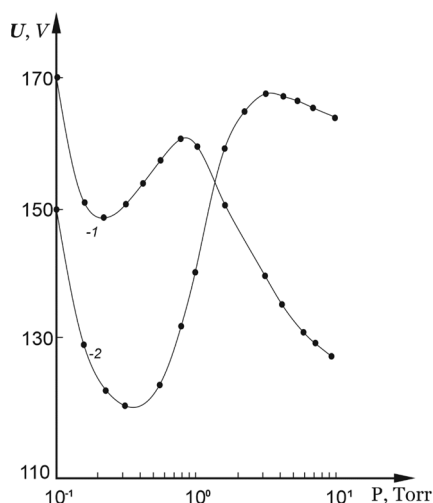


Figure 4. The dependence of the burning voltage on the neon (1) and helium (2) pressure for CoaxHC with a nickel cylinder diameter of 30 mm and a nickel rod diameter of 10 mm at the discharge current of 100 mA

The fact that the burning voltage in the coaxial hollow cathode depends on the rod material indicates that the atomized atoms of the outer cylinder fall on the rod in an insignificant amount. The displacement of the boundaries of the optimal pressures region depending on the type of gas for a coaxial hollow cathode has the same regularities as for a cylindrical one. One would expect that if the width of the annular gap of the coaxial hollow cathode is equal to the diameter of the cylindrical hollow cathode, the regions of optimal pressures should coincide. Comparison for helium gas of the upper PU and lower PL boundaries of the optimal pressures region for a coaxial hollow cathode (CoaxHC) and cylindrical (CylHC) with the equality of the gap width and the diameter of the cathode cavity is given in Table.

Table. The value of the upper P_U and lower P_L boundaries of the optimal pressures region at the same values of the width of the gap of the CoaxHC and the diameter of the CylHC.

	6.5 mm		10 mm		12.5 mm		14 mm	
	CoaxHC	CylHC	CoaxHC	CylHC	CoaxHC	CylHC	CoaxHC	CylHC
P_U , Torr	5.0	7.5	3.0	4.5	3.0	4.0	2.0	3.5
P_L , Torr	0.6	1.5	0.4	0.9	0.4	0.75	0.3	0.7
P_U/P_L	8.3	5.0	7.5	5.0	7.5	5.0	6.7	5.0

DISCUSSIONS

It can be seen from the table that in all cases the region of optimal pressures of the coaxial hollow cathode is shifted relative to the cylindrical one towards lower pressures. At the same time, the value of P_U/P_L for a coaxial hollow cathode is higher than for a cylindrical one. All this indicates that the oscillations of fast electrons in the coaxial hollow cathode occur not only in the radial direction. Part of the electrons emerging from the outer cylinder is decelerated in the dark cathode space near the rod, and part of the electrons first bends around this region and then falls into the dark cathode space near the cylinder again. Thus, the length of the trajectory for different electrons lies in the range from S - the width of the annular gap to D - the diameter of the outer cylinder. As a result, the width of the optimal pressure region increases. The above considerations are confirmed by the fact that when the rod is displaced relative to the axis of the outer cylinder, the region of optimal pressures also expands.

The problem of studying the distribution of the current in a coaxial hollow cathode has two aspects. First, the distribution of the current between the outer cylinder and the rod, and second, the distribution of the current along the length of the cathode cavity [6]. In all discharge tubes, the rod had an insulated terminal, and this made it possible to measure the rod current and its dependence on various conditions. A tube with a sectioned hollow cathode was used to measure the longitudinal distribution of the current.

It turned out that the current to the rod makes up a significant part of the total cathode current and is practically independent of the gas pressure in the region of optimal pressures. Figure 5 shows the dependence of the current on the helium gas pressure for a coaxial nickel cathode with an outer cylinder 30 mm in diameter and different rod diameters: 1 mm, 2.5 mm, 5 mm and 10 mm and the same discharge current of 100 mA.

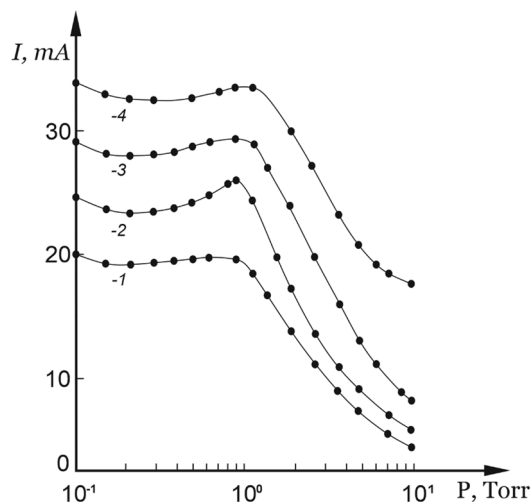


Figure 5. The dependence of the current to the rod on the helium pressure for a nickel CoaxHC with a cylinder diameter of 30 mm and rod diameters of 1 mm (1), 2.5 mm (2), 5 mm (3) and 10 mm (4) at the discharge current of 100 mA

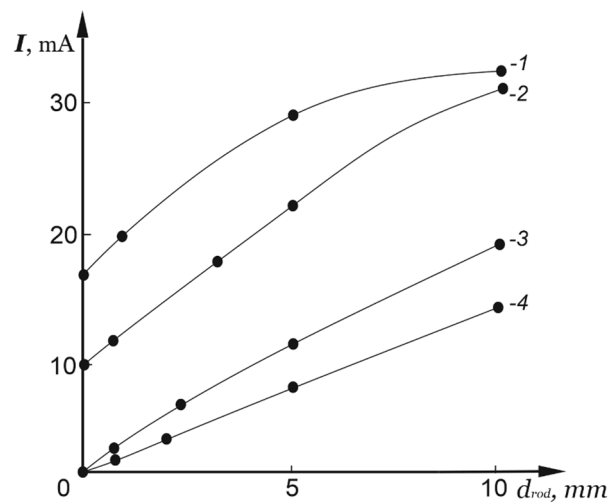


Figure 6. The dependence of the current to the rod on its diameter at helium pressure of 1 Torr (1), 2 Torr (2), 5 Torr (3), 10 Torr (4) at the discharge current of 100 mA. Cylinder diameter equals 30 mm

With an increase in the diameter of the rod, the transition point from a flat section to a steeply dipping one shifts towards high pressures. With the smallest diameter of the rod (1 mm), the rod current in the pressure range of 0.1-1 Torr is about 20% of the total discharge current, although the surface of the rod in this case is 30 times smaller than the surface of the cylinder. Figure 6 shows the dependence of the rod current on its diameter at various helium pressures.

Curve 1 corresponds to the pressure range from 0.1 to 1 Torr. At these pressures, an increase in the diameter of the rod by a factor of 10 leads to an insignificant increase in its current (from 20 mA to 32 mA). With increasing pressure, the dependence of the rod current on the diameter increases, and at a pressure of 10 Torr, the rod current is proportional to its diameter. Such a nature of the curves may indicate a change in the mechanism of emission from the cathode in the studied pressure range.

When the rod is displaced parallel to the axis of the cathode cavity, the pattern of the dependence of the current to the rod on the gas pressure changes. Figure 7 shows the dependence of the current to the rod on the helium pressure for the rod located on the axis of the cavity (curve 1) and when the rod is displaced from the axis by 5 mm (2) and 10 mm (3).

When the rod is displaced perpendicular to the axis, a clear maximum appears on the curves, which, with an increase in the displacement of the rod, shifts to the region of higher pressures. At low gas pressures, the rod current decreases, at high gas pressures, it increases. This behavior of the curves indicates that the current to the rod is determined by the plasma concentration in the cavity of the cylindrical hollow cathode at the location of the rod.

Figure 8 shows the dependences of the current density to the rod on the helium pressure for rods of different diameters, as well as the dependences of the current density to the cylinder.

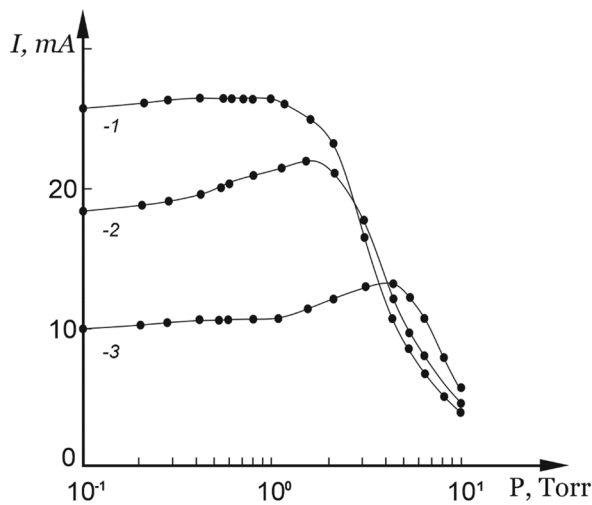


Figure 7. The dependence of the current to the rod on the helium pressure for the rod located on the axis (1) and the rod displaced from the axis by $\Delta_r = 5\text{mm}$ (2) and $\Delta_r = 10\text{mm}$ (3) at the discharge current of 100 mA. Cylinder diameter equals 30 mm. Rod diameter equals 2 mm

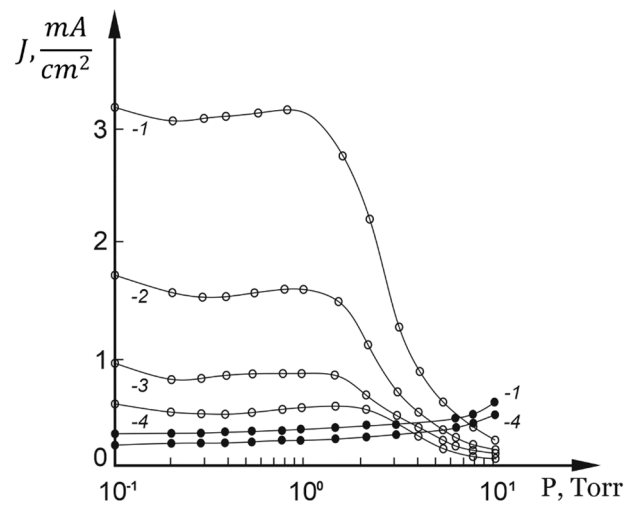


Figure 8. The dependences of the current density to the rod (-o-) and to the cylinder (-●-) on the helium pressure with a cylinder diameter of 30 mm and rod diameters of 1 mm (1), 2.5 mm (2), 5 mm (3) and 10 mm (4) at the discharge current of 100 mA

The current density to the rod increases sharply with decreasing rod diameter, while the current density to the cylinder remains almost unchanged. With an increase in the gas pressure, the current density to the rod decreases and at a pressure above 5 Torr it becomes less than the current density to the cylinder.

The current distribution along the cylinder of a coaxial hollow cathode was studied using a tube with a sectioned hollow cathode 15 mm in diameter, on the axis of which a rod 1 mm and 2 mm in diameter was located. The pattern of the dependence of the current along the length of the coaxial hollow cathode turned out to be qualitatively the same as for the cylindrical hollow cathode. When the rod is placed on the axis of the cylinder, the transverse dimension of the cathode cavity decreases, which prevents the penetration of plasma into the depth of the cathode. Therefore, in order to provide a relatively uniform current load of the cylinder in the coaxial hollow cathode, its length in comparison with the cylindrical one must be reduced in proportion to the decrease in the transverse size of the cathode cavity [7].

Taking into account the fact that in a coaxial hollow cathode the rod current density can be much higher than the cylinder one, it can be assumed that the rod material will be sputtered more intensively than the cylinder material, and the lines of the rod material will prevail in the spectrum of the discharge glow. These considerations stimulated spectral studies of the radiation from a discharge with a coaxial hollow cathode. Copper and iron were used as the rod materials. Measurements were carried out with a discharge in helium and neon. The emission spectrum was recorded using an ISP-51 spectrograph.

The region of negative glow in a discharge with a coaxial hollow cathode has the shape of a ring and changes in the same way as in a discharge with a cylindrical hollow cathode. A dark cathode space exists near the surface of the cylinder and near the surface of the rod. With increasing gas pressure, the width of the dark cathode space decreases, and at pressures less than 2 Torr, the negative glow is distributed into two parts: brighter and wider is near the cylinder, less bright and narrow is near the rod. Photographing the discharge glow with subsequent photometry of the film on the MF-2 microphotometer made it possible to measure the width of the dark cathode space in the discharge (d_c). The value of d_c near the surface of the rod turns out to be constant up to a pressure of 1 Torr, moreover, d_c near the rod is almost 2

times less than near the cylinder. This is due to the fact that the cathode potential drop at the rod and at the cylinder is the same, but the rod current density in this case is 3.4 times higher than the cylinder one. As expected, due to the fact that the current density to the rod is higher than to the cylinder, in the emission spectrum of the coaxial hollow cathode, mainly the lines of the rod material are observed.

When the rod is connected, additional lines appear in the spectrum, the identification of which showed that these are analytical lines of iron at 404.5 nm, 427.1 nm, and 438.3 nm. [8]. Thus, at a discharge current of 50 mA, the sputtering of the cylinder is still insufficient for the lines of the metal from which it is made to appear in the spectrum. When the rod is connected, despite the fact that the current to it is only 14% of the total discharge current, rather intense metal lines appear in the discharge spectrum [9]. Figure 9 shows the dependence of the intensity of three sensitive lines of iron on the discharge current at the neon gas pressure of 1 Torr.

Curves 1 — 3 were obtained for a coaxial hollow cathode; 1'— 3' for a cylindrical hollow cathode with a diameter equal to the diameter of the cylinder of the coaxial hollow cathode. It can be seen that in the coaxial hollow cathode, iron lines are reliably recorded at a discharge current of 20 mA, in a cylindrical one, a current of more than 60 mA is required. Thus, a coaxial hollow cathode is approximately 3 times more efficient than a cylindrical one for use as a source of the iron spectrum. The dependence of the intensity of the spectral lines of copper on the neon pressure for a coaxial hollow cathode is shown in Figure 10.

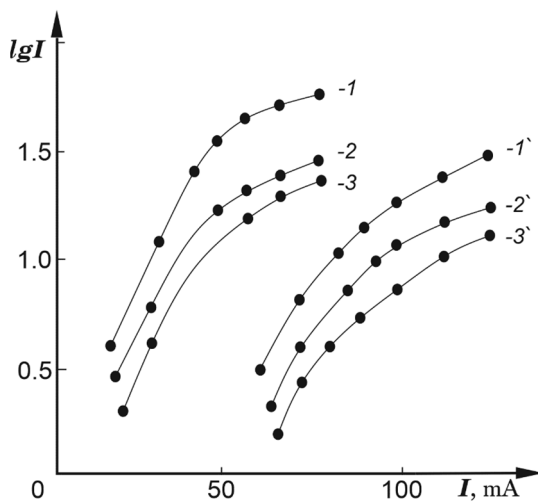


Figure 9. The dependence of the intensity of three sensitive lines of iron $\lambda=438.3$ nm (1), $\lambda=427.2$ nm (2) and $\lambda=404.6$ nm (3) on the discharge current at the neon gas pressure of 1 Torr. 1 - 3 are for CoaxHC, and 1' — 3' are for CylHC

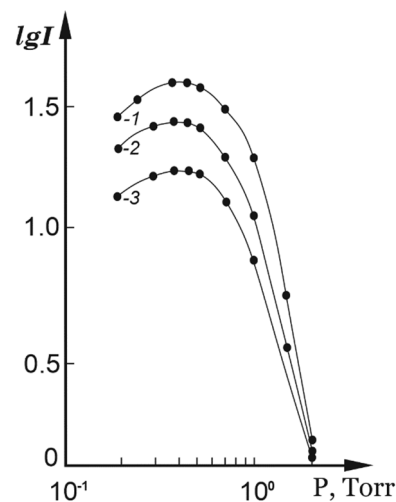


Figure 10. The dependence of the intensity of the spectral lines of copper $\lambda=511.8$ nm (1), $\lambda=515.3$ nm (2) and $\lambda=510.5$ nm (3) on the neon pressure for CoaxHC at the discharge current of 20 mA

In the range of neon pressures of 0.2 - 0.8 Torr, the intensity of the spectral lines of the rod material changes little, and at higher pressures, the intensity decreases sharply. This behavior of the curves is due to the action of several factors. At low gas pressures, the supply of sputtered atoms to the glow region increases, but the concentration of electrons in the plasma decreases, and as a result, the dependence of the radiation intensity on the gas pressure is weakened. As the pressure rises above 1 Torr, the number of sputtered atoms, the plasma concentration, and the current density to the rod decrease. This leads to a sharp decrease in the radiation intensity of the spectral lines of the rod material. Similar measurements were carried out for a discharge with a coaxial hollow cathode in helium. Due to the low mass of the ion, the sputtering of atoms of the cathode material and the intensity of the corresponding spectral lines in helium are lower than in neon.

CONCLUSIONS

As a result of studying the main electrical and spectral characteristics of a discharge with a coaxial hollow cathode made of various materials for different diameters of the outer cylinder and rod, the following new results were obtained.

1. In the annular cavity formed by electrically connected coaxial electrodes, the "hollow cathode effect" is preserved. The burning voltage of a discharge with a coaxial hollow cathode in the region of optimal pressures is lower than that of a discharge with a cylindrical cathode of the same diameter.

2. The position of the region of optimal pressures of the coaxial hollow cathode depends on the width of the annular gap of the cavity and the type of gas. The width of the region of optimal pressures of a coaxial hollow cathode is wider than that of a cylindrical one with an equal transverse size of the cathode cavity. The dependence of the discharge burning voltage on the gas pressure in a coaxial hollow cathode is weaker than in a cylindrical one.

3. The rod current density is 3-5 times higher than the cylinder current density and at low pressures is practically independent of the pressure and the gas type.

4. The weak dependence of the current to the rod on its diameter indicates an insignificant role of the photoelectric effect in the processes of electron emission from the cathode.
5. Due to the higher current density to the rod, the width of the dark cathode space near the rod surface is approximately 2 times less than that near the cylinder surface.
6. In the spectrum of a discharge with a coaxial hollow cathode, the intensity of the lines of the rod material sputtered atoms is much higher than that of the atoms of the cylinder material.

ORCID IDs

 Stanislav V. Pogorelov, <https://orcid.org/0000-0002-0189-8655>;  Volodymyr A. Timaniuk, <https://orcid.org/0000-0003-0689-6074>
 Ihor V. Krasovskyi, <https://orcid.org/0000-0003-4585-7377>;  Nikolay G. Kokodii, <https://orcid.org/0000-0003-1325-4563>

REFERENCES

- [1] A.S. Klimov, Yu.A. Burachevsky and I.S. Zhirkov, Proceedings of TUSUR University, **18**(2), 53 (2008), <https://journal.tusur.ru/storage/47466/53-58.pdf?1467799502>. (in Russian)
- [2] B.I. Moskalev, *Разряд с полым катодом [Hollow cathode discharge]*, (Energiya, Moscow, 1969), pp. 184. (in Russian)
- [3] V.A. Timanyuk, N.G. Kokodiy, and F.G. Diaghileva, Papers SWORLD Transport, Engineering, Physics and Mathematics, **2**(46), 95 (2017), <https://www.sworld.com.ua/ntsw/117-2.pdf>. (in Russian)
- [4] V. Lisovskiy, and I. Bogodielnyi, East European Journal of Physics, **1025**(4), 43 (2012), <https://periodicals.karazin.ua/ejrp/article/view/13588>
- [5] P.N. Chistyakov, in: *Физическая электроника: сборник статей [Physical electronics: collection of articles]*, (Atomizdat, Moscow, 1966), pp. 3-19. (in Russian)
- [6] Bánó, G., Szalai, L., Kutasi, K. et al. Operation characteristics of the Au-II 690-nm laser transition in a segmented hollow-cathode discharge. Appl Phys B, **70**, 521 (2000), <https://doi.org/10.1007/s003400050855>.
- [7] S.V. Pogorelov, V.A. Timaniuk, N.G. Kokodii, and I.V. Krasovskyi, East European Journal of Physics, **(2)**, 155 (2021), <https://doi.org/10.26565/2312-4334-2021-2-13>.
- [8] A.N. Zaidel et al, *Таблицы спектральных линий [Spectral Lines Tables]*, (Nauka, Moscow, 1977), pp. 798. (in Russian)
- [9] V.H. Baggio-Scheid, J.W. Neri, and G. de Vasconcelos, Surface and Coatings Technology, **146-147**, 469-473 (2001), [https://doi.org/10.1016/S0257-8972\(01\)01458-X](https://doi.org/10.1016/S0257-8972(01)01458-X).

ДОСЛІДЖЕННЯ ТЛЮЧОГО РОЗРЯДУ З КОАКСІАЛЬНИМ ПОРОЖНИСТИМ КАТОДОМ

Станіслав В. Погорелов^a, Володимир О. Тіманюк^a, Ігор В. Красовський^a, Микола Г. Кокодій^b

^aНаціональний фармацевтичний університет, Харків, Україна

^bХарківський національний університет імені В. Н. Каразіна, Харків, Україна

Стаття присвячена дослідженню режимів роботи тліючого розряду з коаксіальним порожнистим катодом у газах гелію та неону. Показано, що напруга горіння розряду з коаксіальним порожнистим катодом нижча, ніж з циліндричним порожнистим катодом однакового діаметра, а положення оптимального діапазону тиску залежить від ширини кільцевого зазору порожнини. Зазначено, що щільність струму штока в 3-5 разів перевищує щільність струму циліндра. Доведено незначну роль фотоелектру в процесах емісії електронів з катода. Показано, що при використанні коаксіального порожнистого катода інтенсивність атомних спектральних ліній матеріалу катода значно зростає.

Ключові слова: тліючий розряд, порожнистий катод, конфігурація катода, спектральні джерела, електронні коливання, щільність струму розряду.

EFFECTS OF DIFFERENT FACTORS ON THE HEAT CONDUCTION PROPERTIES OF CARBON FILMS AND FIBERS[†]

 **Junjie Chen**

*Department of Energy and Power Engineering, School of Mechanical and Power Engineering, Henan Polytechnic University
2000 Century Avenue, Jiaozuo, Henan, 454000, P.R. China*

Corresponding author: cjjtpj@163.com

Received February 3, 2022; accepted April 18, 2022

The increasing popularity of carbon nanotubes has created a demand for greater scientific understanding of the characteristics of thermal transport in nanostructured materials. However, the effects of impurities, misalignments, and structure factors on the thermal conductivity of carbon nanotube films and fibers are still poorly understood. Carbon nanotube films and fibers were produced, and the parallel thermal conductance technique was employed to determine the thermal conductivity. The effects of carbon nanotube structure, purity, and alignment on the thermal conductivity of carbon films and fibers were investigated to understand the characteristics of thermal transport in the nanostructured material. The importance of bulk density and cross-sectional area was determined experimentally. The results indicated that the prepared carbon nanotube films and fibers are very efficient at conducting heat. The structure, purity, and alignment of carbon nanotubes play a fundamentally important role in determining the heat conduction properties of carbon films and fibers. Single-walled carbon nanotube films and fibers generally have high thermal conductivity. The presence of non-carbonaceous impurities degrades the thermal performance due to the low degree of bundle contact. The thermal conductivity may present power law dependence with temperature. The specific thermal conductivity decreases with increasing bulk density. At room temperature, a maximum specific thermal conductivity is obtained but Umklapp scattering occurs. The specific thermal conductivity of carbon nanotube fibers is significantly higher than that of carbon nanotube films due to the increased degree of bundle alignment.

Keywords: carbon nanotubes; thermal properties; carbon fibers; thermal conductivity; nanostructured materials; Umklapp scattering

PACS: 65.40.-b, 65.80.-g, 68.37.-d, 68.55.-a, 68.60.-p

Carbon nanotubes can exhibit unique ability to conduct heat [1, 2], referred to as heat conduction properties. Specifically, carbon nanotubes are a highly effective thermal conductor in the longitudinal direction. However, a thermal barrier is formed in the radial direction. For an individual single-walled carbon nanotube, the thermal conductivity in the radial direction is around 1.52 W/(m·K) at room temperature [3]. In contrast, carbon nanotubes show superior heat conduction properties along the longitude directions. The thermal conductivity in the longitudinal direction is around 3500 W/(m·K) at room temperature [4]. Consequently, carbon nanotubes outperform diamond as the best thermal conductor. When macroscopic, ordered assemblies of single-walled carbon nanotubes are formed, the thermal conductivity of carbon nanotube films and fibers could reach up to around 1500 W/(m·K) at room temperature [5]. The heat conduction properties of carbon nanotube networks vary significantly, with a minimum of thermal conductivity less than 0.1 W/(m·K) [6]. The heat conduction properties depend on a variety of factors such as impurities and misalignments. Single-walled carbon nanotube are stable up to around 1000 K in air and around 3000 K in vacuum [7]. The study of heat transport phenomena involved in carbon nanotubes is an active area of interest [8] due to the potential for applications in thermal management.

The thermal conductivity of carbon nanotubes depends heavily upon crystallographic defects. Phonons can scatter due to crystallographic defects. This will lead to the increased relaxation rate, thereby decreasing thermal conductivity associated with the reduced mean free path of phonons [9, 10]. In single-walled carbon nanotubes, the mean free path varies from 50 nm to 1500 nm [11, 12]. Crystallographic defects will lead to a significant reduction in mean free path [13], for example, 4 nm or less [14]. The thermal conductivity of carbon nanotubes depends also upon the structure of the nanotubes. The thermal conductance of multi-walled carbon nanotubes is significantly higher than the sum of that of each individual shell due to the inter-wall interactions [15]. The thermal conductivity of a multi-walled carbon nanotube is lower than that of a single-walled carbon nanotube with an identical diameter configuration [16] due to an increase in cross-sectional area.

Bulk carbon nanotubes can be used as composite fibers in polymers, but the bulk structure will reduce the ability to conduct heat, causing a decrease in thermal conductivity. The thermal conductivity of carbon nanotube fibers is comparable to that of common metals [17]. Through chemical modification, however, the ability to conduct heat is comparable to or higher than that of highly conductive metals [18], for example, copper. The thermal conductivity varies significantly depending upon the density and cross-sectional area of the bulk material. The bulk carbon nanotube material contains pores [19, 20]. Consequently, the thermal conductivity of the non-compact bulk material is much lower than that of the skeletal material, since the bulk volume is inclusive of the void fraction. The skeletal portion of the bulk material is often referred to as the "matrix" or "frame". However, there is considerable uncertainty in determination of the density of the bulk material. Consequently, the effects of carbon nanotube structure, purity, and alignment on the thermal

[†] Cite as: J. Chen, East Eur. J. Phys. 2, 91 (2022), <https://doi.org/10.26565/2312-4334-2022-2-11>
© J. Chen, 2022

conductivity of carbon films and fibers are still poorly understood. Little research has been conducted to determine which parameters are important for high thermal conductivity.

This study relates to the heat conduction properties of carbon nanotube films and fibers. Carbon nanotube films and fibers were produced, and the parallel thermal conductance technique was employed to determine the thermal conductivity. The effects of carbon nanotube structure, purity, and alignment on the thermal conductivity of carbon films and fibers were investigated to understand the characteristics of thermal transport in the nanostructured material. The objective is to gain insight into the fundamental characteristics of thermal transport in carbon nanotubes. Particular emphasis is placed on the dependence of thermal conductivity on carbon nanotube structure, purity, and alignment, with an attempt to improve the heat conduction properties for carbon nanotube films and fibers.

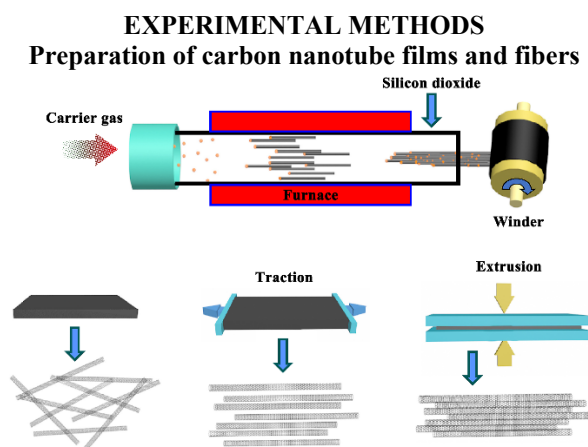


Figure 1. Schematic illustration of the preparation process of carbon nanotube films. A dense film was laid down with aligned carbon nanotube bundles.

Carbon nanotube films were produced by spinning continuously onto a single rotational winder of a spinning machine. The preparation process of carbon nanotube films is depicted schematically in Figure 1. A dense film was laid down with aligned carbon nanotube bundles. The dense film was sprayed with acetone to further condense the carbon nanotube networks. By preparing a dense film in such a manner, the carbon nanotubes were highly aligned [21], although the surface tension effect is significant in the extrusion process [22]. A laser was used to cut the carbon nanotube film into small pieces for the measurement of thermal conductivity. Carbon nanotube fibers were produced by stretching the dense film with two rotational winders of the spinning machine. The two rotational winders operate with only a small difference in rotation rate.

Thermal conductivity measurement methods

To determine the thermal conductivity, the parallel thermal conductance technique was employed [23, 24], since the diameter of the needle-like samples was very small. Fourier's Law was used to compute the thermal conductivity. This steady-state method has been carried out to measure the thermal conductivity of boron nitride nanotube sheets [25], and carbon nanotube sheets [26] and yarns [27, 28]. The configuration of the parallel thermal conductance technique is depicted schematically in Figure 2.

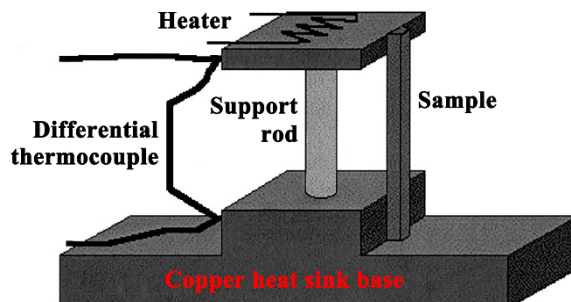


Figure 2. Schematic illustration of the configuration of the parallel thermal conductance technique. The base line was measured with the sample holder itself and then the sample was attached to perform the measurement of parallel thermal conductance in which the base line was subtracted.

A preliminary measurement of thermal conductance was performed with respect to the sample holder itself so as to determine the background or base-line heat conduction and losses associated with the sample stage. The sample was attached and the thermal conductance of the system was measured. The parallel thermal conductance can be obtained by subtraction. In this method, all conductance factors arising from the thermal contacts, sample, and thermal radiation from

the sample accounted for. The radiative heat losses were caused primarily by the thermal radiation from the hot surface of the heater. However, such heat losses were already included in the base line. Therefore, a correction factor of 0.5 was introduced into the method [23, 24] to account for the radiative heat losses.

Linear mass density measurement methods

The linear mass density of the carbon nanotube films was measured by using a gravimetric method [29]. In contrast, the linear mass density of the carbon nanotube fibers was measured by using a vibroscope method [29, 30]. The sample was tensioned between two hard points of a mechanical vibroscope. Mechanical vibration was induced and the fundamental frequency was measured. The specific thermal conductivity is defined as the thermal conductivity normalized by bulk density. The bulk density can be determined in terms of the linear mass density and the cross-sectional area.

RESULTS AND DISCUSSION

Material characterization

The prepared carbon nanotube fibers are characterized by scanning electron microscopy. The surface morphology is analyzed with scanning electron microscope SU3800, Hitachi High-Tech Corporation. Scanning electron microscopy images are presented in Figure 3 for the carbon nanotube fibers prepared by the method described above. The carbon nanotubes are highly aligned. However, the fiber material contains a relatively small amount of short deformed carbon nanotubes. The carbon nanotubes are of the order of several hundred microns.

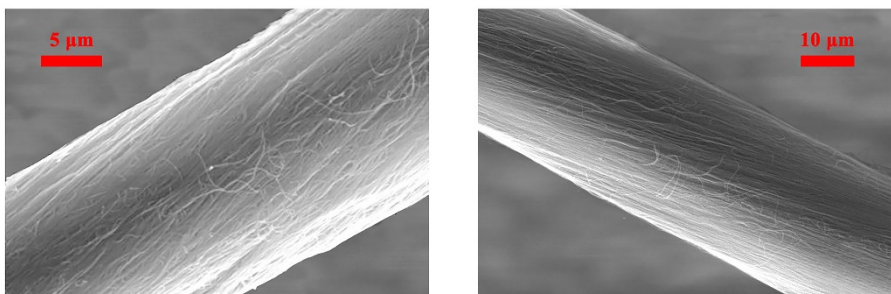


Figure 3. Scanning electron microscopy images of the carbon nanotube fibers prepared by the method described in detail above.

Four samples are prepared with different structure, purity, and alignment in order to investigate the effects of various factors on the thermal conductivity. Three structural parameters are selected in terms of alignment, purity, and the number of walls. The structural parameter space for the selection of samples is illustrated in Figure 4 in the style of the design of measurement experiments. For type A, the carbon nanotube films or fibers are composed mostly of multi-walled carbon nanotubes. In addition, there is a small amount of short deformed carbon nanotubes. For type B, a mixture of carbon nanotubes is used. More specifically, the carbon nanotube films or fibers are composed of single-walled and multi-walled carbon nanotubes. In addition, there is a small amount of amorphous carbon. For type C, the carbon nanotube films or fibers are composed mostly of single-walled carbon nanotubes. In addition, there is a small amount of non-carbonaceous impurities. For type D, the carbon nanotube films or fibers are composed of single-walled carbon nanotubes with very high purity. The understanding of which parameters are important for high thermal conductivity is made possible through the comparison of heat conduction properties between the nanostructured materials.

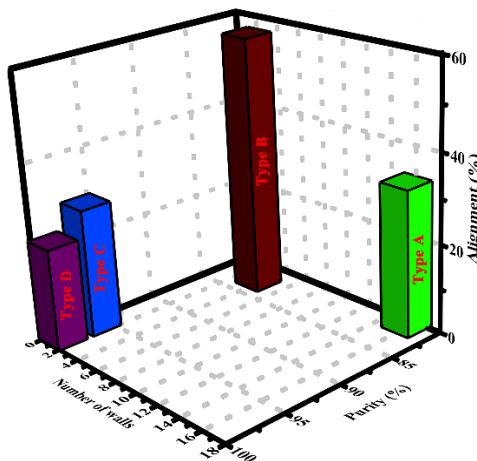


Figure 4. Structural parameter space for the selection of samples in the style of the design of measurement experiments.

Thermal conductivity of carbon nanotube films

The effects of structure, purity, and alignment on the specific thermal conductivity of carbon nanotube films are illustrated in Figure 5 at different temperatures. The specific thermal conductivity of the A-type film is lower than that of the other-type films. Multi-walled carbon nanotubes generally have low thermal conductivity. The A-type film is composed mostly of multi-walled carbon nanotubes. Therefore, the specific thermal conductivity is lower than that of the film composed of single-walled carbon nanotubes. The specific thermal conductivity of the C-type film is higher than that of the A-type film, since the structure is different from each other. The structural variation will lead to the difference in thermal conductivity. However, the specific thermal conductivity of the C-type film is much lower than that of the D-type film. This is because the presence of non-carbonaceous impurities reduces the degree of bundle contact between single-walled carbon nanotubes, which increases the thermal resistance at the interface junctions and degrades the thermal performance of the C-type film.

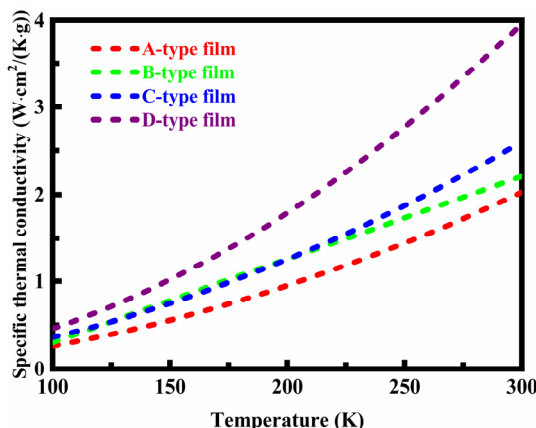


Figure 5. Specific thermal conductivity of the carbon nanotube films at different temperatures. There exist significant differences in terms of structure, purity, and alignment between the films.

While the specific thermal conductivity increases with temperature, the effect of temperature is different for the B-type film and the other-type films. The specific thermal conductivity of the B-type film has a linear relationship with temperature. For the other-type films, there is an exponential increase in specific thermal conductivity. The effect of temperature on thermal conductivity is illustrated in Figure 6 for the carbon nanotube films. The thermal conductivity of all the films presents power law dependence with temperature except that of the B-type film. The power law index is about 1.87, 1.80, and 1.96 for the thermal conductivity of the A, C, and D type films, respectively. In contrast, the temperature index is 0.99 for the thermal conductivity of the B-type film. The temperature index is small, which reduces the dimensionality of the propagation of phonons [31, 32] due to an increase in the degree of bundle alignment and contact.

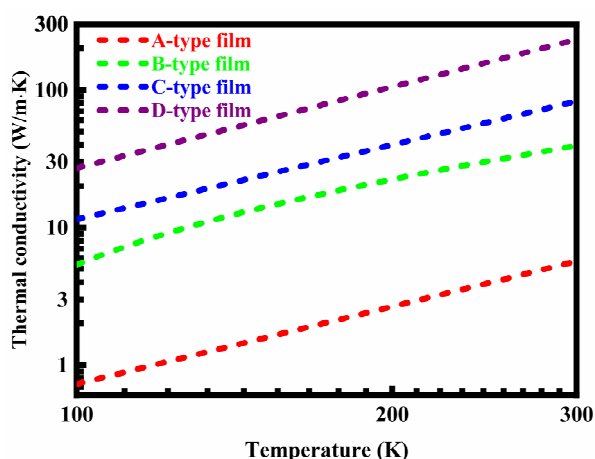


Figure 6. Thermal conductivity of the carbon nanotube films at different temperatures. The thermal conductivity is indicated with points plotted on a logarithmic coordinate system.

The effect of bulk density on the specific thermal conductivity at room temperature is illustrated in Figure 7 for the carbon nanotube films. At room temperature, the highest specific thermal conductivity is achieved for the D-type film. In addition, the power law index is largest, although the degree of bundle alignment is very low, which reduces the mechanical stiffness of the film. At room temperature, the lowest specific thermal conductivity is obtained for the A-type film. A tentative explanation could be made for the distinctive phenomenon. The specific thermal conductivity decreases

with increasing bulk density. The low bulk density of the D-type film compensates for the adverse effect of poor alignment on specific thermal conductivity. Therefore, the bulk density may be controlled to produce carbon nanotube films with high thermal conductivity.

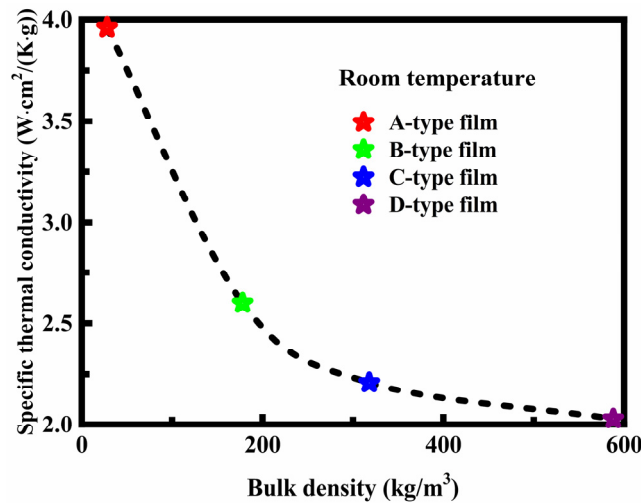


Figure 7. Effect of bulk density on the specific thermal conductivity of the carbon nanotube films at room temperature.

Thermal conductivity of carbon nanotube fibers

The effects of structure, purity, and alignment on the specific thermal conductivity of carbon nanotube fibers are illustrated in Figure 8 at different temperatures. The specific thermal conductivity of the fibers is around 10 W·cm²/(K·g) at room temperature, which is comparable to or higher than that of pristine and chemically modified carbon nanotube fibers [17, 18]. A maximum specific thermal conductivity is obtained at room temperature, which appears as a peak in the dependence of temperature in Figure 8, as determined previously [18, 32]. The maximum specific thermal conductivity represented by the peaks indicates the onset of Umklapp scattering. The Umklapp scattering is the dominant process for thermal resistivity, which limits the specific thermal conductivity. High thermal conductivity of carbon fibers is often associated with a high modulus of elasticity [33, 34]. Therefore, the carbon nanotube fibers have sufficient strength to be used as a reinforcement for composite materials. Clearly, the specific thermal conductivity of the fibers is significantly higher than that of the films. This is caused by the improved degree of bundle alignment for the fibers. A high degree of bundle alignment will lead to an increase in thermal conductivity due to the increased interfacial area between the carbon nanotubes.

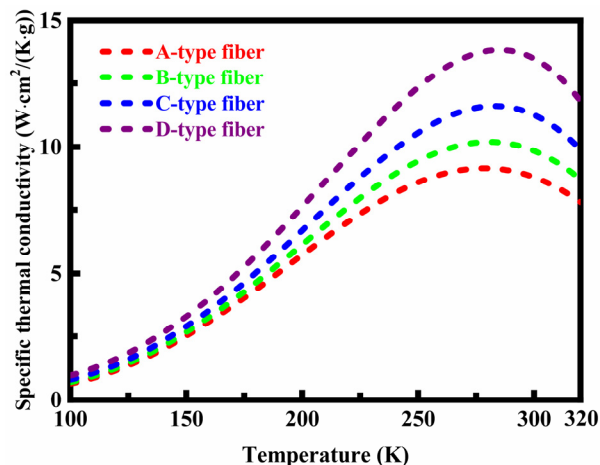


Figure 8. Specific thermal conductivity of the carbon nanotube fibers at different temperatures. There exist significant differences in terms of structure, purity, and alignment between the fibers.

The effect of cross-sectional area on the specific thermal conductivity at room temperature is illustrated in Figure 9 for the carbon nanotube films and fibers. Some previous data are also included for comparison. These previous data are available in the literature [18, 27, 28, 35-38]. The fibers have higher specific thermal conductivity than the films. Under the same cross-sectional area conditions, the specific thermal conductivity of the films and fibers is higher than that previously reported in the literature. The carbon nanotubes are of the order of several hundred microns, which is significantly greater than the phonon mean free path. As the length of carbon nanotubes increases, the effect of temperature on thermal conductivity becomes more pronounced [4, 38]. The length of the carbon nanotubes contained in

the films and fibers is much greater than that of the carbon nanotubes used in the literature. Consequently, the films and fibers are very efficient at conducting heat and typically have higher specific thermal conductivity in comparison to the previous data.

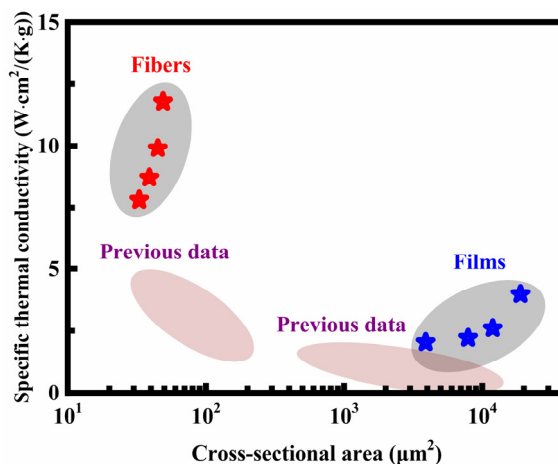


Figure 9. Effect of cross-sectional area on the specific thermal conductivity of the carbon nanotube films and fibers at room temperature. Some previous data are also included for comparison.

CONCLUSIONS

Carbon nanotube films and fibers were produced, and the parallel thermal conductance technique was employed to determine the thermal conductivity. The effects of carbon nanotube structure, purity, and alignment on the heat conduction properties of carbon films and fibers were investigated to understand the characteristics of thermal transport in the nanostructured material. The major conclusions are summarized as follows:

Multi-walled carbon nanotube films and fibers generally have low thermal conductivity.

The presence of non-carbonaceous impurities reduces the degree of bundle contact between carbon nanotubes, thereby increasing the thermal resistance at the interface junctions and degrading the thermal performance.

The thermal conductivity presents power law dependence with temperature or has a linear relationship with temperature.

The specific thermal conductivity decreases with increasing bulk density. Low bulk density can compensate for the adverse effect of poor alignment on specific thermal conductivity.

A maximum specific thermal conductivity is obtained at room temperature due to the onset of Umklapp scattering.

The specific thermal conductivity of carbon nanotube fibers is significantly higher than that of carbon nanotube films. The improved thermal properties are caused by the increased degree of bundle alignment.

The prepared carbon nanotube films and fibers are very efficient at conducting heat due to the increased length of the carbon nanotubes.

ORCID IDs

 Junjie Chen, <https://orcid.org/0000-0002-4222-1798>

REFERENCES

- [1] T.W. Ebbesen. Carbon nanotubes. *Physics Today*, **49**(6), 26 (1996), <https://doi.org/10.1063/1.881603>
- [2] Y. Ando, X. Zhao, T. Sugai, and M. Kumar. Growing carbon nanotubes. *Materials Today*, **7**(10), 22 (2004), [https://doi.org/10.1016/S1369-7021\(04\)00446-8](https://doi.org/10.1016/S1369-7021(04)00446-8)
- [3] K.S. Ibrahim. Carbon nanotubes-properties and applications: A review. *Carbon Letters*, **14**(3), 131 (2013), <http://dx.doi.org/10.5714/CL.2013.14.3.131>
- [4] E. Pop, D. Mann, Q. Wang, K. Goodson, and H. Dai. Thermal conductance of an individual single-wall carbon nanotube above room temperature. *Nano Letters*, **6**(1), 96 (2006), <https://doi.org/10.1021/nl052145f>
- [5] K.K. Koziol, D. Janas, E. Brown, and L. Hao. Thermal properties of continuously spun carbon nanotube fibres. *Physica E: Low-dimensional Systems and Nanostructures*, **88**, 104 (2017), <https://doi.org/10.1016/j.physe.2016.12.011>
- [6] B. Kumanek, and D. Janas. Thermal conductivity of carbon nanotube networks: A review. *Journal of Materials Science*, **54**(10), 7397 (2019), <https://doi.org/10.1007/s10853-019-03368-0>
- [7] E.T. Thostenson, C. Li, and T.-W. Chou. Nanocomposites in context. *Composites Science and Technology*, **65**(3-4), 491 (2005), <http://dx.doi.org/10.1016/j.compscitech.2004.11.003>
- [8] S. Rathinavel, K. Priyadarshini, and D. Panda. A review on carbon nanotube: An overview of synthesis, properties, functionalization, characterization, and the application. *Materials Science and Engineering: B*, **268**, 115095 (2021), <https://doi.org/10.1016/j.mseb.2021.115095>
- [9] N. Mingo, D.A. Stewart, D.A. Broido, and D. Srivastava. Phonon transmission through defects in carbon nanotubes from first principles. *Physical Review B*, **77**(3), 033418 (2008), <https://doi.org/10.1103/PhysRevB.77.033418>
- [10] C. Sevik, H. Sevinçli, G. Cuniberti, and T. Çağın. Phonon engineering in carbon nanotubes by controlling defect concentration. *Nano Letters*, **11**(11), 4971 (2011), <https://doi.org/10.1021/nl2029333>

- [11] P. Kim, L. Shi, A. Majumdar, and P.L. McEuen. Thermal transport measurements of individual multiwalled nanotubes. *Physical Review Letters*, **87**(21), 215502 (2001), <https://doi.org/10.1103/PhysRevLett.87.215502>
- [12] C. Chang, D. Okawa, H. Garcia, A. Majumdar, and A. Zettl. Breakdown of Fourier's Law in nanotube thermal conductors. *Physical Review Letters*, **101**(7), 075903 (2008), <https://doi.org/10.1103/PhysRevLett.101.075903>
- [13] K. Sääskilähti, J. Oksanen, S. Volz, and J. Tulkki. Frequency-dependent phonon mean free path in carbon nanotubes from nonequilibrium molecular dynamics. *Physical Review B*, **91**(11), 115426 (2015), <https://doi.org/10.1103/PhysRevB.91.115426>
- [14] T.S. Gspann, S.M. Juckes, J.F. Niven, M.B. Johnson, J.A. Elliott, M.A. White, and A.H. Windle. High thermal conductivities of carbon nanotube films and micro-fibres and their dependence on morphology. *Carbon*, **114**, 160 (2017), <https://doi.org/10.1016/j.carbon.2016.12.006>
- [15] X. Zhang, W.-X. Zhou, X.-K. Chen, Y.-Y. Liu, and K.-Q. Chen. Significant decrease in thermal conductivity of multi-walled carbon nanotube induced by inter-wall van der Waals interactions. *Physics Letters A*, **380**(21), 1861 (2016), <https://doi.org/10.1016/j.physleta.2016.03.040>
- [16] B. Goh, K.J. Kim, C.-L. Park, E.S. Kim, S.H. Kim, and J. Choi. In-plane thermal conductivity of multi-walled carbon nanotube yarns under mechanical loading. *Carbon*, **184**, 452 (2021), <https://doi.org/10.1016/j.carbon.2021.08.047>
- [17] E. Mayhew, and V. Prakash. Thermal conductivity of high performance carbon nanotube yarn-like fibers. *Journal of Applied Physics*, **115**(17), 174306 (2014), <https://doi.org/10.1063/1.4874737>
- [18] N. Behabtu, C.C. Young, D.E. Tsentlovich, O. Kleinerman, X. Wang, A.W.K. Ma, E.A. Bengio, R.F.T. Waarbeek, J.J.D. Jong, R.E. Hoogerwerf, S.B. Fairchild, J.B. Ferguson, B. Maruyama, J. Kono, Y. Talmon, Y. Cohen, M.J. Otto, and M. Pasquali. Strong, light, multifunctional fibers of carbon nanotubes with ultrahigh conductivity. *Science*, **339**(6116) 182 (2013), <https://doi.org/10.1126/science.1228061>
- [19] H.E. Misak, and S. Mall. Investigation into microstructure of carbon nanotube multi-yarn. *Carbon*, **72**, 321 (2014), <http://dx.doi.org/10.1016%2Fj.carbon.2014.02.012>
- [20] A.S. Wu, and T.-W. Chou. Carbon nanotube fibers for advanced composites. *Materials Today*, **15**(7-8), 302 (2012), [https://doi.org/10.1016/S1369-7021\(12\)70135-9](https://doi.org/10.1016/S1369-7021(12)70135-9)
- [21] H. Zhan, Y.W. Chen, Q.Q. Shi, Y. Zhang, R.W. Mo, and J.N. Wang. Highly aligned and densified carbon nanotube films with superior thermal conductivity and mechanical strength. *Carbon*, **186**, 205 (2022), <https://doi.org/10.1016/j.carbon.2021.09.069>
- [22] S. Li, X. Zhang, J. Zhao, F. Meng, G. Xu, Z. Yong, J. Jia, Z. Zhang, and Q. Li. Enhancement of carbon nanotube fibres using different solvents and polymers. *Composites Science and Technology*, **72**(12), 1402 (2012), <https://doi.org/10.1016/j.compscitech.2012.05.013>
- [23] B.M. Zawilski, R.T. Littleton IV, and T.M. Tritt. Description of the parallel thermal conductance technique for the measurement of the thermal conductivity of small diameter samples. *Review of Scientific Instruments*, **72**(3), 1770 (2001).
- [24] B.M. Zawilski and T.M. Tritt. Dynamic measurement access, a new technique for fast thermal conductivity measurement. *Review of Scientific Instruments*, **72**(10), 3937 (2001), <https://doi.org/10.1063/1.1347980>
- [25] M. Jakubinek, J.F. Niven, M.B. Johnson, B. Ashrafi, K.S. Kim, B. Simard, and M.A. White. Thermal conductivity of bulk boron nitride nanotube sheets and their epoxy-impregnated composites. *Physica Status Solidi (a) - applications and materials science*, **213**(8), 2237 (2016), <https://doi.org/10.1002/pssa.201533010>
- [26] J.-H. Pöhls, M.B. Johnson, M.A. White, R. Malik, B. Ruff, C. Jayasinghe, M.J. Schulz, and V. Shanov. Physical properties of carbon nanotube sheets drawn from nanotube arrays. *Carbon*, **50**(11), 4175 (2012), <http://dx.doi.org/10.1016%2Fj.carbon.2012.04.067>
- [27] J.F. Niven, M.B. Johnson, S.M. Juckes, M.A. White, N.T. Alvarez, and V. Shanov. Influence of annealing on thermal and electrical properties of carbon nanotube yarns. *Carbon*, **99**, 485 (2016), <https://doi.org/10.1016/j.carbon.2015.12.014>
- [28] M.B. Jakubinek, M.B. Johnson, M.A. White, C. Jayasinghe, G. Li, W. Cho, M.J. Schulz, and V. Shanov. Thermal and electrical conductivity of array-spun multi-walled carbon nanotube yarns. *Carbon*, **50**(1), 244 (2012), <https://doi.org/10.1016/j.carbon.2011.08.041>
- [29] ISO 1973:2021. *Textile fibres - Determination of linear density - Gravimetric method and vibroscope method. Edition: 3*, Number of pages: 10, Publication date: 2021, ICS Code: 59.060.01 Textile fibres in general *Including mixtures of fibres.
- [30] ASTM D1577-07(2018). *Standard test methods for linear density of textile fibers. ASTM International, Book of Standards Volume: 07.01*, Developed by Subcommittee: 58, Number of pages: 11, ICS Code: 59.060.01 Textile fibres in general *Including mixtures of fibres.
- [31] P. Gonnet, Z. Liang, E.S. Choi, R.S. Kadambala, C. Zhang, J.S. Brooks, B. Wang, and L. Kramer. Thermal conductivity of magnetically aligned carbon nanotube buckypapers and nanocomposites. *Current Applied Physics*, **6**(1), 119 (2006), <https://doi.org/10.1016/j.cap.2005.01.053>
- [32] J. Hone, M.C. Llaguno, N.M. Nemes, and A.T. Johnson. Electrical and thermal transport properties of magnetically aligned single wall carbon nanotube films. *Applied Physics Letters*, **77**(5), 666 (2000), <https://doi.org/10.1063/1.127079>
- [33] F.G. Emmerich. Young's modulus, thermal conductivity, electrical resistivity and coefficient of thermal expansion of mesophase pitch-based carbon fibers. *Carbon*, **79**, 274 (2014), <https://doi.org/10.1016/j.carbon.2014.07.068>
- [34] D. Jang and S. Lee. Correlating thermal conductivity of carbon fibers with mechanical and structural properties. *Journal of Industrial and Engineering Chemistry*, **89**, 115 (2020), <https://doi.org/10.1016/j.jiec.2020.06.026>
- [35] L.M. Ericson, H. Fan, H. Peng, V.A. Davis, W. Zhou, J. Sulpizio, Y. Wang, R. Booker, J. Vavro, C. Guthy, A.N.G. Parra-Vasquez, M.J. Kim, S. Ramesh, R.K. Saini, C. Kittrell, G. Lavin, H. Schmidt, W.W. Adams, W.E. Billups, M. Pasquali, W.-F. Hwang, R.H. Hauge, J.E. Fischer, and R.E. Smalley. Macroscopic, neat, single-walled carbon nanotube fibers. *Science*, **305**(5689), 1447 (2004), <http://dx.doi.org/10.1126/science.1101398>
- [36] P. Liu, Z. Fan, A. Mikhilchan, T.Q. Tran, D. Jewell, H.M. Duong, and A.M. Marconnet. Continuous carbon nanotube-based fibers and films for applications requiring enhanced heat dissipation. *ACS Applied Materials & Interfaces*, **8**(27), 17461 (2016), <http://dx.doi.org/10.1021/acsami.6b04114>
- [37] J. Qiu, J. Terrones, J.J. Vilatela, M.E. Vickers, J.A. Elliott, and A.H. Windle. Liquid infiltration into carbon nanotube fibers: Effect on structure and electrical properties. *ACS Nano*, **7**(10), 8412 (2013), <https://doi.org/10.1021/nn401337m>

- [38] A.E. Aliev, C. Guthy, M. Zhang, S. Fang, A.A. Zakhidov, J.E. Fischer, and R.H. Baughman. Thermal transport in MWCNT sheets and yarns. *Carbon*, **45**(15), 2880 (2007), <http://dx.doi.org/10.1016%2Fj.carbon.2007.10.010>

ВПЛИВ РІЗНИХ ЧИННИКІВ НА ВЛАСТИВОСТІ ТЕПЛОПРОВІДНОСТІ ВУГЛЕЦЕВИХ ПЛІВОК ТА ВОЛОКОН
Цзюньцзе Чен

*Факультет енергетики та енергетичного машинобудування, Школа машинобудування та енергетики,
Політехнічний університет Хенань, Проспект 2000 Століття, Яожуо, Хейнань, 454000, Китай*

Зростаюча популярність вуглецевих нанотрубок створила потребу в більш глибокому науковому розумінні характеристик теплового транспорту в наноструктурних матеріалах. Проте вплив домішок, зміщення та структурних факторів на теплопровідність плівок і волокон вуглецевих нанотрубок досі мало вивчений. Були виготовлені плівки та волокна вуглецевих нанотрубок, і для визначення їх теплопровідності використовувався метод паралельної теплопровідності. Щоб зрозуміти характеристики теплового транспорту в наноструктурному матеріалі було досліджено вплив структури вуглецевих нанотрубок, чистоти та вирівнювання на теплопровідність вуглецевих плівок і волокон. Значення об'ємної маси та площі поперечного перерізу було визначено експериментально. Результати показали, що підготовлені плівки та волокна вуглецевих нанотрубок дуже ефективно проводять тепло. Структура, чистота і вирівнювання вуглецевих нанотрубок відіграють принципово важливу роль у визначенні властивостей теплопровідності вуглецевих плівок і волокон. Одностінні плівки та волокна вуглецевих нанотрубок зазвичай мають високу теплопровідність. Наявність неуглецевих домішок погіршує теплотехнічні характеристики через низький ступінь контакту пучка. Теплопровідність може представляти залежність степеневого закону від температури. Питома теплопровідність зменшується із збільшенням об'ємної маси. При кімнатній температурі досягається максимальна питома теплопровідність, але відбувається Umklapp розсіювання. Питома теплопровідність волокон вуглецевих нанотрубок значно вища, ніж у плівок вуглецевих нанотрубок через підвищений ступінь вирівнювання пучків.

Ключові слова: вуглецеві нанотрубки; теплові властивості; вуглецеві волокна; теплопровідність; наноструктурні матеріали; Umklapp розсіювання

THE FEATURES OF INTENSE ELECTRON FLOW IMPACT ON METAL HYDRIDE ELECTRODE[†]

 Ihor Sereda*,  Yaroslav Hrechko,  Ievgeniia Babenko,  Mykola Azarenkov

V.N. Karazin Kharkiv National University, Kurchatov av. 31, 61108, Kharkiv, Ukraine

*Corresponding author: igorsereda@karazin.ua

Received April 19, 2022; accepted May 19, 2022

The features of generation of a shielding plasma layer by a Zr₅₀V₅₀ metal hydride surface which prevents the sample from melting have been studied. The sample was interacting with an electron beam formed directly by the metal hydride. The electron beam was emitted from primary plasma generated by an additional discharge with a filament cathode and accelerated in the space charge layer at the front of the shielding plasma, which is formed on hydrogen desorbed from metal hydride or on the sample material in case of the depletion of stored hydrogen. Three different stages of the formation of shielding plasma layer have been identified depending on the ratio between the current to the metal hydride I_{MH} and the current of the primary plasma source I_d . When $I_{MH}/I_d < 1$ the classical conditions for charged particles transfer are realized. At $I_{MH}/I_d > 1$ the classical conditions for the transfer of charged particles are violated and double layer appears at the front of the shielding plasma, which ensures the efficient energy transfer from external electrical field to the energy of bipolar motion of charged particles.

Keywords: metal hydride, plasma shielding layer, electron flux

PACS: 29.25.Bx, 81.40.Wx

The application of metal hydrides as protective elements of structural materials for plasma devices has been expressed in [1-2]. Under the material subjection to high thermal and energy loads the formation of a shielding plasma layer protects the surface from an incident plasma flow and prevents its erosion. The most suitable materials for the practical application are getters based on ZrV alloys [3]. These materials are characterized by low equilibrium pressures, high velocities and large thermal effects of sorption-desorption of hydrogen isotopes. Due to the decomposition of hydride phases plasma energy dissipation occurs on a gas-dynamic shielding target, which is formed self-consistently by the surface and prevents from the erosion of plasma facing surface.

The studies on coaxial plasma accelerators RPI and QSPA have shown that a protective layer is formed by the surface for hundreds of nanoseconds with an average density higher than 10^{17} cm⁻³ and an electron temperature of 5 eV. The duration of the plasma shielding layer is significantly longer than the time of plasma stream propagation (~ 3 μs). In case of RPI there were no spectral lines of the components of metal hydride matrix from the protective layer [1]. But the shielding effect of course is not absolute. Increasing the energy density of plasma stream from 15 J/cm² (RPI) to 30 J/cm² (QSPA) resulted in the surface layer melting and weight losses of the sample [2].

Stationary bombardment by high-energy hydrogen particles (5 keV, 100 mA/cm²) [3] and Ar⁺ ions (8 keV, 1.5 μA/cm²) [4] was also revealed the sputtering of metal hydride surface. But, the sputtering rate of the metal hydride was nevertheless significantly lower compared to materials that do not form hydride phases.

Thus, the interaction of metal hydride with plasma flows or with flows of positive ions has been carefully studied, whereas interaction with electron fluxes has not yet been considered. The purpose of this work is to study the features of the influence of an electron beam on the generation of shielding plasma and the processes of melting of the sample, which could be promising in case of current disruption in plasma devices.

EXPERIMENTAL SETUP

The experiments were carried out using a plasma source based on a reflective discharge with a filament cathode mounted to a vacuum chamber (Fig. 1). The source operation was released by the application of the negative potential $U_d = -100$ V to the filament cathode (anode and the vacuum chamber was grounded) and hydrogen injection from balloon to the region of the filament cathode to the pressure of $\sim 2 \cdot 10^{-4}$ Torr. The discharge current was $I_d = 1$ A. The plasma source was in a longitudinal bell-shaped magnetic field with a maximum intensity of 0.06 T in order to form a diverging stream of primary plasma to the vacuum chamber. It allows to obtain sufficiently dense ($\sim 10^{10}$ cm⁻³) primary plasma in the chamber at low pressures ($\sim 10^{-4}$ Torr). The shielding plasma layer 5 was formed around the tungsten holder 6 with metal hydride element 7, which was under positive potential $+V_{MH}$.

The metal-hydride element was produced from the alloy of Zr₅₀V₅₀ by the standard method [5]. It includes an alloy activation and filling with hydrogen. Then crushed hydride was mixed with a copper powder followed by pressing it in a disk 20 mm in diameter with a thickness of 4 mm. The quantity of accumulated hydrogen in produced electrode was measured by Siverts method [5] and was about 800 cm³ under normal conditions.

The decomposition of the hydride phases followed by hydrogen desorption is also accompanied by energy absorption, which limits the temperature of the sample and prevents its melting. At low temperatures of 80 – 350 °C the

[†] Cite as: I. Sereda, Y. Hrechko, I. Babenko, and M. Azarenkov, East Eur. J. Phys. 2, 99 (2022), <https://doi.org/10.26565/2312-4334-2022-2-12>
© I. Sereda, Y. Hrechko, Ie. Babenko, M. Azarenkov, 2022

desorption is caused by the decomposition of intermetallic hydrides ZrV_2H_x , and further by the destruction of the zirconium hydride in the temperature range of 400 – 650 °C [5].

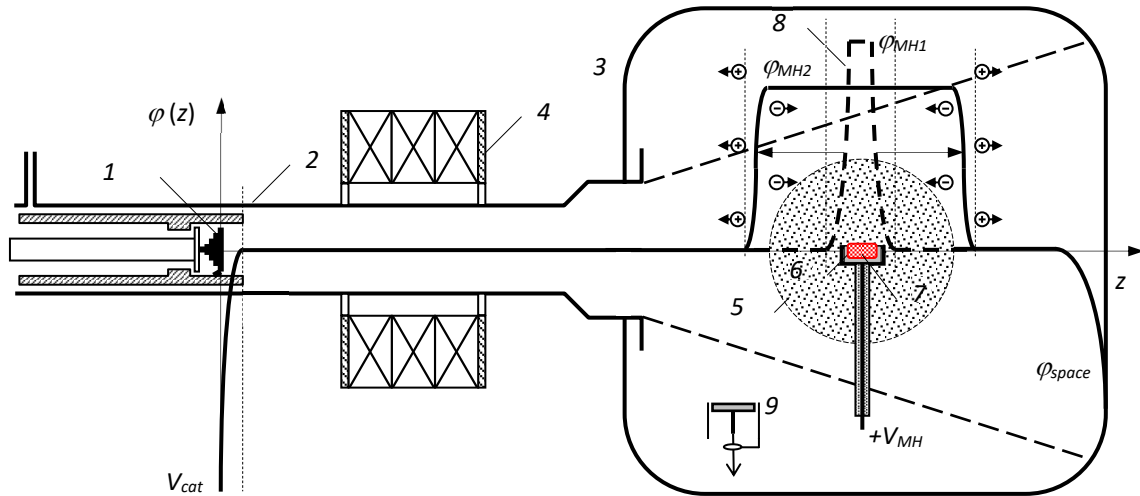


Figure 1. The scheme of experiment

1 – filament cathode, 2 – discharge tube, 3 – vacuum chamber, 4 – magnetic field coils, 5 – shielding plasma layer, 6 – tungsten holder, 7 – metal-hydride element, 8 – potential distribution near the metal-hydride, 9 – flat probe

The dynamics of floating plasma potential φ_{space} was registered by a flat probe 9, which was installed in the chamber outside the plasma source stream. Assuming that the voltage V_{MH} is redistributed only between the anode layer and the grounded chamber wall, one can calculate the potential in the layer near the metal hydride element: $\varphi_{MH} = V_{MH} - |\varphi_{space}|$

RESULTS AND DISCUSSION

The application of positive potential $+V_{MH}$ to the metal hydride element resulted in the formation of a space charge layer with a potential drop φ_{MH1} near its surface. In the layer the electrons from primary plasma are accelerated, and an electron beam is formed that heats the metal hydride. As the sample heats up, a flow of neutral atoms of desorbed hydrogen appears. Due to the electron impact ionization the part of loaded energy from the primary plasma is spent on the ionization and excitation of neutral hydrogen. The more power is loaded in, the greater hydrogen amount is desorbed and the denser shielding plasma is formed by the surface.

At low power of ~ 20 W ($I_{MH} \approx 0.1$ A, $V_{MH} = 200$ V) supplied to the metal hydride the pressure in the chamber increased from 2×10^{-4} Torr to 6×10^{-4} Torr after about 30 seconds of continuous exposure and the shielding plasma layer with potential φ_{MH1} was formed (1st stage). All the positive voltage applied to the metal hydride V_{MH} is concentrated in the layer near the surface φ_{MH1} , the space potential has a small negative potential ($\varphi_{space} \sim T_e/e$) and the dependence of V_{MH} on φ_{MH1} is linear (Fig. 2a green line).

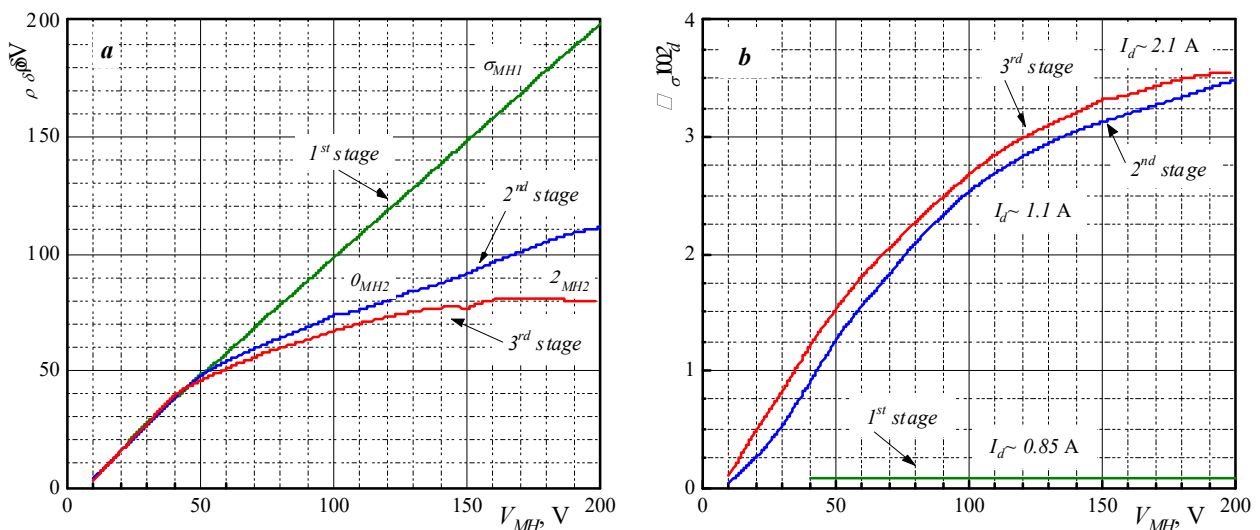


Figure 2. The dependence of potential φ_{MH} in the layer near the metal hydride element (a) and ratio of the metal hydride current to discharge current I_{MH}/I_d (b) on the voltage applied to the metal hydride element V_{MH}

The current to the metal hydride I_{MH} is less than the discharge current of the primary plasma source $I_d \sim 0.85$ A and doesn't depend on the voltage applied to the metal hydride V_{MH} (Fig.2b green line).

A further increase of the power supplied to the metal hydride element to 60 W ($V_{MH} = 600$ V at a constant current $I_{MH} \approx 0.1$ A) leads to a significant increase of hydrogen desorption rate (the pressure raised to 5×10^{-3} Torr) and the current to the metal hydride drastically jumps (2nd stage).

In this stage dense ($n > 10^{10}$ cm⁻³) shielding hydrogen plasma forms around the metal hydride, immersed in lower density primary plasma (Fig. 1). Starting from $I_{MH}/I_d = 1$, the classical conditions for the charged particles transfer are violated, because there are no longer enough ions generated in the primary plasma to cover the excess current on the metal hydride. The initial surface layer φ_{MHI} turns into double electric layer (DL) φ_{MH2} at the front of the shielding plasma, where the intense electron and ion beams are accelerated in the opposite directions [6].

An increase in the slope of the blue curve (Fig.2a) indicates on a redistribution of applied to metal hydride voltage V_{MH} between the DL potential φ_{MH2} and the φ_{space} potential.

Appearing of the positive potential near the wall rises the current to the metal hydride. The chamber wall plays the role of the cathode of a non-self-sustaining glow discharge, providing additional generation of charged particles in the chamber. The metal hydride plays the role of an anode.

Spending the energy loaded from primary plasma on the ionization and excitation of neutral hydrogen released from metal hydride causes the shielding properties of the plasma formed around the sample. The decomposition of hydride phases followed by hydrogen desorption is also accompanied by energy absorption, which limits the temperature of the sample and prevents its melting.

When all stored hydrogen is desorbed from metal hydride the shielding plasma conditionally transits to the 3rd stage (red curves in Fig. 2). The physical processes here develop according to a similar scenario but more intense. The shielding plasma layer is formed on the sample material, but not on the desorbed hydrogen. For process stability of shielding plasma formation, we had to increase the discharge current of the primary plasma source to $I_d \sim 2.1$ A.

There are no longer any limiting factors for increasing the sample temperature, and when supplied power is about 60 W ($I_{MH} \approx 0.1$ A, $V_{MH} \approx 600$ V) the melting process of the sample begins after about 30 second. Fig. 3 shows the photo of metal hydride surface after the impact of electron flow. Fig. 3a corresponds to the case of shielding plasma formation under hydrogen release from metal hydride, Fig. 3b – to the case of hydrogen depletion in metal hydride.

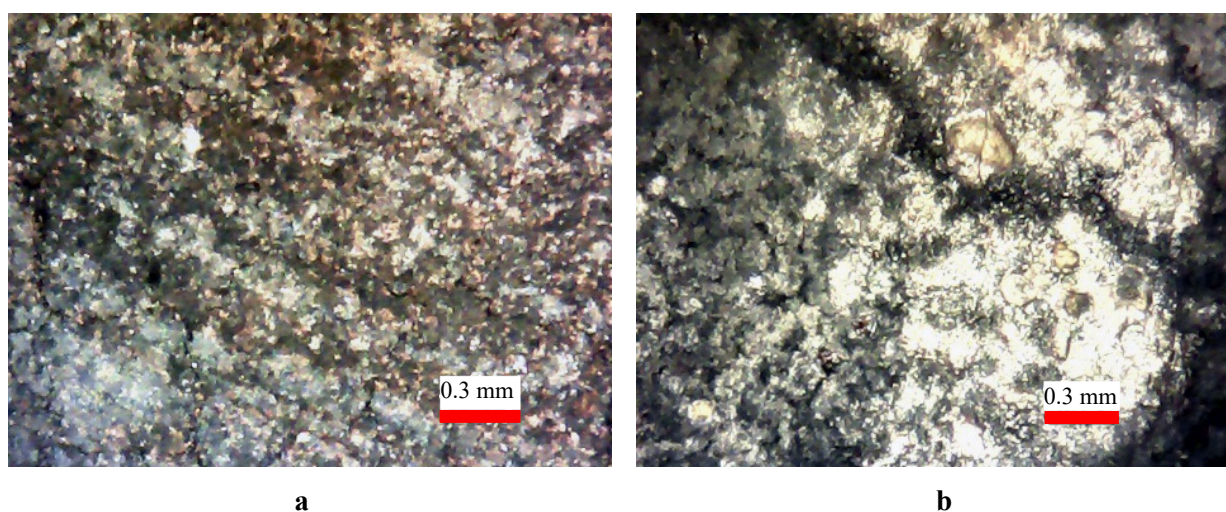


Figure 3. The photo of metal hydride surface after the impact of electron flow
a – the case of hydrogen release from metal hydride; b – the case of hydrogen depletion in metal hydride.

The DL formation at the front of the shielding plasma in case of hydrogen depletion is the most dangerous, because of addition damage of the sample material (Fig. 3b), deposition on the ambient surfaces and hydrogen plasma contamination.

CONCLUSION

Thus, we can assume the following scenario for the interaction of intense electron flow with the metal hydride. A shielding plasma layer is formed on hydrogen released from metal hydride, which shields the surface from extreme heat and energy loads.

When the current to metal hydride is less than the current of plasma source ($I_{MH}/I_d < 1$), the applied voltage V_{MH} is concentrated in the layer near its surface φ_{MHI} , and the wall has only a small ($\varphi_{space} \sim T_e/e$) negative potential.

If the current to metal hydride exceeds the current of primary plasma source ($I_{MH}/I_d > 1$), the classical conditions for the transfer of charged particles are violated and double layer (DL) appears at the front of the shielding plasma. Due to the redistribution of applied V_{MH} voltage between DL (φ_{MH2}) and near-wall layer it adjusts the current to metal hydride and ensures the efficient energy transfer from external electrical field to the energy of bipolar motion of charged particles.

Due to the energy absorption by hydride phases decomposition the formation of shielding plasma on released hydrogen occurs at limited temperatures which is significantly lower than the melting temperature of the sample. This makes the application of metal hydrides attractive as the materials of plasma facing elements.

ORCID IDs

 Ihor Sereda, <https://orcid.org/0000-0002-9111-9853>;  Yaroslav Hrechko, <https://orcid.org/0000-0001-9198-3660>
 Ievgeniia Babenko, <https://orcid.org/0000-0001-9339-3365>;  Mykola Azarenkov, <https://orcid.org/0000-0002-4019-4933>

REFERENCES

- [1] M.J. Sadowski, J. Baranowski, E. Skladnik-Sadowska, V.N. Borisko, O.V. Byrka, V.I. Tereshin, and A.V. Tsarenko, Characterization of pulsed plasma-ion streams emitted from RPI-type devices applied for material engineering, *Applied Surface Science*, **238**, 433 (2004), <https://doi.org/10.1016/j.apsusc.2004.05.167>
- [2] V.N. Borisko, I.E. Garkusha, V.V. Chebotarev, M.V. Lototsky, J. Langner, M.J. Sadowski, V.I. Tereshin, and Yu.F. Shmal'ko, Influence of high-power plasma streams irradiation on surface erosion behavior of reversible hydrogen getters, *J. Nucl. Mat.* **313-316**, 465 (2003), [https://doi.org/10.1016/S0022-3115\(02\)01366-1](https://doi.org/10.1016/S0022-3115(02)01366-1)
- [3] M.V. Lototsky, I. Tolj, L. Pickering, C. Sita, F. Barbir, and V. Yartys, The use of metal hydrides in fuel cell applications, *Progress in Natural Science*, **27**, 3 (2017), <https://doi.org/10.1016/j.pnsc.2017.01.008>
- [4] I.I. Okseniuk, V.O. Litvinov, D.I. Shevchenko, R.L. Vasilenko, S.I. Bogatyrenko, and V.V. Bobkov, Hydrogen interaction with Zr-based getter alloys in high vacuum conditions: In situ SIMS-TPD studies, *Vacuum*, **197**, 110861 (2022), <https://doi.org/10.1016/j.vacuum.2021.110861>
- [5] Z. Free, Z. Hernandez, M. Mashal, and K. Mondal, A Review on Advanced Manufacturing for Hydrogen Storage Applications. *Energies*, **14**, 8513 (2021), <https://doi.org/10.3390/en14248513>
- [6] L.P. Block, A double layer review, *Astrophysics and Space Science*, **55**, 59 (1978), <http://dx.doi.org/10.1007/BF00642580>

ОСОБЛИВОСТІ ВЗАЄМОДІЇ ІНТЕНСИВНОГО ПОТОКУ ЕЛЕКТРОНІВ З МЕТАЛОГІДРИДНИМ ЕЛЕКТРОДОМ Ігор Серєда, Ярослав Грєчко, Євгенія Бабєнко, Микола Азарєнков

Харківський національний університет імені В.Н. Каразіна, просп. Курчатова 31, 61108, Харків, Україна

Досліджено особливості формування захисного плазмового шару біля поверхні металогідриду $Zr_{50}V_{50}$, що перешкоджає плавленню зразка. Зразок взаємодіє з електронним пучком, що формується безпосередньо біля гідриду металу. Електронний пучок вилучався з первинної плазми, що генерується додатковим розрядом з катодом, що розжарюється, і прискорювався в шарі об'ємного заряду на фронті екрануючої плазми, що утворюється на водні, який десорбується з металогідриду, або на матеріалі зразка, у разі виснаження запасів водню. Виявлено три різні етапи формування екрануючого плазмового шару залежно від співвідношення струму на гідрид металу I_{MH} та струму первинного джерела плазми I_d . Коли $I_{MH}/I_d < 1$ реалізовано класичні умови перенесення заряджених частинок. При $I_{MH}/I_d > 1$ порушуються класичні умови перенесення заряджених частинок і на фронті екрануючої плазми виникає подвійний шар, що забезпечує ефективний переїс енергії від зовнішнього електричного поля до енергії біполярного руху заряджених частинок.

Ключові слова: гідрид металу, плазмовий екрануючий шар, потік електронів

STRUCTURAL, THERMAL, AND ELECTRONIC INVESTIGATION OF $ZrCo_{1-x}Ni_xBi$ ($x = 0, 0.25, 0.75$ and 1) HALF-HEUSLER ALLOYS[†]

 **Mahmoud Al-Elaimi**

Department of Basic Sciences, Preparatory Year Deanship, University of Ha'il, Ha'il, Saudi Arabia

E-mail: m.alelaimi@gmail.com

Received April 14, 2022; accepted May 15 2022

This article presents the theoretical evaluation of the structural, mechanical, thermal and electrical properties of half-Heusler $ZrCo_{1-x}Ni_xBi$ ($x = 0, 0.25, 0.75$ and 1) alloys in the framework of density functional theory (DFT) that is implemented in WIEN2k code. Equilibrium lattice parameters are found agree with previous literature. Several calculated mechanical properties are revealed that all studied alloys are mechanically stable. According to the critical values for B/G, Ni-doped $ZrCoBi$ alloys are ductile, whereas $ZrCoBi$ and $ZrNiBi$ are brittle. The band structure and density of states of the present compounds show that $ZrCoBi$ has a semiconducting nature, while Ni-doped $ZrCoBi$ has a half-metallic nature. The structural reforms, brought to $ZrCoBi$ as the Ni-dopant concentration increases at the site of Co-atom, showed an increase in its metallicity, conductivity and ductility, and a decrease in its rigidity, stiffness, minimum thermal conductivity, melting and Debye temperatures. According to the results obtained, $ZrCo_{1-x}Ni_xBi$ ($x = 0, 0.25, 0.75$ and 1) alloys could have potential thermal and electronic applications.

Keywords: ZrCoBi; First principles; Half-Heusler compounds; Electronic structure; Ni/Co Substitution

PACS: 61.05.-a, 61.50.-f

Heusler alloys have been exploring since their first find in 1903 by Friedrich Heusler [1] for their promising characteristics, such as semi-metallicity [2], tunable band gap [3], magnetism [4], thermoelectricity [5], etc. Accordingly, they can be utilized, for instance, in piezoelectric [6], spintronics [7], optoelectronic [8], thermoelectric [9], shape memory alloys [10], and solar cell applications [11]. Half-Heusler alloys, with crystallize of $MgAgAs$ structure, have a 1:1:1 stoichiometry formulation XYZ with the $F\bar{4}3m$ space group [1]. X and Y atoms are the d - or f -block rare-earth or transition elements and Z is the p -block element [12]. The half-Heusler alloys which have 18 valence electrons (VE) exhibit semiconductors behavior, and the other alloys own a metallic character. The semiconductors half-Heusler alloys are closed-shell species, non-magnetic and semiconducting [13].

Nasir Mehmood et al. [14] have studied the structural, mechanical, elastic, electronic, magnetic, and optical properties theoretically of half-Heusler alloys RhCrZ ($Z = Si, Ge$). They found that both alloys are half-metallic, ductile, weak ferromagnetic, optically metallic and become transparent above 17 and 13 eV, respectively. Osafire O.E. et al. [15] reported a ductile half-metallic character in the γ -phase of the novel half-Heusler ZrMnAs (VE=16) alloy. They showed that ZrMnAs had a promising application in spintronics devices.

Bismuth-based materials have recently attracted many researchers. Yazdani-Kachoei, M. et al. [16] have investigated the structural and electronic properties of ZrCoBi and ZrRhBi. They found that these alloys have high Seebeck coefficient and low electrical conductivity making them good candidates for thermoelectric applications. Gokhan Surucu et al. [17] have shown that γ -phase structure of $XCoBi$ ($X: Ti, Zr, Hf$) half-Heusler alloys has the most stability structure depending on the computed formation enthalpies, Cauchy pressures and energy-volume dependencies. Hangtian Zhu et al. [18] have studied the thermoelectric performance of ZrCoBi-based half-Heuslers. They demonstrated that the ZrCoBi-based half-Heuslers are quite promising for mid- and high-temperature thermoelectric power generation.

Therefore, it is worthy to study this promising field to enhance its usage capability as well as to discover new compounds for further investigations. In this study, I aim to use the ab-initio calculations to investigate the structural, mechanical, thermal and electronic properties of Co substituting by Ni atoms in the half-Heusler ZrCoBi alloy, with concentration of 25%, 75% and 100%.

This paper is arranged as follows: Section "METHOD OF CALCULATIONS" describes the calculations method; Section "RESULTS AND DISCUSSION" presents the results and discussion of the calculated parameters. While, Section "CONCLUSION" recaps the mentioned and analyzed results.

METHOD OF CALCULATIONS

In this study, the calculations were performed using Full-Potential Linearized Augmented Plane Wave (FP-LAPW) method that depend on the density functional theory (DFT) [19], which is implemented in WIEN2k code [20]. For exchange-correlation (XC) potential, the generalized gradient approximation Perdew-Burke-Ernzerhof (PBE-GGA) is used [21]. The structural and electronic properties of $ZrCo_{1-x}Ni_xBi$ ($x = 0, 0.25, 0.75$ and 1) alloys were computed with 3000 k-points. The plane wave is applied in the interstitial site with a cutoff energy of $K_{max} = 8.0/R_{MT}$ where R_{MT} is the smallest of all atomic sphere radii. The k-points and $K_{max}R_{MT}$ values were estimated by the convergence test. The muffin-tin sphere radii (MT) were chosen to be 2.35,

[†] Cite as: M. Al-Elaimi, East Eur. J. Phys. 2, 103 (2022), <https://doi.org/10.26565/2312-4334-2022-2-13>

© M. Al-Elaimi, 2022

2.35 (2.37) and 2.47 a.u. for Zr, Co (Ni) and Bi, respectively. The self-consistent calculations are converged when the determined total energy and charge of the crystal became lower than 0.1×10^{-3} Ry and 0.1×10^{-3} e, respectively. The three independent elastic constants (C_{11} , C_{12} and C_{44}) are calculated from stress tensor matrix under small strains. These constants are used to investigate the elastic and thermal properties. The elastic constants, C_{ij} , were obtained by Charpin method using ElaStic code which is integrated within WIEN2k code [22]. The elastic constants are used to investigate the elastic and thermal properties.

RESULTS AND DISCUSSION

Structural properties

In the first step, the ground state structure characteristics of $ZrCo_{1-x}Ni_xBi$ ($x = 0, 0.25, 0.75$ and 1) alloys have been carried out at 0 K and 0 GPa. The cubic half-Heusler $ZrCo_{1-x}Ni_xBi$ ($x = 0, 0.25, 0.75$ and 1) alloys, which has $F\bar{4}3m$ space group, have Wyckoff positions at $(0, 0, 0)a$, $(\frac{1}{4}, \frac{1}{4}, \frac{1}{4})b$, and $(\frac{1}{2}, \frac{1}{2}, \frac{1}{2})c$ for Zr, Co (Ni) and Bi atoms, respectively. The optimized lattice constant (a) and bulk modulus (B) are calculated using Birch-Murnaghan's equation of states [23], as listed in Table 1 and shown in Fig. 1. The computed lattice parameters of ZrCoBi and ZrNiBi alloys are in agreement with the experimental study explained in ref. [24]. It is found that the unit cell volume of ZrCoBi increases directly with Ni-dopant concentration. This allows us to predict that ductility of alloys decreases as going from ZrCoBi to ZrNiBi alloy.

Table 1. The calculated lattice constant (a in Å), bulk modulus (B in GPa) and formation energy (ΔH_f in eV/unit cell) of $ZrCo_{1-x}Ni_xBi$ ($x = 0, 0.25, 0.75$ and 1) alloys.

Alloys	a (Å)	B (GPa)	ΔH_f (eV/unit cell)
ZrCoBi	6.232 6.179 [24]	126.10	-3.76
ZrCo _{0.75} Ni _{0.25} Bi	6.258	114.526	-14.47
ZrCo _{0.25} Ni _{0.75} Bi	6.280	99.695	-13.49
ZrNiBi	6.291 6.148 [24]	103.544	-3.26

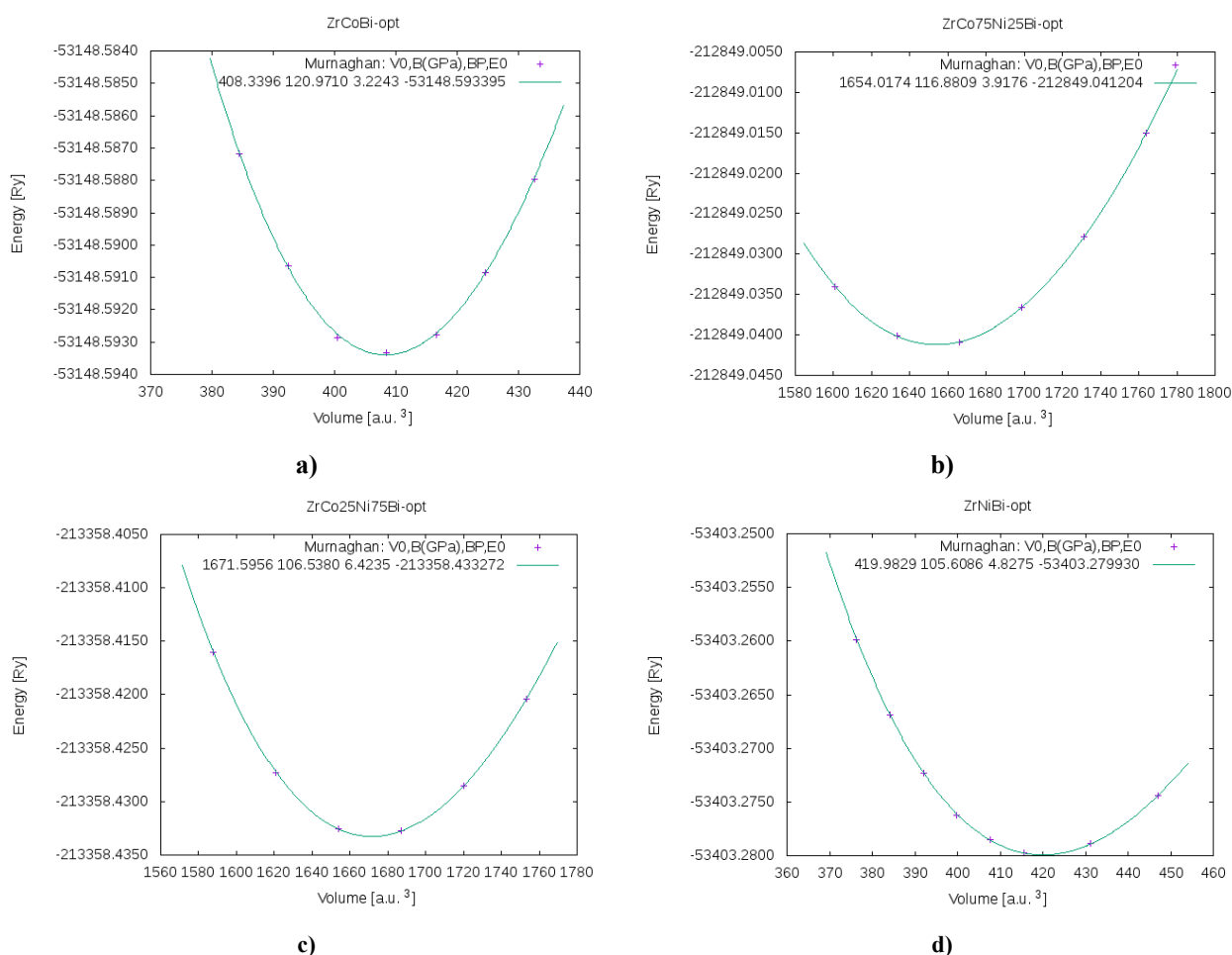


Figure 1. The energy-volume optimization graphs of $ZrCo_{1-x}Ni_xBi$ ($x = 0, 0.25, 0.75$ and 1) alloys (a) ZrCoBi; (b) ZrCo_{0.75}Ni_{0.25}Bi; (c) ZrCo_{0.25}Ni_{0.75}Bi; (d) ZrNiBi.

In order to study the stability of $ZrCo_{1-x}Ni_xBi$ alloys, the formation energy (ΔH_f) are calculated by comparing the fully minimized total energies ($E_{ZrCo_{1-x}Ni_xBi}$) with content atoms (E_{atom}) energies. ΔH_f is represented mathematically by

$$\Delta H_f = E_{ZrCo_{1-x}Ni_xBi} - n_{Zr}E_{Zr} - n_{Co}E_{Co} - n_{Ni}E_{Ni} - n_{Bi}E_{Bi} \quad (1)$$

where, n_{Zr} , n_{Co} , n_{Ni} and n_{Bi} are Zr, Co, Ni and Bi atoms numbers in the $ZrCo_{1-x}Ni_xBi$ unit cell, respectively.

The computed ΔH_f values for current compounds are negative, see Table 1, suggesting that these compounds are thermodynamically stable and can be synthesized experimentally.

The determination of three elastic constants, C_{11} , C_{12} and C_{44} , of a cubic alloy takes an important role. These constants are utilized to understand the mechanical characteristics. For instance, studying alloy behavior under mechanical stress provides acquaintance about its elastic rigidity and stability. Stress-strain method that is implemented in ab initio calculations makes it possible to determine these values with high precision. The calculated elastic parameters of the present alloys are listed in Table 2. The calculated values of C_{ij} satisfy the mentioned criteria formulae, $(C_{11} + 2C_{12})/3 > 0$; $C_{44} > 0$; $(C_{11} - C_{12})/2 > 0$; $C_{12} < B < C_{11}$, which is confirmed that the alloys are mechanically stable [25]. Moreover, it is noticed that C_{11} constant is quite higher than C_{12} and C_{44} constants for all studied alloys, leading to the fact that the alloys have higher resistance to be compressed in the x-direction. It is found that C_{11} values are 257.98%, 295.42%, 250.02%, and 220.73% higher than C_{44} for $ZrCoBi$, $ZrCo_{0.75}Ni_{0.25}Bi$, $ZrCo_{0.25}Ni_{0.75}Bi$, $ZrNiBi$, respectively. Hence, $ZrNiBi$ alloy has the lowest resistance, while $ZrCo_{0.75}Ni_{0.25}Bi$ has the highest resistance. Ni-doping modifies the whole alloy's microstructure and consequently increases its resistance to be compressed [26].

Table 2: The determined bulk modulus (B in GPa), shear modulus (G in GPa), Young's modulus (E in GPa), the three independent elastic constants (C_{11} , C_{12} and C_{44} in GPa), B/G ratio, Vicker's hardness (H_v in GPa), Cauchy pressure ($C_{12} - C_{44}$ in GPa), elastic anisotropy (A) and Kleinman parameter (ξ) of $ZrCo_{1-x}Ni_xBi$ ($x = 0, 0.25, 0.75$ and 1)

Properties		<i>ZrCoBi</i>	<i>ZrCo_{0.75}Ni_{0.25}Bi</i>	<i>ZrCo_{0.25}Ni_{0.75}Bi</i>	<i>ZrNiBi</i>
$B = (C_{11} + 2C_{12})/3$	(GPa)	126.048	114.798	100.071	104.134
G		81.662	60.663	51.535	89.086
E		201.476	154.733	131.954	207.957
C_{11}		257.585	212.045	173.141	249.533
C_{12}		60.279	66.175	63.537	31.435
C_{44}		71.955	53.625	49.465	77.801
B/G		1.544	1.892	1.942	1.169
H_v (GPa)		12.681	8.150	7.051	18.501
Cauchy pressure ($C_{12} - C_{44}$) (GPa)		-11.6755	12.5497	14.0711	-46.3662
ξ		0.385	0.459	0.509	0.277
A		0.729	0.735	0.907	0.713

The bulk modulus, $B = (C_{11} + 2C_{12})/3$, describes the resistance to fracture deformation. The calculated B values from C_{ij} agrees those determined by Birch-Murnaghan's equation of state, see Table 1. This assures the reliability of the computed elastic constants in the present study. The bulk modulus is found to decrease with increasing of the concentration of Ni-dopant and the unit cell volume; which articulates that the rigidity diminishes as going from $ZrCoBi$ to $ZrCo_{0.25}Ni_{0.75}Bi$, with a minute increase in the rigidity in $ZrNiBi$ alloy.

The elastic anisotropy of any material leads to the generation of microcracks and lattice distortion during and after the production process that limits its durability in practical applications. Therefore, evaluating the anisotropy factor, $A = 2C_{44}/(C_{11} - C_{12})$, of $ZrCo_{1-x}Ni_xBi$ ($x = 0, 0.25, 0.75$ and 1) alloys is necessary for development purposes. The alloy is presumed to be fully isotropic for $A = 1$, else the alloy is anisotropic. The $ZrCo_{1-x}Ni_xBi$ alloys are considered anisotropic as all calculated A values are deviating from 1 with $ZrCo_{0.25}Ni_{0.75}Bi$ being the lowest anisotropic alloy compared to the other alloys, as listed in Table 2.

Pugh's index of ductility ratio (B/G) value is used to examine the ductile and brittle character of the alloys. The alloy assumes brittle if this ratio is less than 1.75, otherwise it behaves in a ductile nature [27]. From the results in Table 2, I predict that the $ZrCoBi$ and $ZrNiBi$ alloys have a brittle nature with $ZrCoBi$ is more rigidity than $ZrNiBi$. Whereas $ZrCo_{0.75}Ni_{0.25}Bi$ and $ZrCo_{0.25}Ni_{0.75}Bi$ classify as ductile alloys and $ZrCo_{0.25}Ni_{0.75}Bi$ is more ductility than $ZrCo_{0.75}Ni_{0.25}Bi$.

I have also calculated the shear Modulus ($G = \frac{1}{2}(C_{11} - C_{12})$), to comprehend the dynamical stability of the alloys. The present alloys display a dynamical stability structure since $G > 0$.

The Young's modulus ($E = (9BG)/((3B) + G)$) is used to examine the stiffness of the alloys. Strong covalent bonds, where the alloys have also high rigidity, are expected when Young's modulus has a high value. Our results point out that the alloys stiffness decreases as increases the concentration of Ni-doped atom. This decreasing is due to the replacement of weak ionic bonds over covalent bonds in this case. Vicker's hardness criteria, $H_v = 0.92(G/B)^{1.137}G^{0.708}$, is used to check the alloys resisting ability. It is figured out that as Ni-dopant concentration increases, the alloy resistance ability to be dented

decreases. Pettifor and Johnson [28,29] suggested that the Cauchy pressure ($C_{12} - C_{44}$) parameter explains the nature of atomic bonding domination in the alloys. It is typically negative for directional bonding where the covalent bonds are majority. In this case the material resists against the shear strain (C_{44}) more strongly than with the volume change (C_{12}), whereas it is positive when ionic bonding is dominant. As shown in Table 2, the Cauchy pressure for ZrCoBi and ZrNiBi has a negative value, which portrays that the covalent bonding is a majority. While, for ZrCo_{1-x}Ni_xBi ($x = 0.25$ and 0.75) Cauchy pressure's value becomes positive upon alloying with Ni, pointing out a domination of ionic bonding for the Ni-doped alloys. Additionally, the dimensionless Kleinman parameter (ξ) is used to examine the prospect of the alloys to be stretched or bended. If ξ is close to zero (one), maximum bond stretching (bending) is expected, respectively. Among the studied alloys, ZrCo_{0.25}Ni_{0.75}Bi has the highest ξ , while ZrNiBi has the smallest ξ . This leads to the fact that ZrCo_{0.25}Ni_{0.75}Bi (ZrNiBi) alloy possesses minimum (maximum) bond stretching, respectively.

Thermal properties

In this subsection, I inspect the thermal characteristics, such as minimum thermal conductivity (Λ_{min}), sound velocities, Debye (Θ) and melting (T_M) temperatures, as listed in Table 3. The Debye temperature, $\Theta = \frac{h}{k} \left[\frac{3n}{4\pi} \left(\frac{N_A \rho}{M} \right) \right]^{\frac{1}{3}} V_m$, is an important parameter correlating with many physical and thermal properties of materials [27]. Where N_A , k and h are Avogadro, Boltzmann's and Plank's constants; M and ρ are molecular weight and density of the alloy; n is atoms number in a single cell and V_m stands for average sound velocity. $V_m, V_m = \left[\frac{1}{3} \left(\frac{2}{v_t^3} + \frac{1}{v_l^3} \right) \right]^{-\left(\frac{1}{3}\right)}$, can be calculated straight forward from the computed longitudinal ($v_l = \sqrt{\frac{3B+4G}{3\rho}}$) and transverse ($v_t = \sqrt{\frac{G}{\rho}}$) acoustic velocities. According to the results listed in Table 3, it is found that longitudinal acoustic velocity is larger than transverse acoustic velocity for all examined alloys. Additionally, longitudinal acoustic velocity specifically along [100] directions is the highest. The computed melting temperature ($T_M 553 + \frac{(5.91 \times C_{11})}{GPa}$) and Debye values suggest that the present alloys are tolerable candidates in electronic high-temperature applications. The suggested operational temperature T for electronic apparatuses must be restricted between Debye and melting temperatures, i.e. ($\Theta < T < T_M$).

Table 3. The average wave velocity (V_M in km/s), the longitudinal elastic wave velocity (v_l in km/s), the transverse elastic wave velocity (v_t in km/s), Debye temperature (Θ in K), melting temperature (T_M in K), the longitudinal and transverse sound velocities along specific directions ([100], [110], and [111]), minimum thermal conductivity at 0 K ($\Lambda_{min}(WK^{-1}m^{-1})$), and minimum thermal conductivity along specific directions ([100], [110], and [111]) of ZrCo_{1-x}Ni_xBi ($x = 0, 0.25, 0.75$ and 1).

Properties	ZrCoBi	ZrCo _{0.75} Ni _{0.25} Bi	ZrCo _{0.25} Ni _{0.75} Bi	ZrNiBi
$V_M(km/s)$	3.190	2.763	2.549	3.309
$v_l(km/s)$	4.883	4.457	4.140	4.758
$v_t(km/s)$	2.879	2.481	2.287	3.008
Θ (K)	349.315	333.034	307.193	362.375
$T_M \pm 300$ (K)	2075.329	1806.184	1576.263	2027.737
$v_l[100](km/s)$	5.113	4.639	4.193	5.034
$v_l[110](km/s)$	4.840	4.423	4.128	4.708
$v_l[111](km/s)$	4.746	4.348	4.106	4.594
$v_t[100](km/s)$	2.702	2.333	2.241	2.811
$v_t[110](km/s)$	4.475	3.848	3.336	4.706
$v_t[111](km/s)$	3.018	2.598	2.320	3.165
$\Lambda_{min}(WK^{-1}m^{-1})$	0.3171	0.3401	0.3146	0.3211
$\Lambda_{min}[100](WK^{-1}m^{-1})$	0.3134	0.3359	0.3132	0.3176
$\Lambda_{min}[110](WK^{-1}m^{-1})$	0.4110	0.4375	0.3899	0.4208
$\Lambda_{min}[111](WK^{-1}m^{-1})$	0.3213	0.3446	0.3158	0.3256

Knowing thermal conductivity is vital to ease predicting the thermal characteristics of a specific alloy. The thermal conductivity decreases with elevating temperature up to a particular limit which is referred to as minimum thermal conductivity (Λ_{min}). The determination of minimum thermal conductivity is important to enhance the thermal performance of the alloys under investigation. I have calculated Λ_{min} by Cahill model [30] that is given by the following formula:

$$\Lambda_{min} = \frac{(k_b)}{2.48} (n_o)^{\frac{2}{3}} (v_l + 2v_t), \text{ at } 0K \text{ for all alloys} \tag{2}$$

where n_o is the atoms number per unit volume.

To extend our knowledge of the minimum thermal conductivity effect along specific directions. Where these directions make is easy to grow crystals intentionally to design maximal or minimal thermally conductive devices. From our results enlisted in Table 3, I have observed that all $ZrCo_{1-x}Ni_xBi$ alloys have low thermal conductivity making them good candidates for high temperature applications such as thermal barrier coatings. However, it is found that $ZrCo_{0.25}Ni_{0.75}Bi$ has the smallest value of minimum thermal conductivity in all studied directions. The reduced value of thermal conductivity can be a result of substitutional point defect scattering induced by the Ni-dopant [31].

Electronic properties

The partial, total density of states (PDOS and TDOS), and band structure of $ZrCo_{1-x}Ni_xBi$ ($x = 0, 0.25, 0.75$ and 1) alloy are shown in Figs. 2 and 3, respectively. The properties of the studied alloys are demonstrated based on the electron's behavior around the Fermi level. Figures 2a and 3a show the semiconductor nature of $ZrCoBi$ alloy with a band gap value of 0.99 eV. This gap is confined between the d-states of Zr and Co and p-state of Bi in the valence band at Γ symmetry line the X symmetry line of d-states for Zr and Co in the conduction band. The computed band gap value of $ZrCoBi$ agrees with that found in the previous literatures [32].

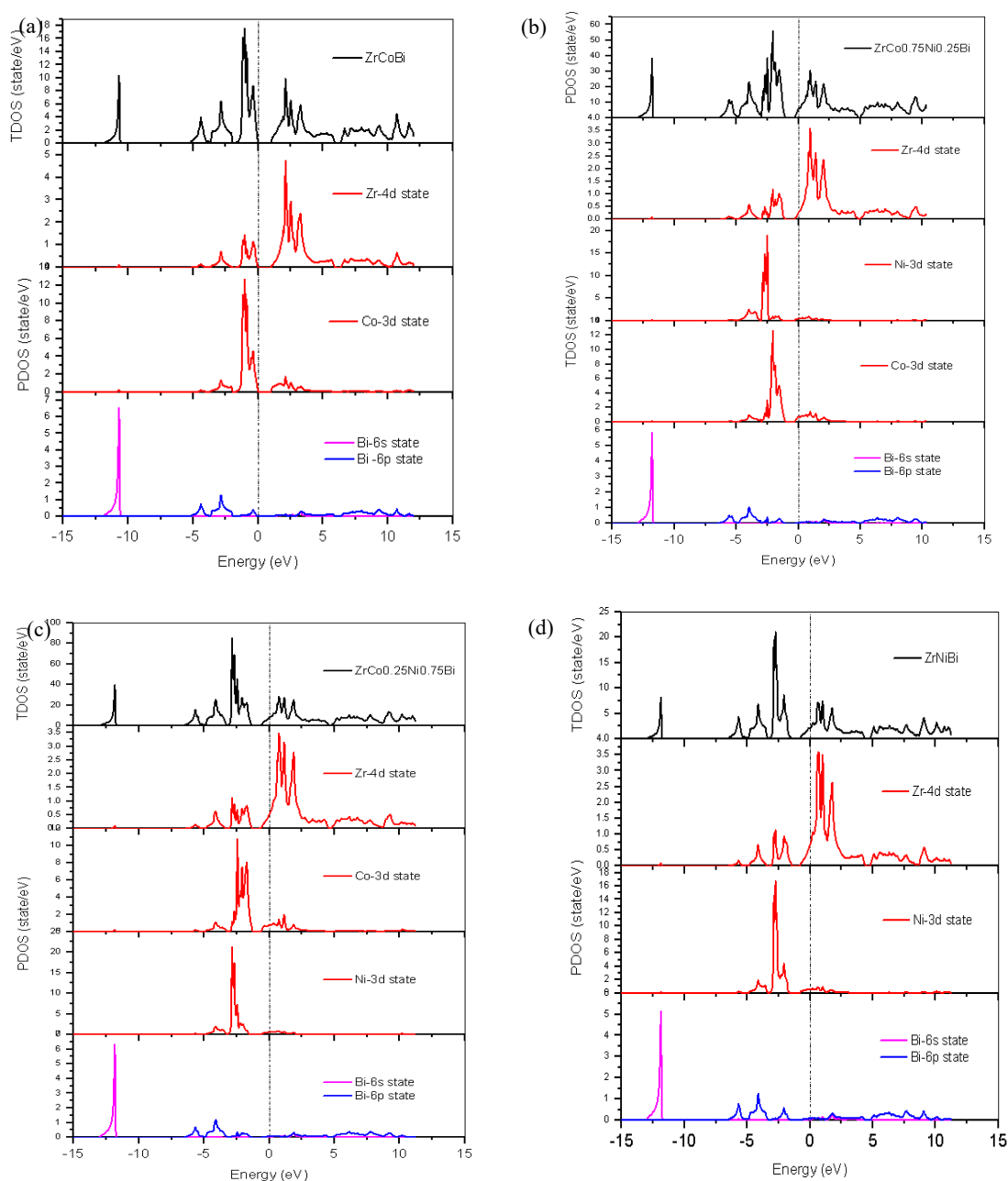


Figure 2. Graphs for density of states (TDOS and PDOS) of $ZrCo_{1-x}Ni_xBi$ ($x = 0, 0.25, 0.75$ and 1). The dashed lines represent Fermi level: (a) $ZrCoBi$; (b) $ZrCo_{0.75}Ni_{0.25}Bi$; (c) $ZrCo_{0.25}Ni_{0.75}Bi$; (d) $ZrNiBi$

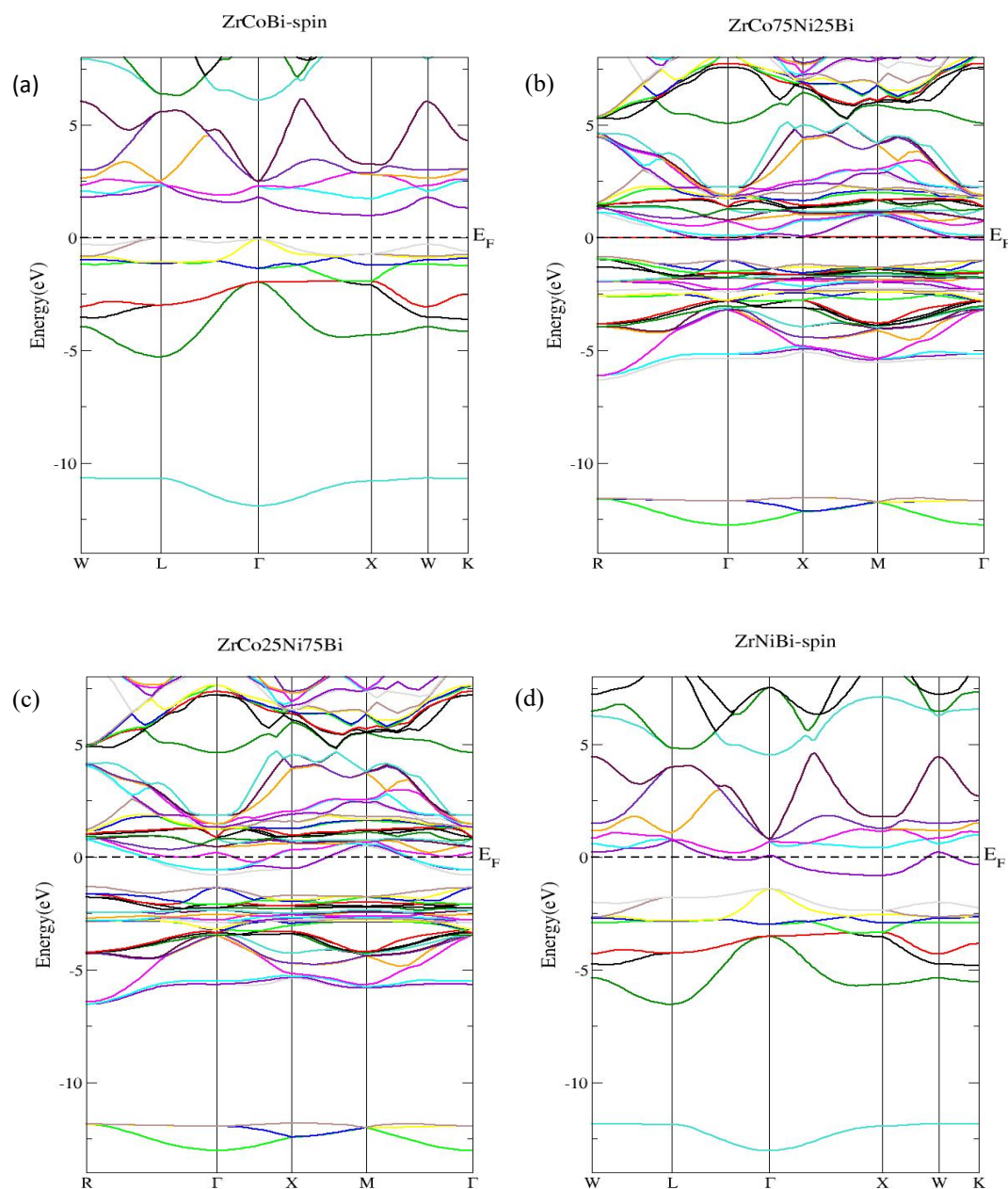


Figure 3. Graphs for energy band structure along the symmetry points of $ZrCo_{1-x}Ni_xBi$ ($x = 0, 0.25, 0.75$ and 1). The dashed lines represent Fermi level: (a) $ZrCoBi$; (b) $ZrCo_{0.75}Ni_{0.25}Bi$; (c) $ZrCo_{0.25}Ni_{0.75}Bi$; (d) $ZrNiBi$.

It is noticed that Ni-doping increases the number of valence electrons, and shifts the electronic states of the content atoms for the $ZrCoBi$ alloy to the low energy level. The d-state of Zr and Co crosses Fermi level and changes the alloy nature from semiconducting to half-metallicity. This doping changes the band gap to the direct (Γ - Γ) and decreases this gap to 0.62 and 0.24 eV for $ZrCo_{0.75}Ni_{0.25}Bi$ and $ZrCo_{0.25}Ni_{0.75}Bi$, respectively. Our electronic results agree with the previous calculations [33,34].

In order to study the bonding nature of $ZrCo_{1-x}Ni_xBi$ alloys, the charge density difference is also performed. Figure 4 displays the charge density difference along (110) plane that uses to explain the bonding nature of the $ZrCo_{1-x}Ni_xBi$ alloys. The charge contours are perfectly spherical and isolated around Co – Ni, Bi – Co, Bi – Ni and Zr – Bi atoms that denote the ionic bonding among them. However, the charge contours for Zr are not completely spherical and dented which means the electronic orbit is not fully filled. The charges transfer from Zr to Co and Ni due to the electronegativity difference. This creates the induced dipole moment toward Zr atom. The charge contours around Zr – Co and Zr – Ni atoms denote the covalent bonding among them. The Zr – Bi and Bi – Co (Bi – Ni) ionic bonds are existed due to pd-hybridization between Zr 3d and Bi 5p states and from pd-hybridization of Bi 5p and Co 3d (Ni 3d), respectively. It can be assumed that bonding nature of the current alloys is a mixed between a covalent and ionic bond.

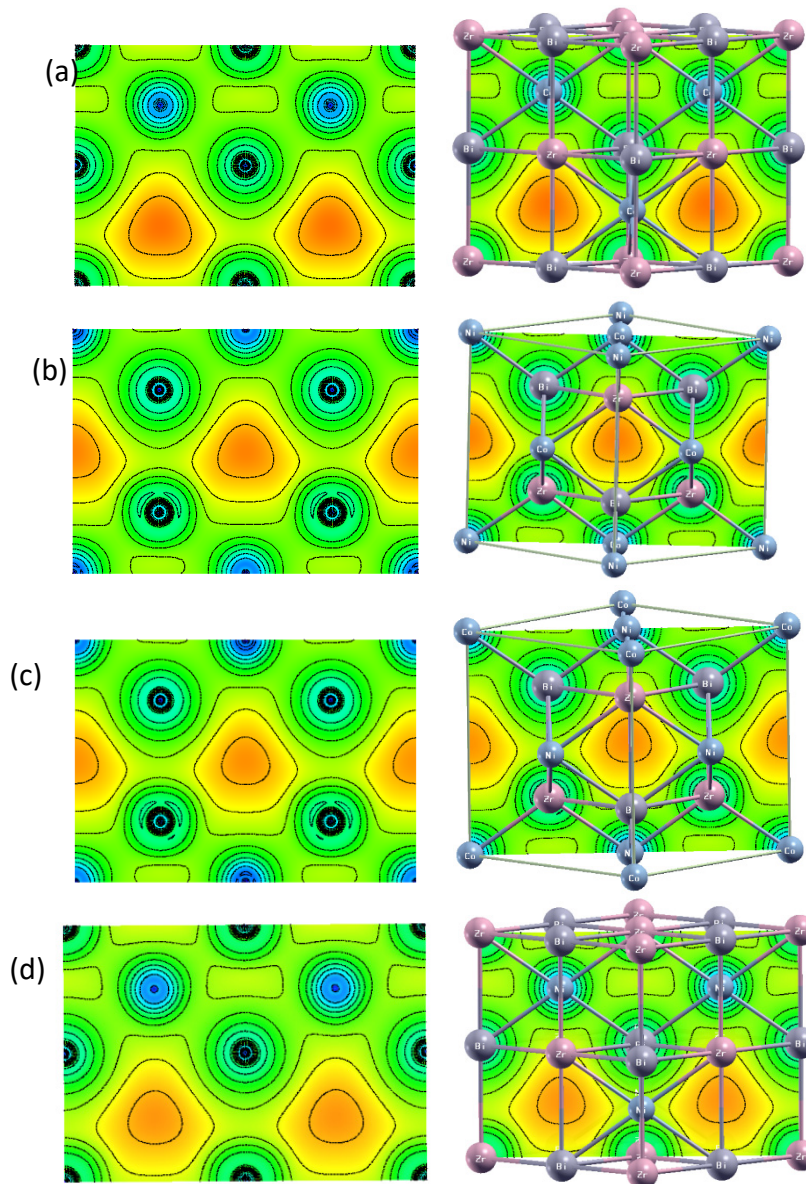


Figure 4. The charge density difference diagrams along (110) plane of (a) $ZrCoBi$, (b) $ZrCo_{0.75}Ni_{0.25}Bi$, (c) $ZrCo_{0.25}Ni_{0.75}Bi$, and (d) $ZrNiBi$

CONCLUSION

In this article, I have carried out ab initio study on $ZrCo_{1-x}Ni_xBi$ ($x = 0, 0.25, 0.75$ and 1) alloys, predicting their structural, thermal and electronic characteristics using full-potential linearized augmented plane wave method.

I enumerate the important conclusions of our DFT calculations as follows:

- (i) All studied alloys are mechanically, thermodynamical stable and can be formed depending on formation energy, elastic constants and elastic moduli criteria.
- (ii) It is found that $ZrCo_{1-x}Ni_xBi$ elastic moduli, rigidity, stiffness, resistance to be dented, Debye and melting temperatures, minimum thermal conductivity, and band gap energy decrease as Ni -atom concentration in Co site increases.
- (iii) It is also found that $ZrCo_{1-x}Ni_xBi$ ductility, metallicity, conductivity, and ionic bonding nature increase as Ni -atom concentration in Co site increases.
- (iv) The band gap calculation shows that $ZrCoBi$ exhibits a semiconducting behavior, whereas Ni -doped $ZrCo_{1-x}Ni_xBi$ has a metallic character.
- (v) C_{11} for all studied alloys are larger than C_{12} and C_{44} , hence all alloys have higher resistance to be compressed in x -direction.
- (vi) $ZrCo_{1-x}Ni_xBi$ ($x = 0, 0.25, 0.75$ and 1) alloys show an anisotropic character.
- (vii) Cauchy pressure calculation discloses that covalent bonding dominates in $ZrCoBi$ and $ZrNiBi$, while ionic bonding dominates in Ni -doped $ZrCo_{1-x}Ni_xBi$ alloys

- (viii) It is noticed that the smallest value of minimum thermal conductivity occurs for $ZrCo_{0.25}Ni_{0.75}Bi$ in all studied directions. Therefore, the half-Heusler alloys $ZrCo_{1-x}Ni_xBi$ ($x = 0, 0.25, 0.75$ and 1) would be useful for high-temperature thermal device applications.

ORCID IDs

 Mahmoud Al-Elaimi, <https://orcid.org/0000-0001-6985-1012>

REFERENCES

- [1] T. Graf, C. Felser, and S.S.P. Parkin, "Simple rules for the understanding of Heusler compounds", *Progress in Solid State Chemistry*, **39**(1), 1 (2011), <https://doi.org/10.1016/j.progsolidstchem.2011.02.001>
- [2] R. Majumder, M.M. Hossain, and D. Shen, "First-principles study of structural, electronic, elastic, thermodynamic and optical properties of LuPdBi half-Heusler compound", *Modern Physics Letters B*, **33**(30), 1950378 (2019), <https://doi.org/10.1142/s0217984919503780>
- [3] M.K. Bamgbose, "Electronic structure and thermoelectric properties of HfRhZ (Z= As, Sb and Bi) half-Heusler compounds", *Applied Physics A*, **126**(7), 1 (2020), <https://doi.org/10.1007/s00339-020-03691-3>
- [4] B. Nanda, and I. Dasgupta, "Electronic structure and magnetism in half-Heusler compounds", *Journal of Physics: Condensed Matter*, **15**(43), 7307 (2003), <https://doi.org/10.1088/0953-8984/15/43/014>
- [5] J.W. Bos, and R.A. Downie, "Half-Heusler thermoelectrics: a complex class of materials", *J. Phys. Condens Matter*, **26**(43), 433201 (2014), <https://doi.org/10.1088/0953-8984/26/43/433201>
- [6] A. Roy, J.W. Bennett, K.M. Rabe, and D. Vanderbilt, "Half-Heusler semiconductors as piezoelectrics", *Physical review letters*, **109**(3), 037602 (2012), <https://doi.org/10.1103/PhysRevLett.109.037602>
- [7] J. Ma, V.I. Hegde, K. Munira, Y. Xie, S. Keshavarz, D.T. Mildebrath, C. Wolverton, A.W. Ghosh, and W.H. Butler, "Computational investigation of half-Heusler compounds for spintronics applications", *Physical Review B*, **95**(2), 024411 (2017), <https://doi.org/10.1103/PhysRevB.95.024411>
- [8] T. Gruhn, "Comparative ab initio study of half-Heusler compounds for optoelectronic applications", *Physical Review B*, **82**(12), 125210 (2010), <https://doi.org/10.1103/PhysRevB.82.125210>
- [9] S. Chen, and Z. Ren, "Recent progress of half-Heusler for moderate temperature thermoelectric applications", *Materials today*, **16**(10), 387 (2013), <https://doi.org/10.1016/j.mattod.2013.09.015>
- [10] G.-H. Yu, Y.-L. Xu, Z.-H. Liu, H.-M. Qiu, Z.-Y. Zhu, X.-P. Huang, and L.-Q. Pan, "Recent progress in Heusler-type magnetic shape memory alloys", *Rare Metals*, **34**(8), 527 (2015), <https://doi.org/10.1007/s12598-015-0534-1>
- [11] F. Casper, T. Graf, S. Chadov, B. Balke, and C. Felser, "Half-Heusler compounds: novel materials for energy and spintronic applications", *Semiconductor Science and Technology*, **27**(6), 063001 (2012), <https://doi.org/10.1088/0268-1242/27/6/063001>
- [12] R. Majumder, and M.M. Hossain, "First-principles study of structural, electronic, elastic, thermodynamic and optical properties of topological superconductor LuPtBi", *Computational Condensed Matter*, **21**, e00402 (2019), <https://doi.org/10.1016/j.cocom.2019.e00402>
- [13] Jung, D., H.-J. Koo, and M.-H. Whangbo, "Study of the 18-electron band gap and ferromagnetism in semi-Heusler compounds by non-spin-polarized electronic band structure calculations", *Journal of Molecular Structure: THEOCHEM*, **527**(1-3), 113 (2000), [https://doi.org/10.1016/S0166-1280\(00\)00483-8](https://doi.org/10.1016/S0166-1280(00)00483-8)
- [14] N. Mehmood, R. Ahmad, and G. Murtaza, "Ab initio investigations of structural, elastic, mechanical, electronic, magnetic, and optical properties of half-Heusler compounds RhCrZ (Z= Si, Ge)", *Journal of Superconductivity Novel Magnetism*, **30**(9), 2481 (2017), <https://doi.org/10.1007/s10948-017-4051-3>
- [15] O. Osafire, and J. Azi, "Structural, electronic, elastic and mechanical properties of novel ZrMnAs half Heusler alloy from first principles", *Physica B: Condensed Matter*, **571**, 41 (2019), <https://doi.org/10.1016/j.physb.2019.06.004>
- [16] M. Yazdani-Kachoei, and S. Jalali-Asadabadi, "Topological analysis of electron density in half-Heusler ZrXBi (X= Co, Rh) compounds: A density functional theory study accompanied by Bader's quantum theory of atoms in molecules", *Journal of Alloys Compounds*, **828**, 154287 (2020), <https://doi.org/10.1016/j.jallcom.2020.154287>
- [17] G. Surucu, M. Isik, A. Candan, X. Wang, and H.H. Gullu, "Investigation of structural, electronic, magnetic and lattice dynamical properties for XCoBi (X: Ti, Zr, Hf) Half-Heusler compounds", *Physica B: Condensed Matter*, **587**, 412146 (2020), <https://doi.org/10.1016/j.physb.2020.412146>
- [18] H. Zhu, J. Mao, Z. Feng, J. Sun, Q. Zhu, Z. Liu, D.J. Singh, Y. Wang, and Z. Ren, "Understanding the asymmetrical thermoelectric performance for discovering promising thermoelectric materials", *Sci. Adv.*, **5**(6), eaav5813 (2019), <https://doi.org/10.1126/sciadv.aav5813>
- [19] P. Hohenberg, and W. Kohn, "Inhomogeneous electron gas", *Physical Review B*, **136**(3B), B864 (1964), <https://doi.org/10.1103/PhysRev.136.B864>
- [20] P. Blaha, K. Schwarz, G.K.H. Medsen, D. Kvasnicka, and J. Luitz, (2001), *WIEN2k, An Augmented Plane Wave Plus Local Orbitals Program for Calculating Crystal Properties*, (Vienna University Technology, Vienna, Austria, 2001).
- [21] J.P. Perdew, K. Burke, and M. Ernzerhof, "Generalized gradient approximation made simple", *Physical review letters*, **77**(18), 3865 (1996), <https://doi.org/10.1103/PhysRevLett.77.3865>
- [22] R. Golezorkhtabar, P. Pavone, J. Spitaler, P. Puschnig, and C. Draxl, ElaStic: A tool for calculating second-order elastic constants from first principles. *Computer Physics Communications*, **184**(8), 1861 (2013), <https://doi.org/10.1016/j.cpc.2013.03.010>
- [23] F.D. Murnaghan, "The Compressibility of Media under Extreme Pressures", *Proc. Natl. Acad. Sci. USA*, **30**(9), 244 (1944), <https://doi.org/10.1073/pnas.30.9.244>
- [24] C.B.H. Evers, C.G. Richter, K. Hartjes, and W. Jeitschko, "Ternary transition metal antimonides and bismuthides with MgAgAs-type and filled NiAs-type structure", *Journal of alloys compounds*, **252**(1-2), 93 (1997), [https://doi.org/10.1016/S0925-8388\(96\)02616-3](https://doi.org/10.1016/S0925-8388(96)02616-3)
- [25] J. Wang, S. Yip, S.R. Phillpot, and D. Wolf, "Crystal instabilities at finite strain", *Physical review letters*, **71**(25), 4182 (1993), <https://doi.org/10.1103/PhysRevLett.71.4182>

- [26] R.M. Hussein, and O.I. Abd, "Influence of Al and Ti additions on microstructure and mechanical properties of leaded brass alloys", *Indian Journal of Materials Science*, **2014**, (2014), <https://doi.org/10.1155/2014/909506>
- [27] S. Pugh, "XCII. Relations between the elastic moduli and the plastic properties of polycrystalline pure metals", *The London, Edinburgh, Dublin Philosophical Magazine Journal of Science*, **45**(367), 823 (1954), <https://doi.org/10.1080/14786440808520496>
- [28] D.G. Pettifor, "Theoretical predictions of structure and related properties of intermetallics", *Materials Science and Technology*, **8**(4), 345 (1992), <https://doi.org/10.1179/mst.1992.8.4.345>
- [29] R.A. Johnson, "Analytic nearest-neighbor model for fcc metals", *Phys. Rev. B, Condens. Matter*, **37**(8), 3924 (1988), <https://doi.org/10.1103/physrevb.37.3924>
- [30] D.G. Cahill, S.K. Watson, and R.O. Pohl, "Lower limit to the thermal conductivity of disordered crystals", *Phys. Rev. B, Condens. Matter*, **46**(10), 6131 (1992), <https://doi.org/10.1103/physrevb.46.6131>
- [31] M. Khan, and Y. Zeng, "Achieving low thermal conductivity in Sr (Zr_{0.9}Yb_{0.05}Gd_{0.05}O₂)₉₅: A suitable material for high temperature applications", *Ceramics International*, **46**(18), 28778 (2020), <https://doi.org/10.1016/j.ceramint.2020.08.040>
- [32] D. Zhao, M. Zuo, L. Bo, and Y. Wang, "Synthesis and Thermoelectric Properties of Pd-Doped ZrCoBi Half-Heusler Compounds", *Materials (Basel)*, **11**(5), 728 (2018), <https://doi.org/10.3390/ma11050728>
- [33] V. Ponnambalam, et al., "Thermoelectric Properties of Half-Heusler Bismuthides ZrCo_{1-x}Ni_xBi (x=0.0 to 0.1)", *Journal of electronic materials*, **36**(7), 732 (2007), <https://doi.org/10.1007/s11664-007-0153-1>
- [34] F. Hamioud, and A. Mubarak, "The mechanical, optoelectronic and thermoelectric properties of NiYSn (Y= Zr and Hf) alloys", *International Journal of Modern Physics B*, **31**(23), 1750170 (2017), <https://doi.org/10.1142/S0217979217501703>

СТРУКТУРНІ, ТЕРМІЧНІ ТА ЕЛЕКТРОННІ ДОСЛІДЖЕННЯ НАПІВ-ГЕЙСЛЕРОВИХ СПЛАВІВ $ZrCo_{1-x}Ni_xBi$ ($x=0, 0,25, 0,75$ і 1)

Махмуд Аль-Елаймі

Факультет фундаментальних наук, деканат підготовчого року, Університет Хаїля, Хаїль, Саудівська Аравія

У статті представлено теоретичну оцінку структурних, механічних, теплових та електричних властивостей напівгейслерових сплавів $ZrCo_{1-x}Ni_xBi$ ($x = 0, 0.25, 0.75$ and 1) в рамках теорії функціоналу щільності (DFT), яка реалізована в коді WIEN2k. Знайдено, що параметри рівноважної решітки узгоджуються з попередньою літературою. Декілька розрахункових механічних властивостей показують, що всі досліджувані сплави є механічно стійкими. Відповідно до критичних значень V/G , леговані Ni сплави $ZrCoBi$ є пластичними, тоді як $ZrCoBi$ та $ZrNiBi$ крихкі. Зонна структура та щільність станів цих сполук показують, що $ZrCoBi$ має напівпровідникову природу, тоді як легований Ni $ZrCoBi$ має напівметалеву природу. Структурні реформи, внесені до $ZrCoBi$ у міру збільшення концентрації Ni-допantu на місці Co-атома, показали збільшення його металічності, провідності та пластичності, а також зниження його жорсткості, стисливості, мінімальної теплопровідності, температур плавлення та Дебая. Згідно з отриманими результатами, сплави $ZrCo_{1-x}Ni_xBi$ ($x = 0, 0.25, 0.75$ and 1) можуть мати потенційне термічне та електронне застосування.

Ключові слова: $ZrCoBi$; першопринципи; сполуки напів-Гейслера; електронна структура; заміщення Ni/Co

CORRELATING DEPOSITION PARAMETERS WITH STRUCTURE AND PROPERTIES OF NANOSCALE MULTILAYER (TiSi)N/CrN COATINGS[†]

 Vyacheslav M. Beresnev^a,  Olga V. Maksakova^a,  Serhiy V. Lytovchenko^{a*},
 Serhiy A. Klymenko^b,  Denis V. Horokh^a,  Andrey S. Manohin^b,  Bohdan O. Mazilin^a,
 Volodymyr O. Chyshkala^a,  Vyacheslav A. Stolbovoy^c

^a*V.N. Karazin Kharkiv National University
4, Svobody Sq., 61000 Kharkiv, Ukraine*

^b*V.M. Bakula Institute of Superhard Materials of the National Academy of Sciences of Ukraine
2, Avtozavodska str., 04074 Kyiv, Ukraine*

^c*National Science Center «Kharkiv Institute of Physics and Technology»
1, Akademichna Str., 61108 Kharkiv, Ukraine*

Corresponding Author: s.lytovchenko@karazin.ua, (+380)-50-694-33-21

Received May 2, 2022; accepted May 30, 2022

Multilayer (TiSi)N/CrN coatings were fabricated through vacuum-arc deposition by applying the arc currents of (100 ÷ 110) A on TiSi cathode and (80 ÷ 90) A on Cr cathode, negative bias potential connected to the substrate holder of $-(100 \div 200)$ V and reactive gas pressure of (0.03 ÷ 0.6) Pa. Applying a negative bias voltage on substrates enhanced the ion bombardment effect, which affected the chemical compositions, phase state, mechanical and tribological properties of (TiSi)N/CrN coatings. Obtained results indicated that (TiSi)N/CrN coatings with Si content ranging from 0.53 to 1.02 at. % exhibited a high hardness level of (22.1 ÷ 31.1) GPa accompanied with a high Young's modulus of (209 ÷ 305) GPa, H/E* level of (0.080 ÷ 0.100), H³/E*² level of (0.15 ÷ 0.33) GPa, and the friction coefficient of 0.35. Values of critical loads at dynamic indentation, changes in friction coefficient and level of acoustic emission signal evidence the high adhesive strength of (TiSi)N/CrN coatings, which allows recommending them to increase cutting tool performance.

Keywords: multilayer coatings, refractory metal nitrides, hardness, adhesive strength

PACS: 61.46.-w, 62.20. Qp, 62-65.-g

INTRODUCTION

CrN-based coatings are well known for their higher ductility and fracture toughness, lower coefficient of friction, and excellent oxidation and corrosion resistance compared to extensively used TiN coatings [1, 2]. Additionally, the lower coefficients of friction of CrN coatings provide better wear resistance than TiN coatings under dry sliding conditions; in addition, their high toughness prevents the initiation and propagation of cracks in erosive environments. For these reasons, CrN coatings have been used to protect cutting tools in the machining of copper, aluminium, and titanium based alloys [3] and have become a successful alternative to TiN coatings for protecting injection moulding tools. However, in other potential industries, CrN coatings demonstrate limited use due to their relatively low hardness compared to TiN [3]. In recent years, almost all single-layer coatings satisfy the needs of industry less and less and do not always meet the requirements for increasing their performance. Nanocomposite coatings based on nitrides of the refractory metals are one of the prospective basements in the development of up-to-date multifunctional coatings as they have high both physical and mechanical properties. The combination of mentioned properties of known coatings based on nitrides and carbides of the refractory metals is achieved by their doping with such elements as Al, Si, B, etc. A good example of such doping is the Ti–Si–N ternary system with a silicon content of about 5~10 at.; it has high hardness (≥ 40 GPa) and better oxidation resistance compared to traditional TiN coatings [4, 5]. These characteristics are mainly explained by the structure of the film, which is defined as a nanocomposite consisting of nanocrystalline TiN embedded in amorphous Si₃N₄ [6–8]. In addition, the amorphous phase becomes an oxygen barrier that slows down the oxidation [8]. However, despite all the advantages of the nanocomposite structure, there is a high residual stress between the TiSiN film and the substrate, which causes low adhesion [9]. At the same time, CrN-based coatings are commonly used as a protective hard coating on tool steels for industrial applications due to its good adhesion strength, chemical stability, and high temperature oxidation resistance.

Therefore, in this study, CrN coatings are used as intermediate (second) layers for the formation of (TiSi)N/CrN periodic structure. Such a multilayer coating with layers of nanometer thickness makes it possible to achieve the better hardness and fracture toughness compared to single-layer coatings due to the interfaces that prevent the movement of dislocations and the difference in the elastic modulus of the layers.

EXPERIMENTAL DETAILS AND METHODS

Multilayer coatings were obtained by the vacuum-arc deposition technique. Two cathodes made of TiSi with the elemental composition of Ti = 94 at.% & Si = 6 at.% and hot-pressed Cr with a purity of about 99.6 % were used as

[†] **Cite as:** V.M. Beresnev, O.V. Maksakova, S.V. Lytovchenko, S.A. Klymenko, D.V. Horokh, A.S. Manohin, B.O. Mazilin, V.O. Chyshkala, and V.A. Stolbovoy, East Eur. J. Phys. 2, 112 (2022), <https://doi.org/10.26565/2312-4334-2022-2-14>

© V.M. Beresnev, O.V. Maksakova, S.V. Lytovchenko, S.A. Klymenko, D.V. Horokh, A.S. Manohin, B.O. Mazilin, V.O. Chyshkala, and V.A. Stolbovoy, 2022

evaporated materials. The regime of the deposition was a continuous rotation of the samples at a speed of 8 rpm. The total deposition time was 1.5 hours. The material of the substrate was an austenitic chromium-nickel stainless steel. The dimensions of the substrate were: length $L = 18$ mm, width $W = 18$ mm and thickness $H = 3$ mm. Four series of samples were formed at different pressures of the reaction gas ($P_N = 0.08 \div 0.6$ Pa) and bias potential ($U_b = -100 \div -200$ V). To manage the nanoscale diapason of the layers, the thickness of the deposited layers was estimated. The calculations were carried out on the basis of a theoretical model, which was described in [10]. When the deposition of a coating on a rotating substrate, during the evaporation, the surface of the substrates alternately passes through zones directly near the operating evaporators, and zones in which deposition on the substrate does not occur as a result of the action of geometrical factors. Therefore, a generalized solution was obtained for calculating the thickness of the deposited layers, including dependences on the size of the holder with samples r at a given radius R , as well as on the angle α , since the angular values in these zones and the rate of condensation at an arbitrary point will also change (see Fig. 1). In the case where condensation of the substance occurs on a single rotating surface located at a distance r from the axis of the chamber (corresponding to half the size of the sample holder), with two simultaneously operating evaporators on a circle with radius R (distance between cathode and samples), there are the following zones: "shadow" zone of space in which there is no condensation of the direct flow of the target cathode material; zones in which condensation of material that evaporates from only one evaporator occurs; as well as zones where the flows of materials from the two evaporators overlap to varying degrees (depending on r - the ratio r / R and α - the angle of rotation of the sample holder; at some values of r these zones are not realized).

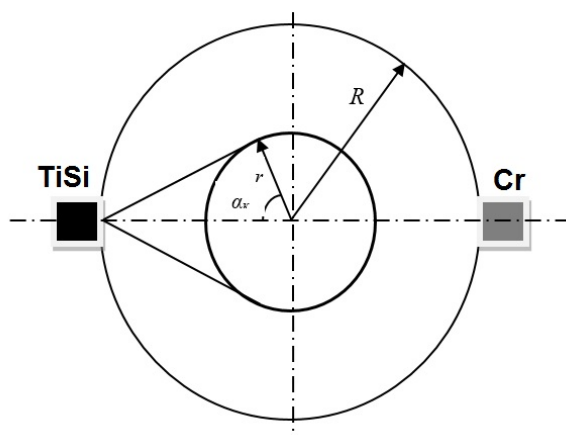


Figure 1. Scheme of deposition of multilayer (TiSi)N/CrN coatings from two evaporators (TiSi and Cr) on a rotating steel substrate.

Table 1 presents the results of calculating the deposition rates and thicknesses of the layers deposited during one rotation of the holder for multilayer (TiSi)N/CrN coatings (V_0 is the condensation rate of the material flow during a normal fall on a stationary substrate).

Table 1. Deposition rates of multilayer (TiSi)N/CrN coatings.

Evaporator	Radius R , mm	Size of the holder r , mm	r'	Angle α , deg	Rotation speed ω , rpm	V_0 , nm/s	Thickness after 1 rotation h_t , nm
TiSi	200	125	0,625	51	8	0,69	3,21
Cr						0,75	3,49

The physical and technological parameters, as well as the elemental composition of the obtained coatings, are shown in Table 2.

Table 2. Technological parameters and elemental composition of multilayer (TiSi)N/CrN coatings.

Seria	Coating	Arc current $I_{TiSi/I_{Cr}}$, A	Reaction gas P_N , Pa	Bias potential U_b , V	Elemental composition, at.%			
					Ti	Si	Cr	N
<i>a</i>	(TiSi)N/CrN	110/90	0.08	-100	52.05	0.89	21.13	25.93
<i>b</i>		100/80	0.08	-200	41.39	0.94	28.80	28.87
<i>c</i>		100/80	0.3	-200	38.54	1.02	17.40	43.04
<i>d</i>		100/80	0.6	-200	30.15	0.53	17.21	52.11

The study of elemental composition of the coatings was carried out by analyzing the spectra of characteristic X-ray radiation generated by an electron beam in a scanning electron microscope FEI Nova NanoSEM 450. The spectra were recorded using an EDAX PEGASUS energy-dispersive X-ray spectrometer fitted to a scanning electron microscope. Phase analysis was carried out by X-ray diffractometry in $Cu\text{-}\alpha$ radiation in a DRON-4 setup. The hardness of the coatings was measured using a high performance micro-hardness testing machine equipped with the

Vickers indenter. The load of 0.4903 N (50 g) was applied for a time of 10–15 s. Adhesion strength of the coatings was determined by sclerometry with simultaneous registration of acoustic emission (AE) signals. The Revetest scratch tester by CSM Instruments with a diamond spherical indenter of Rockwell C type with a radius of 200 microns was used to determine the adhesion characteristics.

RESULTS AND DISCUSSIONS

The results of the analysis of the elemental composition of the coatings (see Table 2) indicate that they consist of the elements of the cathodes, i.e. Ti, Si, Cr and N. With an increase in the bias potential, the amount of titanium and chromium decreases. Fig. 2 shows a cross-sectional image of multilayer (TiSi)N/CrN coating (seria c) obtained by the vacuum arc deposition.

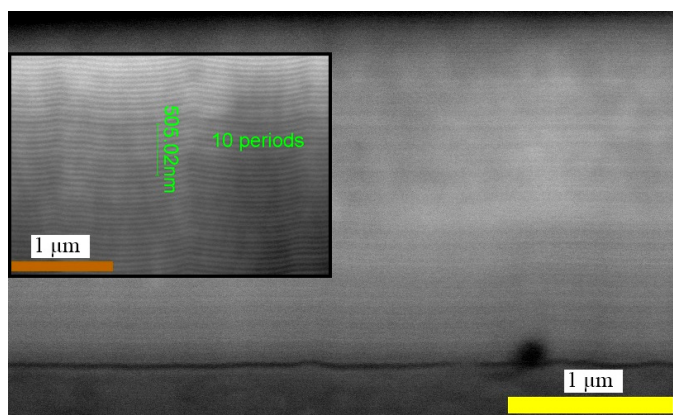


Figure 2. Cross-sectional image of multilayer (TiSi)N/CrN coating (seria c) obtained at $U_b = -200$ V and $P_N = 0.3$ Pa.

The low content of Si in the coating does not lead to the separation with the formation of the SiN_x phase [4], which is confirmed by the absence of peaks corresponding to this phase in diffraction spectra (see Fig. 3).

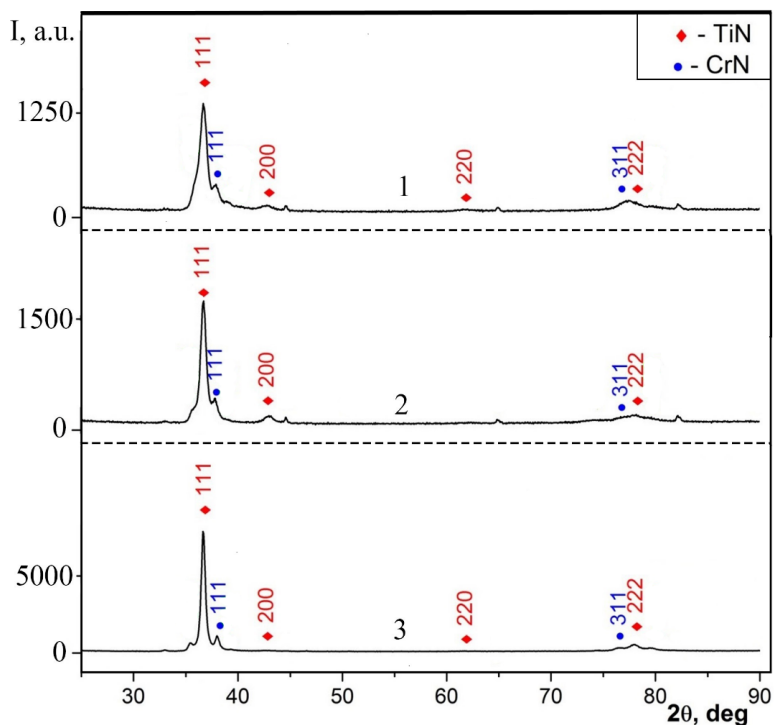


Figure 3. XRD spectra of multilayer (TiSi)N/CrN coatings obtained at $U_b = -200$ V and $P_N = 0.08$ Pa (spectrum 1), $P_N = 0.3$ Pa (spectrum 2) Pa, $P_N = 0.6$ Pa (spectrum 3).

As expected, the nitrogen content is minimal (in the case of the coatings obtained at the lowest gas pressure of 0.08 Pa); therefore, as the analysis of X-ray diffraction spectra (see Fig. 3) has shown, it manifests itself in a bound form, which is characterized by the formation of two phases with strong nitride-forming titanium (with dissolved silicon), forming Ti(Si)N nitride with the preferred orientation of crystallites along the [111] axis and chromium nitride CrN with the [111] axis (see Fig. 3. spectra 1). The calculated lattice periods are 0.4244 nm of (TiSi)N and 0.4101 nm of CrN, and the corresponding sizes of the crystallites are 24.1 nm ((TiSi)N) and 26.8 nm (CrN), respectively.

The spectra also show the presence of α -Ti and Cr phases, where the nitrogen content is so low that the formation of Ti and/or Cr nitride phases becomes impossible. With an increase in the nitrogen pressure to 0.6 Pa, the coating maintains the [111] texture. The lattice period of TiN decreases to 0.4240 nm, while lattice period of CrN increases to 0.4109 nm. The structure of the coating becomes more fine-grained as the crystallite size of TiN and CrN decreases to 12.9 nm and 13.7 nm, respectively (see Fig. 3 spectrum 3). The separation of (111)TiN and (111)CrN diffraction lines indicates the presence of a strong homogeneous [111] texture in both nitride layers. Thus, when forming the coating with sufficiently thin layers (about 7 nm), a significantly higher heat of formation of titanium nitride (see Table 3) leads to a redistribution of nitrogen atoms at low pressure (0.08 ÷ 0.3 Pa), during deposition from Cr to Ti layers (the process is also enhanced by the presence in these Si layers), which is accompanied by the formation of TiSiN and CrN. And only at a high pressure of 0.6 Pa, when TiN is saturated, the separate TiN and CrN phases are formed.

Table 3. Enthalpies of formation (ΔH) of binary metal nitrides and silicides based on studied elements [11, 12].

Enthalpy of formation ΔH , kJ/mol	TiN	TiSi ₂	Si ₃ N ₄	CrN	CrSi ₂
	-337,7	-171,0	-750	-123,2	-77,4

It is known that, in addition to hardness H and reduced Young's modulus E^* , the important characteristics of the coating functionality, that assess the fracture toughness, are the elastic strain to failure and the resistance to plastic deformation, which are presented by the ratios of H/E^* and H^3/E^{*2} , respectively. The H^3/E^{*2} ratio determines the level of toughness of the coating. At the same time, the H/E^* ratio makes it possible to evaluate the deformation of the contacting surfaces [13, 14]. The results of the calculations of H , E^* , H/E^* и H^3/E^{*2} ratios of multilayer (TiSi)N/CrN coatings are presented in Table 4.

Table 4. Mechanical characteristics of multilayer (TiSi)N/CrN coatings

Seria	Reaction gas P_N , Pa	Bias potential U_b , V	Hardness H , GPa	Young's modulus E^* , GPa	H/E^*	H^3/E^{*2}
<i>a</i>	0.08	-100	22.1	209	0.1	0.22
<i>b</i>	0.08	-200	24.5	305	0.08	0.15
<i>c</i>	0.3	-200	28.2	275	0.1	0.28
<i>d</i>	0.6	-200	31.1	298	0.1	0.33

The calculated H/E^* and H^3/E^{*2} ratios for all obtained coatings demonstrate the highest values of the resistance to plastic deformation ($H/E^* > 0.1$ according to the hard nanocomposite films categorization generalized by Musil et al.). The higher level of H^3/E^{*2} , the better resistance of the coating to the formation and propagation of cracks. It should be noted that the maximum hardness value of 31.1 GPa is identified for multilayer (TiSi)N/CrN coating seria *d* obtained at $P_N = 0.6$ Pa and $U_b = -200$ V, which is characterized by rather low crystallite sizes (12.9 nm for (TiSi)N and 13.7 nm for CrN layers), as well as by the best-developed growth texture [111]. From the structural engineering point of view, this state corresponds to the presence of nitride phases (TiSi)N and CrN with an isostructural crystal lattice of the NaCl type in both layers. It should also be noted that layers with lower hardness (CrN) prevent the propagation of cracks in hard layers ((TiSi)N) when operating under dynamic loads, since softer chromium nitride layers have high fracture toughness and resistance to deformation, which makes them promising for use as wear resistant coatings.

To determine the adhesive strength, scratches were applied to the surface of the coatings under progressive loading on the indenter from 0.9 N to 190 N. According to [15], depending on various values of critical loads, several physicochemical processes occur simultaneously during abrasion, however, only L_C is directly related to adhesive failure.

Fig. 4 shows the image of a scratch on the surface of multilayer (TiSi)N/CrN coating seria *d* obtained at $P_N = 0.6$ Pa and $U_b = -200$ V, as well as the change in the average values of the friction coefficient μ (left scale) and the acoustic emission amplitude AE (right scale).

The following main critical loads were recorded by changing the curves of the dependence of the friction coefficient and acoustic emission on the load: L_{C1} is the moment of appearance of the first chevron crack at the bottom and a diagonal crack along the edges of the scratch; L_{C2} is the moment of appearance of chevron cracks at the bottom of the scratch; L_{C3} is the moment of the formation of many chevron cracks at the bottom of the scratch and local peeling of the coating; L_{C4} is the moment of appearance of cohesive-adhesive destructions of the coating; L_{C5} is the moment of plastic abrasion of the coating to the substrate.

To compare the obtained results, the adhesion characteristics of single-layer (TiSi)N and CrN coatings obtained under the same conditions as multilayer (TiSi)N/CrN coatings were used. An analysis of scratches on the surface of (TiSi)N/CrN indicates that the appearance of fluctuations in the acoustic emission signal at low loads is associated not with the destruction of the coating, but with the presence of defects on its surface and structure. When the load increases to 28,9 H (see Table 5, load L_{C3}) the formation of chipping occurs along the edges of the scratch. It is confirmed by a slight increase in the amplitude of acoustic emission and the coefficient of friction; moreover, it increases the penetration depth of the indenter. Obtained results indicate that during scratching multilayer (TiSi)N/CrN coatings wear

out, but do not exfoliate; thus, they are destroyed by the cohesive mechanism associated with plastic deformation and the formation of fatigue cracks in the structure of the coating.

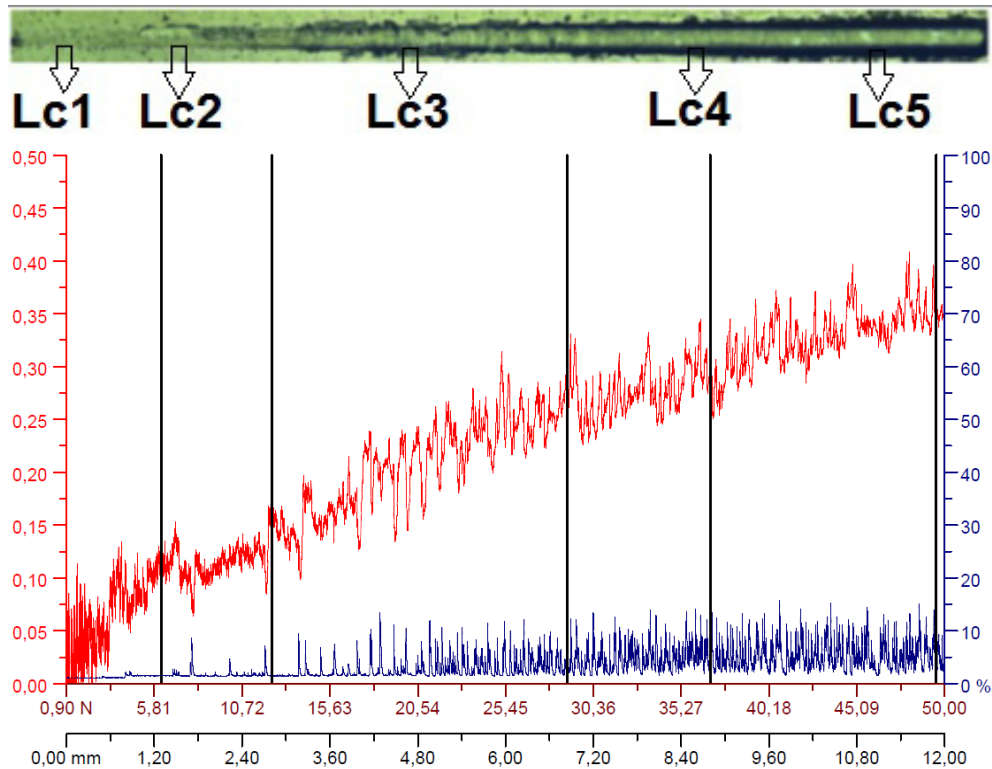


Figure 4. Image of a scratch on the surface of multilayer (TiSi)N/CrN coating obtained at $P_N = 0.6$ Pa and $U_b = -200$ V, as well as the change in the average values of the friction coefficient μ (left scale, red line) and the acoustic emission amplitude AE (right scale, blue line) along the scratch.

Initially, the surface of the coating resists the penetration of the indenter. In this case, the friction coefficient increases non-monotonically, while the amplitude AE signal changes insignificantly (see Fig. 4). Further, with an increase in the load, chips and solely flakes appear along the edges of the scratch (see Fig. 4, image of the scratch); the penetration depth of the indenter continues to increase. The formation of such cracks is accompanied by an increase in the amplitude of acoustic emission and the coefficient of friction. The appearance of the substrate material at the bottom of the scratch is noted when the load L_{C5} reaches 49.54 N (see Fig. 4 and Table 5).

Table 5. Comparative results of the adhesion testing of multilayer (TiSi)N/CrN coating (seria *d*) and single-layer (TiSi)N and CrN coatings

Coating	Reaction gas P_N , Pa	Bias potential U_b , V	Load, N					Friction coefficient, μ
			L_{C1}	L_{C2}	L_{C3}	L_{C4}	L_{C5}	
(TiSi)N/CrN	0.6	-200	6.1	12.4	28.9	36.8	49.5	0.35
(TiSi)N	0.6	-100	9.5	12.4	18.3	48.8	45.3	0.55
CrN	0.6	-100	4.5	7.8	12.3	25.5	37.5	0.24

CONCLUSIONS

1. The effect of vacuum-arc deposition parameters on the composition, structure, and properties of multilayer (TiSi)N/CrN coatings has been studied. It is shown that the two-phase system of NaCl-type structure (fcc crystal lattice) is formed in both nitride layers. The preferred orientation for all obtained coatings is (111).
2. It has been established that in multilayer (TiSi)N/CrN coatings, the nanolayered periodic structure of the layers is even, flat and does not contain visible defects. The smallest crystallites size is 12.9 nm for (TiSi)N and 13.7 nm for CrN layers. Such a nanoscale structure provides the maximum value of hardness of 31.1 GPa and Young's modulus of 298 GPa. The main difference in the structure and properties of multilayer coatings is primarily due to differences in the energy impact of Ti, Si Cr ions on the radiation-stimulated processes of coating formation.
3. The adhesion strength of multilayer (TiSi)N/CrN coating is higher by 10 % compared to single-layer (TiSi)N and/or CrN coatings. The nanoscale multilayer structure decreases the friction mechanisms, i.e. the friction coefficient of (TiSi)N/CrN coating is 0.35, while for (TiSi)N is 0.55.

ORCID IDs

-  Vyacheslav M. Beresnev, <https://orcid.org/0000-0002-4623-3243>;  Olga V. Maksakova, <https://orcid.org/0000-0002-0646-6704>
 Serhiy V. Lytovchenko, <https://orcid.org/0000-0002-3292-5468>;  Serhiy A. Klymenko, <https://orcid.org/0000-0003-1464-3771>
 Denis V. Horokh, <https://orcid.org/0000-0002-6222-4574>;  Andrey S. Manohin, <https://orcid.org/0000-0003-1479-8482>
 Bohdan O. Mazilin, <https://orcid.org/0000-0003-1576-0590>;  Volodymyr O. Chyshkala, <https://orcid.org/0000-0002-8634-4212>
 Vyacheslav A. Stolbovoy, <https://orcid.org/0000-0001-7734-0642>

REFERENCES

- [1] F. Cai, X. Huang, Q. Yang, R. Wie, and D. Nagy. Surf. and Coat. Technol. **205**, 182 (2010), <https://doi.org/10.1016/j.surfcoat.2010.06.033>
- [2] A.O. Andreev, L.P. Sablev, and S.N. Grigor'ev, *Вакуумно-дуговые покрытия* [Vacuum-arc coatings] (Kharkiv, NNC KIPT, 2010), pp. (in Russian).
- [3] B. Navinšek, P. Panjan, and I. Milošev. Surf. and Coat. Technol. **97**(1-3), 182 (1997), [https://doi.org/10.1016/S0257-8972\(97\)00393-9](https://doi.org/10.1016/S0257-8972(97)00393-9)
- [4] S. Veprek, M. Veprek-Heijman, P. Karvankova, and O. Prochazka, Thin Solid Films. **476**(1), 1-29 (2005), <https://doi.org/10.1016/j.tsf.2004.10.053>
- [5] A.D. Pogrebnyak, A.P. Shpak, N.A. Azarenkov, and V.M. Beresnev, Physics-Uspekhi, **52**(1), 29 (2009), <https://doi.org/10.3367/UFNe.0179.200901b.0035>
- [6] H. Zeman, J. Musil, and P. Zeman, J. Vac. Sci. Technol. **A22**(3), 646-664 (2004).
- [7] P.J. Martin, A. Bendavid, J.M. Cairney, and M. Hoffman, Surf. and Coat. Technol. **200**(7), 2228-2235 (2005), <https://doi.org/10.1016/j.surfcoat.2004.06.012>
- [8] A. Cavaleiro, and J. Hosson, *Nanostructured Coatings* (Springer New York, NY, 2006), pp. 648, <https://doi.org/10.1007/978-0-387-48756-4>
- [9] Sh.-Min Yang, Yi.-Yu.Chang, D.-Yi.Lin, Da-Yu.Wang, and W. Wu, Surf. & Coat. Technol. **202**(10), 2176 (2008), <https://doi.org/10.1016/j.surfcoat.2007.09.004>
- [10] Y.V. Kunchenko, V.V. Kunchenko, I.M. Neklyudov, G.N. Kartmazov, and A.A. Andreev, PAST, **2**(90), 203 (2007), https://vant.kipt.kharkov.ua/ARTICLE/VANT_2007_2/article_2007_2_203.pdf
- [11] G.V. Samsonov and I.M. Vinnitskiy, *Тугоплавкие соединения: справочник* [Refractory compounds: handbook] (Metallurgiya, Moscow, 1976), 560 p. (in Russian).
- [12] G.V. Samsonov, L.A. Dvorina, and P.V. Rud', *Силициды* [Silicides] (Metallurgiya, Moscow, 1979), pp. 272. (in Russian).
- [13] S.A. Firstov, V.F. Gorban', E.P. Pechkovskiy, and N.A. Mameka, Materialovedenie, **11**, 26 (2007).
- [14] D.V. Shtansky, S.A. Kulnich, E.A. Levashov, A.N. Sheveiko, F.V. Kirihancev, and J.J. Moore, Thin Solid Films. **420-421**, 330 (2002), [https://doi.org/10.1016/S0040-6090\(02\)00942-2](https://doi.org/10.1016/S0040-6090(02)00942-2)
- [15] J. Valli, J. Vac. Sci. Technol. A, **4**, 3007 (1986) <https://doi.org/10.1116/1.573616>

**КОРЕЛЯЦІЯ МІЖ ПАРАМЕТРАМИ ОСАДЖЕННЯ ТА СТРУКТУРОЮ І ВЛАСТИВОСТЯМИ
НАНОРОЗМІРНИХ БАГАТОШАРОВИХ ПОКРИТТІВ (TiSi)N/CrN**

**В.М. Береснев^а, О.В. Максакова^а, С.В. Литовченко^а, С.А. Клименко^б, Д.В. Горох^а, А.С. Манохін^б,
Б.О. Мазілін^а, В.О. Чишкала^а, В.О. Столбовой^с,**

^аХарківський національний університет імені В.Н. Каразіна, майдан Свободи 4, 61022, м. Харків, Україна

^бІнститут надтвердих матеріалів ім. В.М. Бакуля НАН України, вул. Автозаводська, 2, 04074, м. Київ, Україна

^сНаціональний науковий центр «Харківський фізико-технічний інститут», вул. Академічна, 1, 61108, м. Харків, Україна

Багатошарові покриття (TiSi)N/CrN сформовані методом вакуумно-дугового осадження з двох катодів при струмах дуги (100 ÷ 110) А на TiSi катоді і (80 ÷ 90) А на Cr катоді. Негативний потенціал зміщення на тримачі підкладки становив (100 ÷ 200) В, а тиск реактивного газу в камері (0,03 ÷ 0,6) Па. Негативний потенціал зміщення на підкладках посилював дію іонного бомбардування, що вплинуло на хімічний склад, фазовий стан, механічні та трибологічні властивості покриттів (TiSi)N/CrN. Отримані результати показали, що покриття (TiSi)N/CrN з вмістом Si від 0,53 до 1,02 ат.% мають високу твердість (22,1 ÷ 31,1) ГПа разом з високим модулем Юнга (209 ÷ 305) ГПа, рівнем Н/Е* (0,080 ÷ 0,100), рівнем Н³/Е*² (0,15 ÷ 0,33) ГПа та коефіцієнтом тертя 0,35. Значення критичних навантажень при динамічному вдавлюванні, зміни коефіцієнта тертя і рівня сигналу акустичної емісії при склерометрії свідчать про високу адгезійну міцність покриттів (TiSi)N/CrN, що є підставою рекомендувати їх для підвищення продуктивності різального інструменту.

Ключові слова: багатошарові покриття, нітриди тугоплавких металів, твердість, адгезійна міцність.